UNIVERSITÀ DEGLI STUDI FIRENZE

Da un secolo, oltre.

HR EXCELLENCE IN RESEARCH

PhD in Chemical Sciences

CYCLE XXXVIII

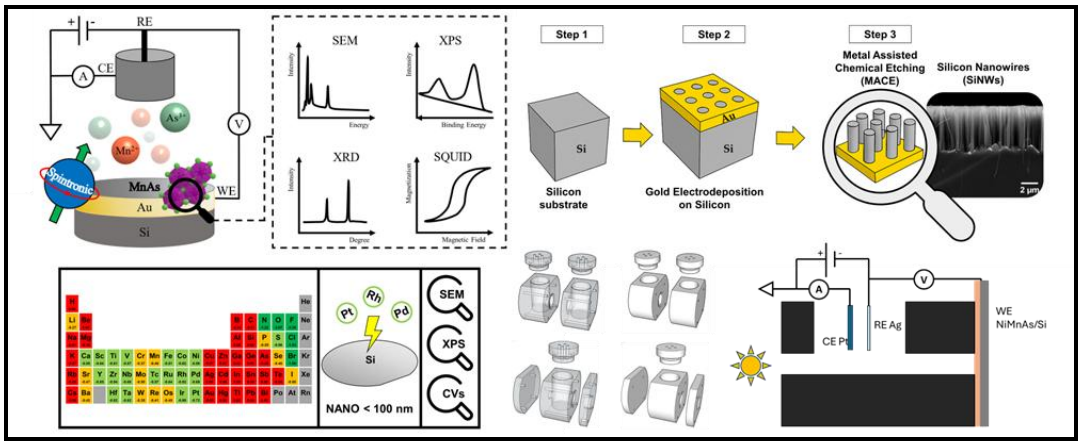

COORDINATOR Prof. ANNA MARIA PAPINI

Electrodeposition and Surface Modification for Technological and Industrial Applications

Academic Discipline (SSD) CHEM-01/A

Doctoral Candidate
Dr. Giulio Pappaianni

Supervisor
Prof. Massimo Innocenti

Co-Supervisor 1
Dr. Aldo Paon

Co-Supervisor 2
Dr. Walter Giurlani

Coordinator
Prof. Anna Maria Papini

UNIVERSITÀ DEGLI STUDI FIRENZE

Da un secolo, oltre.

HR EXCELLENCE IN RESEARCH

PhD in Chemical Sciences

CYCLE XXXVIII

COORDINATOR Prof. ANNA MARIA PAPINI

Electrodeposition and Surface Modification for Technological and Industrial Applications

Academic Discipline (SSD) CHEM-01/A

Doctoral Candidate
Dr. Giulio Pappaianni

Supervisor
Prof. Massimo Innocenti

Co-Supervisor 1
Dr. Aldo Paon

Co-Supervisor 2
Dr. Walter Giurlani

Coordinator
Prof. Anna Maria Papini

Contents

1 Preface

1.1 Abstract

The continuous growth in global energy demand and the urgent need to reduce environmental impact have driven modern research toward the development of materials and technologies that are both efficient and sustainable. Within this framework, electrochemical methods, and in particular electrodeposition, have gained increasing importance as versatile, scalable, and environmentally compatible techniques for the synthesis of functional materials. Unlike high-vacuum or high-temperature physical and chemical vapor deposition processes, electrodeposition allows the fabrication of thin films, alloys, and nanostructures at room temperature and pressure, with fine control over morphology, composition, and thickness. These advantages make it an attractive route for producing materials for advanced applications in energy conversion, catalysis, electronics, and surface engineering.

This doctoral research was conceived and developed within this broader context, aiming to bridge the gap between fundamental electrochemical science and practical industrial applications. The initial hypothesis was that electrodeposition, properly optimized, could be exploited not only for the production of technologically relevant coatings but also as a synthesis route for complex functional materials, such as Heusler-type alloys and nanostructured systems, with potential applications in spintronics, photoelectrochemical (PEC) hydrogen generation, and sustainable electroplating. The work also addressed the pressing need for innovation and environmental responsibility in the decorative and functional plating industries, seeking to replace hazardous processes and materials with safer, more efficient, and digitally monitored alternatives.

The research was carried out in close synergy between academic laboratories and industrial partners, particularly in collaboration with the company Lotti S.r.l. and Italian Fashion Engineering S.r.l., within a framework of technology transfer. The overall objective was to combine advanced material design and characterization with the development of tools and methodologies applicable at the industrial scale, promoting sustainable production models aligned with the principles of the circular economy and the United Nations Sustainable Development Goals (SDGs).

The core scientific objectives of this doctoral project revolved around three main axes:

1. The synthesis and characterization of electrodeposited alloys and compounds on semiconductor substrates for spintronic and PEC applications.
2. The study of metal electrodeposition on silicon for the fabrication of nanostructures and silicon nanowires (NWs) via metal-assisted chemical etching (MACE).
3. The investigation and improvement of electroplating processes from an environmental and technological perspective

A major achievement of this research was the successful electrodeposition and characterization of MnAs-based thin films. The study demonstrated that films with

magnetic properties suitable for spintronic applications can be produced without relying on high-vacuum techniques such as molecular beam epitaxy. Morphological, structural, and magnetic analyses, performed using SEM, XRD, XPS, and SQUID magnetometry, revealed that the films exhibited ferromagnetic behavior close to room temperature. These results confirm that electrodeposition is a viable, low-cost, and energy-efficient method for producing spin-filtering materials, paving the way for their integration into spintronic and magnetoelectronic devices.

Building upon these results, a second phase of the research focused on the Ni–Mn–As ternary system, exploring its electrodeposition and potential use as a bifunctional material for both magnetic and electrocatalytic applications. The Ni–Mn–As alloy films exhibits remarkable potential for spintronic applications, and consequently in the oxygen evolution reaction (OER) optimization, a key step in water electrolysis and hydrogen production. These properties position the material as a promising candidate for OER electrodes. Moreover, the coexistence of magnetic and catalytic functionalities highlights the versatility of electrodeposited alloys as multifunctional materials for energy applications.

Complementary studies addressed the electrodeposition of nanostructured metals on n-type silicon, with particular attention to noble and transition metals such as rhodium and gold. These investigations provided fundamental insights into nucleation mechanisms, interface phenomena, and the role of semiconductor surface chemistry in metal deposition. The results contributed to a deeper understanding of metal-silicon interactions, and electrolyte composition on film morphology and adhesion.

One of the most significant outcomes was the development of an optimized process for silicon nanowire (NW) fabrication via metal-assisted chemical etching (MACE), using electrodeposited metal catalysts. Starting from electrodeposited metal, etching and precise control over silicon nanowire density and length were achieved, eliminating the need for conventional vacuum-based deposition techniques. This approach provides a simpler, cost-effective, and scalable route to produce high-aspect-ratio nanostructures for applications in photovoltaics, sensors, and catalytic systems.

The industrial branch of this research investigated the transition of the decorative electroplating sector toward greener and more sustainable practices. A detailed assessment of the environmental and technological state of the industry highlighted key challenges, including the elimination of cyanide-based baths, the reduction of waste and energy consumption, and the need for real-time process control.

With a focus on sustainability, simulations were performed to predict criticalities and optimize processes, while efforts were made to reduce material consumption and recover metals from processing water. The study presented an overview of sustainable practices within the electroplating industry, addressing ongoing challenges and highlighting the potential of atomistic and multiphysics simulations for the design of greener formulations and components. Industrial strategies aimed

at minimizing metal dispersion were also analyzed, and efficient procedures for metal recovery from wastewater were evaluated

The outcomes of this doctoral research have broad implications for both fundamental science and applied technology. From a scientific standpoint, the successful electrodeposition of MnAs and Ni–Mn–As alloys on silicon represents a significant step forward in expanding the range of materials accessible through electrochemical synthesis. The detailed understanding of nucleation dynamics, interfacial behavior, and structural variations gained through this work provides a foundation for future investigations on other functional materials, including Heusler-type and multicomponent alloys for spintronics, catalysis, and photoconversion.

From an industrial perspective, the research demonstrates the transformative potential of electrodeposition as a sustainable manufacturing platform. The introduction of real-time analytical control, energy-efficient baths, and environmentally safe formulations contributes to reducing the ecological impact of electroplating, while maintaining high production standards and competitive costs.

The work also establishes a concrete example of technology transfer between academia and industry, demonstrating how fundamental research can be effectively translated into practical innovations that support both scientific advancement and socio-economic growth. By connecting frontier topics, such as spin-filtering alloys, photoelectrochemical water splitting, and sustainable surface engineering, this thesis embodies a multidisciplinary approach that spans materials science, electrochemistry, and industrial technology.

In conclusion, this research confirms that electrodeposition, when coupled with advanced analytical characterization, can serve as a unifying tool for addressing some of the most pressing challenges of modern science and technology: the transition to clean energy, and the sustainable use of materials. The results achieved provide new scientific knowledge and a tangible contribution to the ongoing transformation toward a greener, smarter, and more responsible technological future.

1.2 Scientific Production

1.2.1 Published Papers

The following list of publications represents the core research contributions and findings that underpin this work. These studies focus on electrodeposition and surface modification for technological and industrial applications, providing a solid foundation for the discussions and conclusions developed in this thesis.

- G. Pappaianni, F. Visconti, F. Montanari, M. Bonechi, C. Fontanesi, M. Pagliai, W. Giurlani, M. Innocenti. "Electrodeposition of metals on silicon for enhanced silicon nanowires (NWs) Fabrication via Metal Assisted Chemical Etching (MACE)". Electrochimica Acta. Elsevier. 2025, 535, 146705. https://www.sciencedirect.com/science/article/pii/S0013468625010667

- G. Pappaianni, F. Montanari, M. Bonechi, G. Zangari, W. Giurlani, M. Innocenti. "Electrodeposition of Nanostructured Metals on n-Silicon and Insights into Rhodium Deposition". Nanomaterials. MDPI. 2024, 14(24), 2042. https://doi.org/10.3390/nano14242042

- W. Giurlani, G. Pappaianni, F. Biffoli, E. Mariani, M. Bonechi, L. Giliberti, M. Tufarelli, P. Franzo, E. Cianfanelli, M. Innocenti. "What Is the Current State of Sustainability in the Decorative Electroplating Industry? A Close Look at New Practices and Advances". Sustainability. MDPI. 2024, 16. https://doi.org/10.3390/su16135821

- G. Pappaianni, W. Giurlani, M. Bonechi, N. Calisi, B. Cortigiani, C. Bazzicalupi, A. Caneschi, C. Fontanesi, M. Innocenti. "Electrodeposition of MnAs-Based Thin-Film as a Possible Promising Candidate in Spintronics Applications". Journal of The Electrochemical Society. IOP. 2024, 171. https://iopscience.iop.org/article/10.1149/1945-7111/ad5112 1.2.2 Papers in Preparation

An article is currently in preparation that presents the most recent developments of my research. Although not yet published, it directly relates to the themes addressed in this thesis, particularly the development of an electrodeposited alloy on silicon with potential applications in spin filtering.
The provisional title of the article is: "Electrodeposition and Characterization of Ni–Mn–As Alloy on Silicon for Oxygen Evolution Reaction (OER) Optimization" Authors: G. Pappaianni, T. Batistini, W. Giurlani, M. Innocenti.

1.2.3 Communications and Poster to Conferences

The following list includes oral and poster contributions presented at conferences, which showcase the research carried out during my PhD thesis.

Conference Oral Contributions (15)

[OC15] **Giurlani, W.**, Pappaianni, G., Batistini, T., Mistretta, S., Visconti, F., Montanari, F., Innocenti, M. Electrodeposition of Metals and Alloys on Silicon for Technological Applications. 248th ECS Meeting, Chicago (USA), October 12-16, 2025. E02-1291.
The PhD student G. Pappaianni did not personally attend the symposium and did not present the oral communication.

[OC14] **Innocenti, M.**, Biffoli, F., Bonechi, M., Bruni, F., Caneschi, A., Del Pace, I., De Luca, A., Giovani, C., Giusti, P., Mariani, E., Montanari, F., Pappaianni, G., Giurlani, W. New Electrodeposition Processes, Increased Corrosion Resistance. 248th ECS Meeting, Chicago (USA), October 12-16, 2025. C03-1135.
The PhD student G. Pappaianni did not personally attend the symposium and did not present the oral communication.

[OC13] **Bonechi, M.**, Montanari, F., Maggini, I., Pappaianni, G., Bitossi, S., Giovani, C., Savastano, M., Pagliai, M., Bianchi, A., Innocenti, M. Electrocatalytic Activity of Pd(II) Complexes for Oxygen Reduction Reaction on Modified Electrodes.XXXI Congresso della Divisione di Chimica Analitica della Società Chimica Italiana (SCI), Pisa, (Italy), September 07-11, 2025. O-ELE-1 (pag. 175).

The PhD student G. Pappaianni personally attended the symposium and did not present the oral communication.

[OC12] **Giurlani W**.; Pappaianni G.; Montanari F.; De Luca A.; Innocenti M. Nano-Sized Metal Deposition on Doped Silicon: Electrodeposition and Characterization. Pacific Rim International Meeting of the Electrochemical Society (PRiME 2024), Honolulu, HI, USA, organized by "The Electrochemical Society (ECS)". October 6-11, 2024. E01-1873.
The PhD student G. Pappaianni did not present and did not attend the Symposium.

[OC11] **Innocenti M**.; Giurlani W.; Rosini A.; Marcucci M.; Bonechi M.; Verrucchi M.; Biffoli F.; Pappaianni G.; Mariani E.; Giovani C.; Fontanesi C. Sustainability in the Electroplating Industry: A Challenge to Overcome. Pacific Rim International Meeting of the Electrochemical Society (PRiME 2024), Honolulu, HI, USA, organized by "The Electrochemical Society (ECS)". October 6-11, 2024. E01-1930.
The PhD student G. Pappaianni did not present and did not attend the Symposium.

[OC10] **Giurlani W**.; Verrucchi M.; Bonechi M.; Pappaianni G.; Marziali M.; Zangari G.; Innocenti M. Determination of additives in copper plating baths by dynamic Electrochemical Impedance Spectroscopy (EIS). XXVIII Congresso Nazionale della Società Chimica Italiana (SCI 2024), Milan, MI, Italy, organized by Società Chimica Italiana (SCI), August 26-30, 2024. ANA-OR-017.
The PhD student G. Pappaianni won the grant, did not present and personally attended the Symposium.

[OC9] **G. Pappaianni**, F. Montanari, W. Giurlani, A. Meoli, D. Morini, M. Innocenti. "Electrodeposition and characterization of thin films on silicon", 15th International Workshop on Electrodeposited Nanostructures (EDNANO-15), Metz, France, organized by Université de Lorraine, Institut Jean Lamour 15/11/2023-18/11/2023.
The PhD student personally attended the Symposium and presented the oral communication.

[OC8] **G. Pappaianni**, W. Giurlani, D. Morini, M. Bonechi, F. Montanari, C. Bazzicalupi, M. Innocenti. "Electrodeposition and characterization of manganese arsenides (MnxAs) as promising candidates in spintronics", XXX Congresso della Divisione di Chimica Analitica Vasto, CH, Italy, organized by Divisione di Chimica Analitica organizzato dalla Società Chimica Italiana (SCI) 17/09/2023 – 21/09/2023 [O2-EL].
The student was the winner of the scholarship for participation.
The PhD student personally attended the Symposium and presented the oral communication.

[OC7] **M. Innocenti**, F. Biffoli, M. Bonechi, A. Comparini, E. Mariani, G. Pappaianni, M. Verrucchi, A. De Luca, W. Giurlani. "The importance of analytical spectroscopy in the fashion industry", XXX Congresso della Divisione di Chimica Analitica Vasto, CH, Italy, organized by Divisione di Chimica Analitica organizzato dalla Società Chimica Italiana (SCI) 17/09/2023 – 21/09/2023 [O1-S].
The PhD student personally attended the Symposium and did not presented the oral communication.

[OC6] **I. Maccioni**, F. Pizzetti, G. Pappaianni, A. Meoli, E. Mariani, C. Giovani, R. Emanuele, M. Innocenti. "Spectroscopic characterization of corrosion processes on galvanic coatings". ISA 2023 Incontro di Spettroscopia Analitica Milan, Italy organized by Gruppo Divisionale di Spettroscopia Analitica (GSA) della Società Chimica Italiana. 14/06/2023 – 16/06/2023 [O15].
The PhD student did not present and did not attend the Symposium.

[OC5] **W. Giurlani**, G. Pappaianni, M. Bonechi, N. Calisi, M. Mannini, C. Bazzicalupi, C. Fontanesi, M. Innocenti. "Electrodeposition of Manganese Arsenides (MnxAs) As Promising Candidates in Spintronics" 243rd ECS Meeting Boston, MA, US organized by "The Electrochemical Society (ECS)". 28/05/2023 – 02/06/2023 [E02-1554 (Invited)].
The PhD student did not present and did not attend the Symposium.

Conference Poster Contributions (19)

[PC20] **Innocenti, M.**, Giurlani, W., Bonechi, M., De Luca, A., Mariani, E., Pappaianni, G., Biffoli, F., Giovani, C., Montanari, F., Gellini, C., Del Pace, I., Pagliai, M. New Perspectives in the Electrodeposition of Metal Alloys in the Field of "Made in Italy". Giornate dell'Elettrochimica Italiana (GEI 2025), San Benedetto del Tronto (Italy). September 15-19, 2025. P37 (pag. 148).
The PhD student G. Pappaianni did not attend the symposium and did not present the communication.

[PC19] Pappaianni, G., **Bonechi, M**., Visconti, F., Mistretta, S., Paon, A., Giurlani, W., Innocenti, M. Electrodeposition-Enabled Fabrication of Enhanced Silicon Nanowires via Metal-Assisted Chemical Etching (MACE). Giornate dell'Elettrochimica Italiana (GEI 2025), San Benedetto del Tronto (Italy). September 15-19, 2025. P56 (pag. 167).
The PhD student G. Pappaianni did not attend the symposium and did not present the communication.

[PC18] **Pappaianni, G.**, Giovani, C., Mariani, E., Bitossi, S., Innocenti, M. Electroplating in the Presence of Microplastics: An Analytical Spectroscopic Approach to Investigate Their Influence on Copper Deposition. XXXI Congresso

della Divisione di Chimica Analitica della Società Chimica Italiana (SCI). Pisa (Italy). September 7-11, 2025. P-SPA-10 (pag. 525).
The PhD student G. Pappaianni personally attended the symposium and presented the communication.
The student was awarded a scholarship.

[PC17] **Pappaianni, G.**, Batistini, T., Paon, A., Giurlani, W., Innocenti, M. Electrodeposition and Characterization of Ni–Mn–As Alloy on Silicon for High-Performance Oxygen Evolution Reaction (OER) Electrodes. XXXI Congresso della Divisione di Chimica Analitica della Società Chimica Italiana (SCI). Pisa (Italy). September 7-11, 2025. P-SPA-11 (pag. 526).
The PhD student G. Pappaianni personally attended the symposium and presented the communication.
The student was awarded a scholarship.

[PC16] **Montanari, F**., Pappaianni, G., Visconti, F., Nunziati, P., Giurlani, W., Innocenti, M. Electrodeposition of nanostructured metals on silicon. A focus on the rhodium/n-doped silicon composite as a promising platform for energy applications. 13th International Conference on Environmental Catalysis (ICEC 2025). Palermo (Italy). June 2-5, 2025. P1_28 (pag. 630).
The PhD student G. Pappaianni did not personally attend the symposium and did not present the communication.

[PC15] **Pappaianni, G.,** Visconti, F., Montanari, F., Mistretta, S., Batistini, T., Giurlani, W., Paon, A., Innocenti, M. Electrodeposition of Metals on Silicon for Enhanced Silicon Nanowires (NWs) Fabrication via Metal Assisted Chemical Etching (MACE). 16th International Workshop on Electrodeposited Nanostructures (EDNANO-16). Florence (Italy). April 10-12, 2025. (pag. 77).
The PhD student G. Pappaianni personally attended the symposium and presented the communication.
The student was part of the organizing committee.

[PC14] **Montanari, F.,** Biffoli, F., Becattini, G., Pappaianni, G., Gentilesca, P., Savastano, M., Bianchi, A., Pagliaia, M., Innocenti, M. Oxygen reduction reaction (ORR) in alkaline medium catalyzed using an atomically precise Pd (II) catalyst, prepared by extraction of Pd(II) from a mixture of metal ions using modified multi walled carbon nanotubes (MWCNT). 16th International Workshop on Electrodeposited Nanostructures (EDNANO-16). Florence (Italy). April 10-12, 2025. (pag.76).
The PhD student G. Pappaianni personally attended the symposium and presented the communication.
The student was part of the organizing committee.

List of poster communications at conferences 2024 - PhD student Giulio Pappaianni

[PC13] **Innocenti M**.; Caneschi A.; Cianfanelli E.; Bonechi M.; Verrucchi M.; Mariani E.; Biffoli F.; Pappaianni G.; De Luca A.; Giurlani W.; Bonini M. Addressing sustainability in the electroplating industry: an all-round challenge. XXVIII Congresso Nazionale della Società Chimica Italiana (SCI 2024), Milan, MI, Italy, organized by Società Chimica Italiana (SCI), August 26-30, 2024. ANA-PO-095.

The PhD student G. Pappaianni won the grant, did not present and personally attended the Symposium.

[PC12] **Pappaianni G.**; Montanari F.; Batistoni C.; Lotti A.; Giurlani W.; Innocenti M. Electrodeposition and Characterization of Nanostructured Metal on Silicon. XXVIII Congresso Nazionale della Società Chimica Italiana (SCI 2024), Milan, MI, Italy, organized by Società Chimica Italiana (SCI), August 26-30, 2024. ANA-PO-026.

The PhD student G. Pappaianni won the grant, presented the poster communication and personally attended the Symposium.

[PC11] **Pappaianni G.**; Montanari F., Giurlani W.; Morini D.; Innocenti M. Electrodeposition of Thin Films and Nanostructures of Metals on n-doped monocrystalline Silicon for Energy Applications. 37th Topical Meeting of the International Society of Electrochemistry (ISE), Electrochemical energy for a greener and more sustainable future society, Stresa, VCO, Italy, organized by the International Society of Electrochemistry (ISE), June 9-12, 2024. S3-031.

The PhD student G. Pappaianni served on the organizing team as a "Student Helper", presented the poster communication and personally attended the Symposium.

[PC10] **Verrucchi M.;** Giurlani W.; Pelagatti A.; Pappaianni G.; Mariani E.; Bazzicalupi C.; Innocenti M. Variables evaluation on electrodeposition of palladium hydrides for hydrogen storage. 37th Topical Meeting of the International Society of Electrochemistry (ISE), Electrochemical energy for a greener and more sustainable future society, Stresa, VCO, Italy, organized by the International Society of Electrochemistry (ISE), June 9-12, 2024. S3-042.

The PhD student G. Pappaianni served on the organizing team as a "Student Helper", did not present the poster communication and personally attended the Symposium.

[PC9] **Pappaianni G.**; Giurlani W.; Calisi N.; Bazzicalupi C.; Caneschi A.; Morini D.; Innocenti M. MnAs-based thin-film electrodeposition: a promising prospect in spintronics. Conventional and High-Energy Spectroscopies for inorganic, organic, and biomolecular Surfaces and interfaces (CHESS2024), Brescia, BS, Italy, organized by Università degli Studi di Milano, February12-16, 2024.

The PhD student G. Pappaianni won the grant, presented the poster communication and personally attended the Symposium.

[PC7] **M. Bonechi**, W. Giurlani, E. Mariani, F. Biffoli, G. Pappaianni, A. Stefani, A. Marchetti, C. Fontanesi, M. Innocenti. "Electrochemical Oxidation of Resorcinol: An Integrated Experimental and Theoretical Study" 244th Meeting ECS, Gothenburg, Sweden. 8/10/2023-12/10/2023 [Z01-3132].
The PhD student did not present and did not attend the Symposium.

[PC6] **M. Verrucchi**, **G. Pappaianni**, A. Comparini, I. Del Pace, M. Innocenti. "Electrochemical impedance spectroscopy (EIS) measurements to investigate the organic additives content in commercial plating baths", XXX Congresso della Divisione di Chimica Analitica Vasto, CH, Italy, organized by Divisione di Chimica Analitica organizzato dalla Società Chimica Italiana (SCI). 17/09/2023 – 21/09/2023.
The student was the winner of the scholarship for participation [S-P1].
The PhD student personally attended the Symposium and presented the poster communication.

[PC5] **W. Giurlani**, G. Pappaianni, M. Bonechi, C. Bazzicalupi, C. Fontanesi, M. Innocenti. "Electrodeposition of manganese arsenides (MnxAs) and its compositional optimization assisted by microanalysis spectroscopy". ISA 2023 Incontro di Spettroscopia Analitica Milan, Italy organized by Gruppo Divisionale di Spettroscopia Analitica (GSA) della Società Chimica Italiana. 14/06/2023 – 16/06/2023 [P7].
The PhD student did not present and did not attend the Symposium.

1.2 List of Abbreviations

ASGM	artisanal and small-scale gold mining
BSE	backscattered electrons
CE	counter electrode
CIF	Crystallographic Information File
CV	cyclic voltammetry
CVD	chemical vapor deposition
DAF	dissolved-air flotation
DC	direct current
DFT	density-functional theory
DMADV	define, measure, analyze, design, verify
DMAIC	define, measure, analyze, improve, control
DMSs	dilute magnetic semiconductors
E-ALD	electrochemical atomic layer deposition
EDS	energy dispersive X-ray spectroscopy
EP	electrochemical precipitation
FCC	face-centered cubic
FWHM	full width at half maximum
GC	glassy carbon
GGA	generalized gradient approximation
GIXD	grazing incidence X-ray diffraction
GMR	giant magnetoresistance
HC-Si	high-conductivity silicon
IBS	ion beam sputtering
LC-Si	low-conductivity silicon
MACE	metal-assisted chemical etching
MBE	molecular beam epitaxy
MCL	maximum contaminant level
ME	membrane electrolysis
MM	molecular mechanics
NF	nanofiltration
NWs	silicon nanowires
OER	oxygen evolution reaction
OQMD	Open Quantum Materials Database

PAW	projector-augmented wave
PBE	Perdew–Burke–Ernzerhof
PEC	photoelectrochemical cell
PLD	pulsed laser deposition
PP	polypropylene
PVD	physical vapor deposition
PXRD	powder X-ray diffraction
QM	quantum mechanics
RCA	Radio Corporation of America
RE	reference electrode
RJC-CoC	Responsible Jewellery Council–Chain of Custody
RKKY	Ruderman–Kittel–Kasuya–Yosida
RTC	relative texture coefficient
Rwp	weighted profile R-factor
SDGs	sustainable development goals
SE	secondary electrons
SEM	scanning electron microscope
SLRs	surface-limited reactions
SQUID	superconducting quantum interference device
UPD	underpotential deposition
USEPA	United States Environmental Protection Agency
VASP	Vienna Ab-initio Simulation Package
WE	working electrode
XPS	X-ray photoemission spectroscopy
XRD	X-ray diffraction
XRF	X-ray fluorescence spectroscopy

2 Introduction

In recent years, the urgent need for sustainable and efficient energy systems has driven the scientific community toward the development of new materials and technologies capable of addressing global environmental and industrial challenges. Among the various strategies explored, electrodeposition has emerged as a powerful and versatile technique for the synthesis and surface modification of functional materials, offering significant advantages in terms of cost-effectiveness, scalability, and environmental compatibility. Unlike high-vacuum or high-temperature methods, electrodeposition allows fine control over film morphology, composition, and thickness under ambient conditions, enabling the fabrication of nanostructured coatings and devices for a broad range of technological applications. This doctoral research focuses on the development and characterization of electrodeposited materials: metals, alloys, and semiconductors, for their potential use in both technological and industrial contexts. In particular, the study investigates the electrodeposition of Heusler-type alloys and their integration with semiconductors such as silicon to produce innovative systems for photoelectrochemical (PEC) water splitting, hydrogen generation, and spintronic applications. These studies are complemented by investigations into metal electrodeposition on silicon for the fabrication of nanostructures, such as silicon nanowires via metal-assisted chemical etching (MACE), and by applied research devoted to sustainable practices in the decorative electroplating industry. The research integrates fundamental electrochemical studies with advanced materials characterization: SEM, XRD, XPS, AFM, and SQUID magnetometry, to explore the structural, compositional, and magnetic properties of the electrodeposited films. Density Functional Theory (DFT) calculations support the experimental findings, providing insight into the stability and electronic structure of the investigated systems. Beyond its academic significance, this work aims to contribute to the ongoing technological transition toward green manufacturing. The proposed methodologies address both high-tech sectors, such as spintronics and energy conversion, and traditional industries, including electroplating and jewelry manufacturing, promoting environmentally friendly and resource-efficient processes. By combining innovative materials research with industrial applicability, this thesis bridges the gap between laboratory-scale experimentation and sustainable technological implementation.

This thesis is organized into six main chapters, preceded by a Preface and followed by Final Remarks.

The Preface provides an overview of the research carried out during the PhD course, including a summary of the scientific publications, conference contributions, and other research activities developed throughout the program.

The first chapter introduces the theoretical and methodological framework of the work, describing the main electrochemical techniques employed, such as electrodeposition and cyclic voltammetry, as well as the electrochemistry of silicon, which together form the experimental foundation of this research. The third chapter, “Electrodeposition of MnAs-Based Thin-Film for Spintronics”, focuses on the

synthesis and characterization of MnAs thin films obtained through electrodeposition. This study explores the potential of these materials for spintronic applications, combining experimental results with DFT data to understand their magnetic and structural properties.

The fourth chapter, “Electrodeposition of Nanostructured Metals on n-Type Silicon with Focus on Rhodium”, investigates the electrodeposition of metallic nanostructures on silicon substrates. Special attention is given to rhodium, evaluating its electrochemical behavior and the formation of nanostructured coatings with potential energy and catalytic applications.

The fifth chapter, “Electrodeposited Metal Catalysts for Controlled Fabrication of Silicon Nanowires via metal assisted chemical etching (MACE)”, presents an innovative approach to fabricate silicon nanowires with improved morphology and performance. The study highlights the role of gold deposited via electrodeposition in optimizing the MACE process for energy-related applications.

The sixth chapter, “Electrodeposition and Characterization of Ni–Mn–As Alloy for Oxygen Evolution Reaction (OER) optimization applications”, explores the development of an electrodeposited ternary alloy as an efficient and stable electrocatalyst for water oxidation. The structural, morphological, and electrochemical properties of the alloy are discussed in the context of sustainable hydrogen production and photoelectrochemical water splitting.

The seventh chapter, “Advances and Challenges in Sustainability of the Decorative Electroplating Industry”, broadens the scope of the thesis to industrial and environmental aspects. It examines the transition toward sustainable practices in the decorative electroplating sector, including the adoption of non-toxic baths, energy-efficient processes, and Industry 4.0 monitoring systems.

Finally, the “Final Remarks” chapter summarizes the key findings of the thesis, highlighting how the integration of fundamental electrochemical research and applied industrial studies contributes to advancing the field of electrodeposition and surface modification. Perspectives for future work are outlined, focusing on the development of sustainable materials and scalable technologies for energy and manufacturing applications.

Each chapter represents a progressive step toward achieving the overall objectives of this doctoral research, providing a comprehensive understanding of Electrodeposition and Surface Modification for Technological and Industrial Applications.

2.1 Electrodeposition and Electroanalytical methods

In this chapter, the theoretical background of the techniques primarily employed in this thesis is presented. The discussion focuses on providing concise explanations of these methods while omitting well-established concepts that are considered common knowledge in the field. For any fundamental aspects or background information not included here, appropriate references are provided throughout the text.

Electrochemical investigation techniques can be broadly classified into static and dynamic methods.

Static methods involve measuring the potential difference (ΔE) at $i = 0$, and are therefore conducted under equilibrium conditions, where the Nernst equation applies.

Although potentiometric measurements are of great practical importance, for example, in determining pH or pM values, they do not provide information about the kinetics of the process.

In contrast, dynamic techniques involve perturbing the system by forcing the potential of the working electrode (considered as the independent variable) to a desired value, and measuring the resulting current (the dependent variable) as a function of time. Alternatively, the current can be controlled as the independent variable while measuring the working electrode potential as the dependent variable, again as a function of time[1].

The electrochemical cell used for electrochemical studies generally consists of three electrodes:

- Working electrode, on which the electrochemical reaction of interest takes place.
- Reference electrode, whose potential ideally remains constant even in the presence of faradaic processes. It provides the reference electrical potential against which all other potentials are measured. Ideally, no current should flow through this electrode.
- Counter electrode, which ensures the flow of charge within the electrochemical cell and prevents the current from passing through the reference electrode, thereby avoiding potential drift. To minimize its influence on the system, the counter electrode typically has a surface area much larger than that of the working electrode.

A schematic representation of a typical electrochemical cell is shown in **Figure 1.**

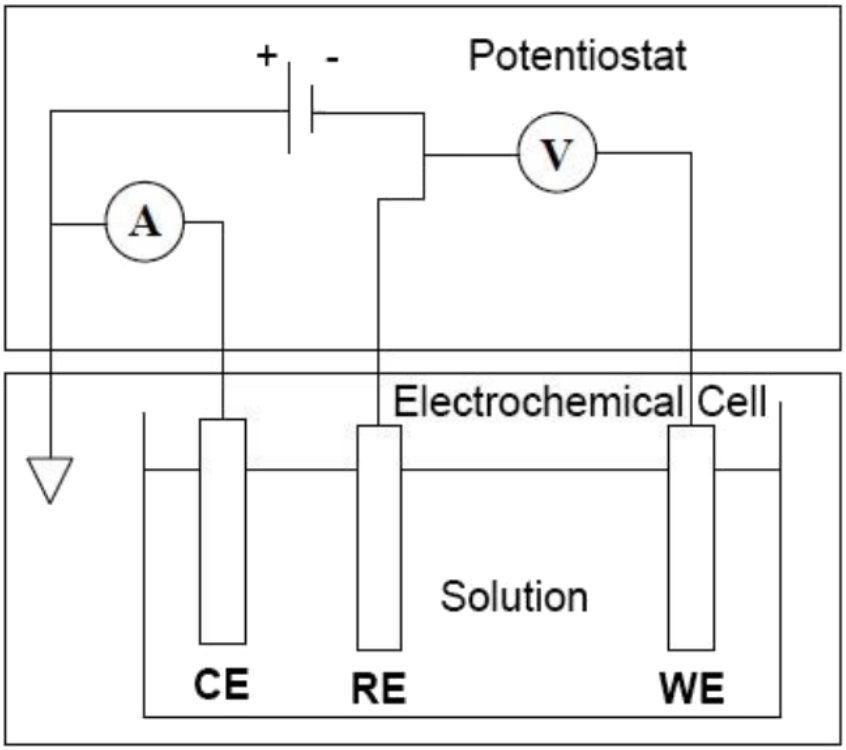

Figure 1 Schematic representation of a three-electrode system showing the electrochemical cell and the potentiostat, illustrated as a voltage source.

2.1.1 Voltammetric Techniques: Cyclic Voltammetry (CV)

Voltammetric techniques are based on measuring the current that flows through an electrochemical cell as a function of the applied potential. Cyclic Voltammetry (CV) is a dynamic electrochemical technique in which a variable potential is applied between the working and reference electrodes (independent variable) using a function generator. This induces a measurable current response, which represents the dependent variable of the system.
The potential scan can take various forms; however, the most common, and the one employed in this doctoral work, is the triangular waveform scan (**Figure 2**). In this configuration, the potential is swept from an initial value E_1 to a final value E_2, with the possibility of repeating the process for a defined number of cycles.

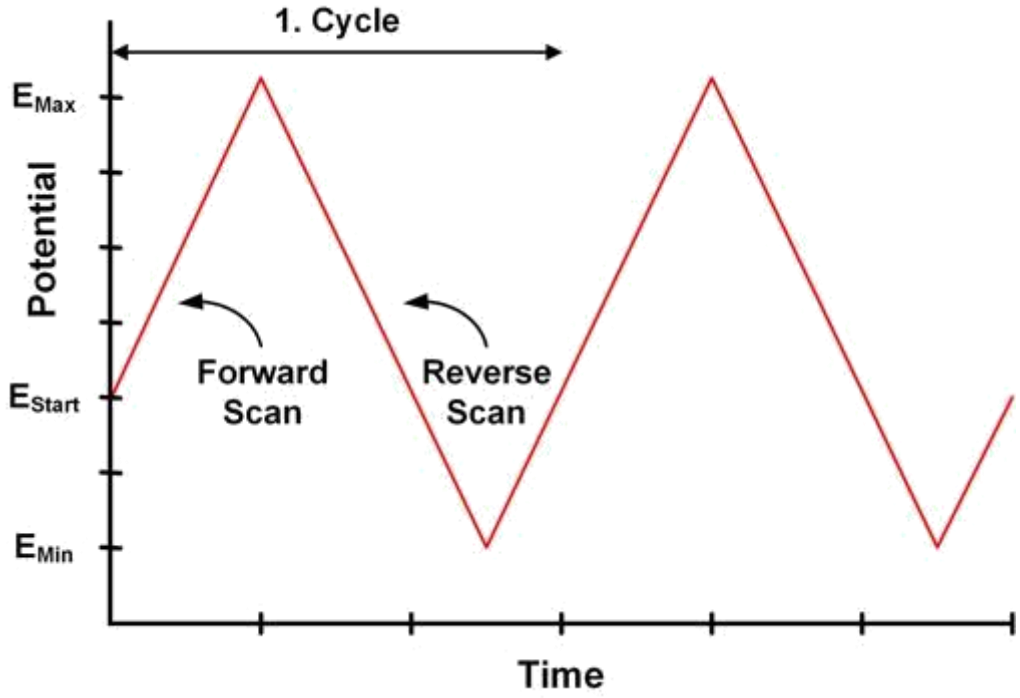

Figure 2 Triangular potential scan of two consecutive cyclic voltammograms (CVs).

In a typical cyclic voltammogram (**Figure 3**), the applied potential is plotted on the x-axis, while the measured current intensity is reported on the y-axis. The most relevant parameters are:

- **Anodic peak potential (E_{pa})**
- **Anodic peak current (i_{pa})** — positive according to the IUPAC convention
- **Cathodic peak potential (E_pc)**
- **Cathodic peak current (i_pc)** — negative according to the IUPAC convention

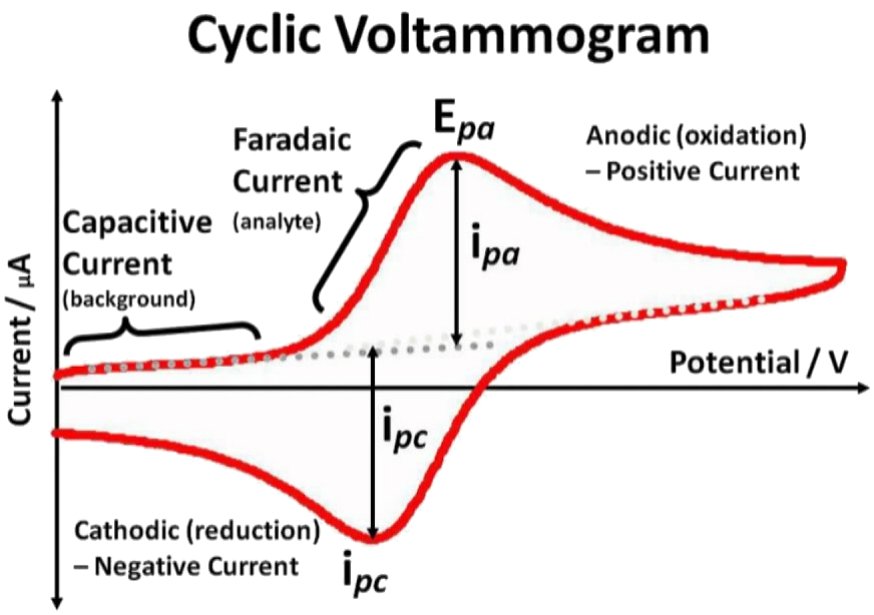

Figure 3 Schematic representation of a typical voltammogram.

The behavior of the current measured during a cyclic potential scan can be summarized as follows. If the species in solution are unreactive at the initial applied potential, the current remains very low over a certain potential range and is primarily due to capacitive effects. At a characteristic potential, when scanning towards more positive potentials, a generic species "R" becomes capable of oxidation, leading to a sudden increase in current attributable to the faradaic oxidation reaction. In this ascending region, the process is charge-transfer controlled**.**

As oxidation progresses, the electrode surface becomes depleted of "R" and enriched with the oxidized species "O," which forms as the reaction product. Consequently, the diffusion layer grows (**Figure 4**). The anodic current continues to increase until the process enters a diffusion-controlled regime. At this point, two scenarios are possible: the current remains constant if the diffusion layer is maintained at a steady thickness through electrode surface renewal or solution stirring; alternatively, as in stationary cyclic voltammetry, the continuous growth of the diffusion layer leads to a decrease in current, giving rise to the typical peak-shaped voltammogram.

Upon reversal of the potential scan, the same behavior occurs for the reverse reaction (O → R) in the case of a reversible redox couple, resulting in negative currents.

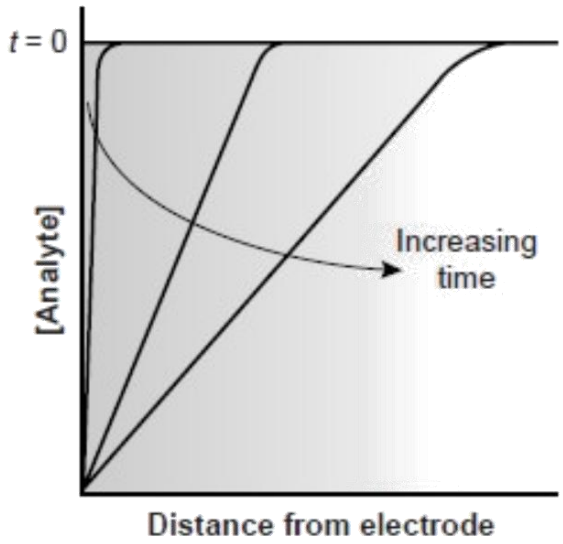

Figure 4 Variation of the concentration at the electrode surface over time.

A reversible redox reaction is characterized by the same amount of charge exchanged (area under the peak) in both the anodic and cathodic directions. Furthermore, the difference between the anodic and cathodic peak potentials, ΔE_p (at 25°C), is given by:

$$\Delta E_p = \left|E_{pa} - E_{pc}\right| = \frac{0.059}{n}\text{V} \quad (1)$$

where n is the number of electrons exchanged. For symmetric peaks, the anodic peak current i_{pa} is equal in absolute value to the cathodic peak current i_pc. If the reaction is irreversible, ΔE_p assumes a value larger than the expected one.
Using the Randles-Sevcik equation, which relates the peak current i_p to the concentration of the electroactive species, quantitative information on the electron transfer kinetics can be obtained:

$$i_p = 0.4463AC\left(\frac{n^3F^3vD}{RT}\right)^{\frac{1}{2}} \quad (2)$$

where A is the electrode area, C the concentration of the electroactive species, D the diffusion coefficient, and v the scan rate.
By integrating the voltammogram, one can obtain information on the total charge and, consequently, the amount of reacted substance (see Equations 3 and 4):

$$Q = \int_0^{\tau} id\tau = \frac{1}{v}\int_{E_1}^{E_2} idE \tag{3}$$

$$Q = \frac{m}{M}Fn \tag{4}$$

where Q is the charge, m the mass of reagent, M its molar mass, n the number of electrons, and F the Faraday constant.

2.1.2 Chronoamperometry

Chronoamperometry is an electrochemical technique in which the potential applied to the working electrode is held at a fixed value, and the resulting faradaic current is measured as a function of time. What is monitored is the current-time behavior, i(t). The experimental setup is the same as that used for voltammetry, with the cell comprising a working electrode, counter electrode, and reference electrode immersed in a quiescent solution. Under these conditions, mass transport to the electrode occurs solely by diffusion (planar stationary electrode and unstirred solution containing supporting electrolyte).
The current-time curve reflects the evolution of the concentration gradient near the electrode surface. As the electrochemical reaction proceeds, the diffusion layer expands, leading to a decrease in the concentration gradient over time. Accordingly, the current decays with time, following the relationship described by the Cottrell equation (Equation 5):

$$i = \frac{nFAC_o D^{\frac{1}{2}}}{t^{\frac{1}{2}}\pi^{\frac{1}{2}}} \tag{5}$$

where n is the number of electrons transferred, F the Faraday constant, A the electrode area, D the diffusion coefficient, and C the bulk concentration of the electroactive species.
Chronoamperometry is generally employed to determine the diffusion coefficient of electroactive species, provided the electrode area is known, or alternatively, to calculate the electrode surface area when the diffusion coefficient is known. In both cases, the analyte concentration is controlled and known.
In the context of electrodeposition, chronoamperometry is widely used to gain insights into the nucleation and growth mechanisms of the species being deposited.

2.1.3 Chronopotentiometry

In galvanostatic techniques, the current between the working and counter electrodes (cell current) is kept constant, while the potential, measured between the reference and working electrodes, is recorded as a function of time.

When current is applied to the system, electrons first charge the double layer, followed by electron transfer; thus, both capacitive and faradaic currents are produced:

$$i = i_c + i_f \tag{6}$$

Due to the instantaneous accumulation of charge in the double layer, the initial potential is significantly far from the equilibrium value but gradually approaches it as electrons are transferred through the faradaic process. After this initial jump, the potential-time profile, *E(t)*, evolves depending on the nature of the electrolytes present in the cell.

The two fundamental parameters in a chronopotentiometric experiment are the magnitude of the applied current and the total experiment time (deposition time).

2.1.4 Electrodeposition of Alloys

The electrodeposition of a compound differs substantially from that of a single element, as the stoichiometry must be maintained.

The general condition for depositing the components of a compound is that the constituents have similar deposition potentials; however, this is not always the case. An effective approach to align the deposition potentials of two components is to complex one of the elements, thereby shifting its deposition potential. If the compound to be deposited has a sufficiently negative heat of formation, this can shift the deposition potential of the less noble component to more positive values, facilitating its co-deposition.

2.1.5 Thermodynamic Factors

The equilibrium conditions for the deposition of individual elements are expressed by the Nernst equation (Equation 7):

$$E = E^0 + \frac{RT}{nF} ln \frac{\Pi(a_{i(ox)}^{v(ox)})}{\Pi(a_{i(red)}^{v(red)})} \tag{7}$$

where *R* is the universal gas constant, *T* the absolute temperature, *a* the chemical activity of the reduced (red) and oxidized (ox) forms of the species, *v* the

stoichiometric coefficients, n the number of electrons transferred in the half-reaction, F the Faraday constant, and E^0 the standard reduction potential of the species.
The potential applied must differ from the equilibrium potential by an amount corresponding to the overpotential. The overall overpotential is the sum of different contributions, the most important of which are: the activation overpotential (present in the Butler-Volmer equation), the concentration overpotential (due to the finite rate at which reactants reach the electrode), and the resistance overpotential (caused by the ohmic drop, IR, associated with current flow in the solution).
For the codeposition of multiple elements, two common scenarios must be considered:

- The reduction potentials of the species are relatively close. In this case, deposition can be achieved by adjusting the ionic activities (or concentrations). However, there is a limit beyond which the potential cannot be shifted merely by changing the concentrations. In some cases, decreasing the activity too much could result in an extremely dilute solution, causing the species to be consumed very rapidly.
- The reduction potentials of the species differ significantly. Under these conditions, deposition of the compound can occur in two ways: (i) by using a complexing agent, or (ii) through the formation of a compound with a favorable Gibbs free energy of formation (ΔG).

2.1.6 Deposition Potential and Role of Complexing Agents

When the ion to be deposited forms a complex, its deposition potential changes. Qualitatively, the deposition potential is shifted to more negative values as the stability of the complex increases, because additional energy is required to decomplex the ion. The tendency to form complexes varies significantly depending on the metallic ions involved. In general, transition metal ions form more stable complexes than other metals.

2.1.7 Kinetic Factors

The kinetic factors that can influence the electrodeposition of compounds are essentially of two types: those related to the reduction kinetics and those related to the deposited structure.
Concerning kinetic factors, the Butler-Volmer equation can be considered (neglecting stirring effects, ohmic drops, interaction energies, etc.), particularly in the high overpotential approximation. The deposition of species A and B can be controlled either by charge transfer**,** mass transport, or both:

$$I = Ai_0 \left\{ \exp\left[\frac{\tilde{\beta} nF}{RT}(E - E_{eq})\right] - \exp\left[\frac{(1-\tilde{\beta})nF}{RT}(E - E_{eq})\right] \right\} \quad (8)$$

where I is the current, A is the active cathodic surface area, i_0 is the exchange current density, E the electrode potential, Eeq the equilibrium potential, n the number of electrons involved in the electrode reaction, F the Faraday constant, R the gas constant, T the absolute temperature, and α the anodic transfer coefficient (symmetry factor).

2.1.8 General Summary Considerations

The above discussion can be summarized as follows: for the deposition of a single element (whether a metal or a semiconductor), the kinetic equation relating the deposition current to the applied potential is described by the Butler-Volmer equation**.**

The electrodeposition of a compound is more complex, as it requires simultaneous consideration of both thermodynamic and kinetic factors. Among the thermodynamic aspects, the variations in the activities of the individual components must be considered. The main kinetic factors are the exchange current density (j_0) and the charge transfer coefficient (α). During deposition, the relative magnitudes of these factors play a critical role in controlling the composition of the deposit.

In many technologically relevant compounds, one component is significantly more noble than the other. Consequently, the condition for codeposition can be achieved either by keeping the concentration of the more noble component low, making the deposition process diffusion-controlled, or by reducing its activity through the use of an appropriate complexing agent. Alternatively, deposition may occur when the standard Gibbs free energy of formation ($\Delta G°$) of the compound is favorable[2].

2.2 Electrochemistry of Silicon

Silicon, owing to its central importance in the electronics industry, is among the most extensively studied electrode materials in semiconductor electrochemistry. It exhibits a broad spectrum of electrochemical behaviors, ranging from electropolishing to porous silicon formation and current oscillations. Although many aspects of these phenomena are still not fully explained by existing theories, fundamental concepts and models remain essential for describing electrode processes across specific temporal and spatial scales, as well as for interpreting large-scale behaviors through the interplay of these processes [3]. In the context of an ideal semiconductor crystal at 0 K, its energy spectrum consists of two distinct bands: a higher-energy conduction band (Ec)**,** which is empty of electrons, and a lower-energy valence band (Ev)**,** fully occupied by electrons. Additionally, the electronic properties of a semiconductor are characterized by the Fermi level (Ef)**,** which represents the chemical potential of electrons within the semiconductor and describes the equilibrium distribution of charge carriers in the bands. Specifically, it is defined as the energy level at which the probability of occupation by an electron is ½ at thermal equilibrium.

The band gap (Eg = Ec - Ev) depends on the electronic structure and bonding characteristics of the material. For example, silicon has a band gap of 1.12 eV at 300 K. The electronic conductivity of semiconductors, as predicted by the band structure, can arise either from the intrinsic mobility of electrons in the crystal lattice **(**intrinsic conductivity) or from electrons introduced by impurities, defects, or dopants (extrinsic conductivity).

In intrinsic semiconductors at finite temperature, charge carriers are generated by thermal excitation of electrons from the valence band to the conduction band, simultaneously creating holes in the valence band. Under an electric field, these holes behave as positively charged particles, with a charge equal in magnitude but opposite in sign to that of electrons. Holes can move through the lattice as electrons fill the vacant positions, generating a current. In intrinsic semiconductors, the Fermi level lies at the midpoint of the band gap.

In extrinsic semiconductors, impurities, defects, or dopants introduce energy levels within the band gap, classified as donors or acceptors (**Figure 5**).

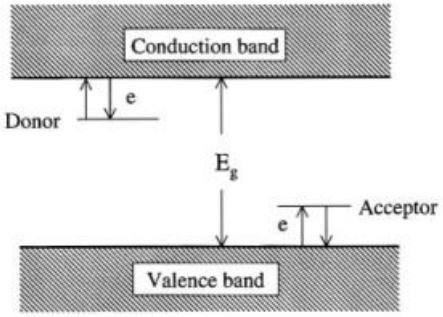

Figure 5 Energy level diagram for a semiconductor.

Donor dopants introduce energy levels close to the conduction band, allowing electrons to be thermally excited into the conduction band. This produces an excess of electrons and leads to the formation of n-type semiconductors (e.g., silicon doped with a group XV element such as phosphorus). Conversely, acceptor dopants introduce energy levels slightly above the valence band, capturing electrons from it and thereby generating an excess of holes, resulting in p-type semiconductors (e.g., silicon doped with a group XIII element such as aluminum).

The presence of dopants, defects, or impurities shifts the Fermi level toward one of the bands, altering the equilibrium distribution of charge carriers. In n-type semiconductors, the Fermi level lies just below the conduction band, whereas in p-type semiconductors it is positioned just above the valence band. As in metallic electrodes, the Fermi level of a semiconductor varies with the applied potential: shifting the potential toward more negative values raises the Fermi level[3].

Analogously, the energy levels of redox species in an electrolyte solution are described by the redox potential (E_{redox}), which expresses the tendency of chemical species to donate or accept electrons and can be regarded as the Fermi level of the solution[3].

At the ideal interface between a semiconductor and an electrolyte, equilibrium is established when their electrochemical potentials are equal ($E_f = E_{redox}$). The redox potential defines the electrochemical potential of the solution, while the semiconductor's potential is determined by its Fermi level. When these values differ, charge transfer occurs between the two phases until equilibrium is reached, producing a net charge at the semiconductor surface.

Unlike metallic electrodes, this excess charge penetrates into the semiconductor, forming a space-charge region that typically extends from 100 to 10,000 Å. This region generates an internal electric field, which adds to the interfacial field described by electric double-layer theory.

Under open-circuit conditions, the Fermi level of an n-type semiconductor generally lies above the redox potential of the electrolyte. As a result, electrons flow from the

semiconductor into the solution, leaving behind a positively charged depletion layer and inducing upward band bending.
For a p-type semiconductor, the Fermi level is typically lower than the redox potential of the electrolyte. As a result, electrons are transferred from the solution to the electrode, generating negative charge within the space-charge region and inducing downward band bending. In this case, the space-charge region corresponds to a depletion layer, as holes are depleted near the surface.
As in metallic electrodes, applying an external potential shifts the Fermi level of a semiconductor, particularly deep within the bulk. However, the band energies at the interface remain fixed, leading to varying degrees of band bending depending on the applied potential. Three regimes can be distinguished:

- Flatband condition: When the applied potential aligns the Fermi level with the redox potential, no net charge transfer occurs and the energy bands remain flat.
- Depletion region: Occurs at potentials more positive than the flatband potential for n-type semiconductors, or more negative for p-type.
- Accumulation region: Forms at potentials more negative than the flatband potential for n-type, or more positive for p-type semiconductors.

Charge-transfer kinetics depend strongly on the regime. In accumulation, the electrode behaves similarly to a metal, with abundant majority carriers enabling rapid charge transfer. In depletion, the scarcity of charge carriers limits electron exchange and reduces faradaic efficiency.
Under illumination, photons can excite electrons into the conduction band. If this excitation occurs within the space-charge region, the internal electric field separates the photogenerated electron–hole pairs, facilitating charge transfer across the interface. For instance, an n-type semiconductor at negative potentials acts as a cathode; further lowering the potential leads to a depletion region, which suppresses anodic current unless light generates additional holes. Upon illumination, these holes can accept electrons from the solution, thus producing anodic photocurrent.
In summary:

- n-type semiconductors act as cathodes at negative potentials, both in the dark and under illumination.
- At positive potentials, they behave as anodes only when illuminated.
- p-type semiconductors display the opposite behavior.

It is important to note that redox reactions are not completely inhibited during electrodeposition, even in the presence of a depletion region. The potential barrier at the semiconductor–electrolyte junction is often insufficient to fully suppress faradaic processes. Consequently, the interface frequently exhibits rectifying behavior analogous to that of a Schottky diode.
When a metal and a semiconductor come into direct contact, a potential barrier, known as the Schottky barrier, forms, preventing most charge carriers (electrons and

holes) from crossing the junction. This barrier allows current to flow primarily in one direction, unlike an ohmic contact, which permits bidirectional current flow. However, if the applied potential exceeds the barrier height (breakdown potential), current can also flow in the reverse direction, even in the presence of a depletion region.

A semiconductor–electrolyte interface exhibits similar behavior and is referred to as a Mott-Schottky junction[3,4]. However, there are key physicochemical differences between the two types of junctions:

- **Charge transfer** at a semiconductor–electrolyte interface is slow, while it is fast at a metal–semiconductor interface.
- **Redox species diffusion** in the electrolyte is slow, whereas charge carrier movement in metals is rapid.
- A **Helmholtz layer** forms at the semiconductor–electrolyte interface, but no such layer exists at a metal–semiconductor junction[3].

Silicon is a semiconductor with an intrinsic conductivity of 4.3×10^{-6} Ω^{-1} cm^{-1} and a band gap of 1.12 eV at 300 K. It has a diamond-like crystal structure, typical of elements with four covalently bonded atoms. Its lattice constant is 5.43 Å, with the nearest-neighbor atomic distance of 2.35 Å, and an atomic radius of 1.18 Å in the hard-sphere model.

In electronics, silicon is commonly doped to enhance conductivity. Typical electron donors include phosphorus, arsenic, and antimony; electron acceptors include boron, aluminum, and gallium.

For monocrystalline silicon, surface properties depend on crystal orientation, the (111) plane has the highest atomic density and lowest surface energy, while the (100) plane has the lowest atomic density and highest surface energy. The (100) plane has the highest surface bond density despite its low atomic density. Including in-plane bonds, absent in (100) and (111) but present in (110), the (110) plane has the highest total bond density. Surface free energy values also vary by plane, depending on bond density and strength.

Importantly, silicon surfaces are not atomically flat; they exhibit defects such as steps, vacancies, kinks, and terraces[3].

Silicon is a reactive element with a potential of –0.857 V vs SHE. According to its Pourbaix diagram silicon is thermodynamically unstable in aqueous environments, as its stability region lies well below the water stability line. Under these conditions, silicon tends to oxidize, forming hydrogen, silicic acids, gaseous SiH_4 (also unstable), SiO_2, and silicates.

However, the formation of a surface silicon oxide layer provides kinetic stabilization in many aqueous solutions. The diagram does not account for the complex nature of silicic acid species $[SiO_x(OH)_{4-2x}]_n$ or interactions with compounds forming insoluble salts or soluble complexes.

In the absence of fluoride ions, silicon oxide is poorly soluble in water and acidic solutions but becomes more soluble in alkaline media. At low dissolved silicon

concentrations ($<10^{-5}$ M), SiO_2 dissolves to form H_4SiO_4, a weak acid that dissociates significantly only at pH 10. At higher silicon activity ($>10^{-4}$ M), SiO_2 remains the stable phase in non-alkaline solutions.
Silica solubility increases with temperature and pressure, enhancing the stability of water molecules surrounding H_4SiO_4. Below 2 mM SiO_2, silica remains monomeric; above this threshold, polymeric forms become significant. Solubility also depends on other dissolved species and surface curvature.
In the presence of hydrofluoric acid (HF), silica dissolves to form highly stable fluorosilicates via (Equation 9)[3]:

$$SiO_2 + 4HF \rightleftarrows SiF_4 + 2H_2O \quad (9)$$

Silicon atoms at the outermost surface layer exhibit unsaturated bonds, known as dangling bonds, caused by the disruption of the crystal lattice periodicity. These atoms are highly reactive and readily interact with surrounding chemical species.
Silicon surfaces naturally react with atmospheric oxygen, forming a thin native oxide layer. In aqueous environments, the surface may terminate with hydrogen, hydroxyl groups, fluoride, or oxide, depending on the chemical conditions.
Surface characteristics can vary significantly based on cleaning and preparation methods. Contaminants such as metallic, organic, or ceramic residues are commonly observed[5].
In non-vacuum environments, the surface is rarely pristine due to the adsorption of various chemical species. The chemical nature, thickness, and composition of the surface termination depend heavily on the cleaning and preparation method.
For instance, treatment with hydrofluoric acid (HF) results in hydrogen-terminated silicon surfaces. In contrast, untreated surfaces are usually covered by a native oxide layer.
In hydrofluoric acid (HF) solutions, silicon surfaces are predominantly hydrogen-terminated, though small amounts of oxygen- and fluorine-terminated sites may also be present depending on conditions.
Hydrogen termination occurs rapidly, typically within one minute of immersion in HF, via chemical adsorption, forming covalent bonds with strength comparable to Si–Si bonds. This passivates and stabilizes the surface. Each surface silicon atom may bond with one, two, or three hydrogen atoms, depending on its geometric position in the surface lattice. Silicon surfaces treated with HF, whether (100) or (111) oriented, typically exhibit mono-, di-, and tri-hydride terminations. At the atomic scale, these surfaces are rough due to terraces, steps, and vacancies, and display a mix of (100), (111), and other crystallographic facets[6,7].
The prevalence of mono-, di-, or tri-hydride terminations on silicon surfaces depends on both crystallographic orientation and atomic-scale roughness. For example, (100) surfaces tend to form SiH_2 terminations, while (111) surfaces favor SiH or SiH_3, due to differences in dangling bond density. These variations stem from the distinct atomic packing of each crystal face.

Achieving a perfectly flat (100) surface with only SiH_2 terminations is challenging due to its high reactivity. The presence of significant amounts of mono- and tri-hydrides after HF treatment suggests atomic-scale roughness, as these terminations typically form at step edges where silicon atoms have single or triple dangling bonds. Thus, the type of hydride observed can serve as an indicator of surface roughness: a mix of all three types implies a rough surface, while predominantly mono-hydride terminations—common on (111) surfaces—indicate atomic flatness.

Selective HF treatments can yield nearly atomically flat (111) surfaces with mostly mono-hydride terminations. These treatments preferentially etch irregular features like steps, which are terminated by di- and tri-hydrides, while leaving mono-hydride-terminated atoms intact. Increased roughness on (111) surfaces is typically accompanied by the appearance of di- and tri-hydride species[3].

Silicon surfaces treated with hydrofluoric acid (HF) and terminated with hydrogen atoms are stable at room temperature, reacting slowly only with oxygen or water. The Si-H bond energy (~3–4 eV) is comparable to Si-Si, while Si-F bonds are stronger (~6–7 eV), making them thermodynamically more stable. However, Si-F terminated complexes are unstable in HF solution due to strong polarization of adjacent Si-SiF bonds, which facilitates further HF attack. This leads to the following reaction (Equation 10):

$$\mathrm{Si-SiF_3 + HF \rightleftharpoons Si-H + SiF_3} \tag{10}$$

Hydride formation (mono-, di-, tri-hydrides) depends on bond-breaking activation energies, as calculated by Trucks et al.[8] (**Table 1**).

Table 1 Activation energies of silicon surface reactions with HF.

Reaction	Activation Energy (eV)
$Si–OH + HF \rightarrow Si–F + H_2O$	0.55
$Si–SiF_3 + HF \rightarrow Si–H + SiF_4$	1.00
$Si–SiH_3 + HF \rightarrow Si–H + SiH_3F$	1.60
$Si–H + HF \rightarrow Si–F + H_2$	1.20

The first reaction is the most favorable, indicating Si–OH groups are highly unstable in HF. The second reaction is kinetically preferred, promoting hydrogen termination over fluorine.

Minimal electronegativity difference between Si–H and Si–Si bonds ensures low polarization and surface stability.

Di- and tri-hydrides are more easily removed in aqueous solutions due to increased bond polarization, making SiH_2 and SiH_3 less stable than SiH.

Native silicon oxide (SiO_2) forms spontaneously when silicon is exposed to air or immersed in solution. This thin, chemically inert layer passivates the surface, protecting it from corrosion and making it suitable for electronic applications, where SiO_2 also serves as an effective insulator.

In electrochemical experiments, the native oxide alters the electrode's behavior and is typically removed with hydrofluoric acid (HF), resulting in a hydrogen-terminated surface. Oxide regrowth begins immediately upon air exposure, with rates depending on surface condition, air purity, and substrate properties. Clean surfaces oxidize rapidly, while HF-treated ones show slower growth due to hydrogen passivation.

Oxide formation also varies with surface chemistry: hydrophilic surfaces tend to form hydrated SiO_2 during cleaning, whereas hydrophobic ones initially develop suboxides that later convert to SiO_2. Growth rates increase significantly with high dopant concentrations ($>10^{19}$ cm^{-3}), are higher on n-type than p-type silicon, and are faster on (111) crystal orientations compared to (100)[9].

In aqueous environments, silicon surfaces are continuously covered by a thin oxide film, regardless of initial conditions. However, the oxide thickness and growth rate depend on the surface state and the concentration of dissolved oxygen. Using low-oxygen solutions significantly slows oxide formation.

Graf et al.[10] described the oxidation mechanism for HF-treated silicon in water as a sequence of reactions. Initially, Si-F groups are replaced by Si-OH through hydrolysis. The high electronegativity of OH weakens adjacent Si-SiOH bonds, making them susceptible to further attack. This leads to the formation of Si-H, which is then replaced by Si-OH. Ultimately, Si-OH groups condense to form Si-O-Si bridges, completing the oxide network.

Oxide growth in both air and water involves significant electrochemical contributions. It is influenced by dopant concentration, the presence of oxidants such as oxygen or hydrogen peroxide, anodic polarization, and metallic submonolayers. Despite this, existing models of native oxide formation do not account for these electrochemical effects.

3 Electrodeposition of MnAs-Based Thin-Film for Spintronics

The first phase of this study was devoted to the electrodeposition of an alloy possessing structural and functional properties aligned with the objectives of the present doctoral research. In particular, the alloy was selected to enable the viable electrodeposition of thin films and to provide functional properties relevant to spintronic and energy-related applications. Specifically, suitability as a spin-injection material, high carrier spin polarization, a small coercive field, relatively high saturation magnetization, and an elevated Curie temperature were considered key selection criteria.

3.1 Introduction

The discovery of the giant magnetoresistance (GMR) effect in 1988 revolutionized the field of computer science and initiated a new field called spintronics, which led to the 2007 Nobel Prize in Physics[11]. The field of "spintronics", a name given by the combination of the words "*spin transport electronics",* studies the intrinsic spin of the electron and its associated magnetic moment, jointly with its fundamental electronic charge in solid-state devices[12]. The combined contribution of both electron spin and electron charge facilitate electronic functions, enabling one extra degree of freedom for information processing.

The spintronics field has rapidly grown over the past years with significant discoveries, technological advancements, material studies, and device developments leading to numerous product applications: magnetic field sensors, magnetic resonance imaging (MRI) systems, and extremely low-power replacements for the Complementary metal–oxide–semiconductor (CMOS) transistors[11,12,13].

Heusler alloys are particularly suitable for spintronic applications because they exhibit almost complete spin-polarized electron conduction and interesting magnetic properties[14,15,16]. Heusler alloys are a class of intermetallic materials characterized by the general formula X_2YZ or XYZ (the latter often referred to as Half-Heusler), where X and Y are typically transition metals (not necessarily different from each other), and Z is an element that can belong to groups 13, 14 and 15 of the periodic system. Heusler alloys exhibit a special crystal structure and may present a unique combination of properties, including ferromagnetism, shape memory effect, and half-metallicity. A half-metal is any substance that acts as a conductor to electrons of one spin orientation but as an insulator or semiconductor to those of the opposite orientation[17,18,19].

The versatile nature and tunable properties of Heusler alloys make them a promising material for many applications such as thermoelectronics, energy production, spintronics, and quantum computing, enabling devices based on multifunctional properties that could revolutionize technological applications.

The most common methods of synthesizing bulk Heusler compounds include arc-fusion using stoichiometric quantities of highly pure elements, mechanical alloying,

sputtering, solid-state reaction, and molecular beam epitaxy (MBE)[20,21,22]. Physical and/or vapor phase deposition techniques can produce materials with very few defects; however, they are complex to manage and typically very expensive.
Spintronic devices can be realized in metals or ferromagnetic semiconductors, also known as dilute magnetic semiconductors (DMSs)[23]. Among spintronic materials, thin-film synthesis methods reported in the literature include physical vapor deposition (PVD), MBE, Direct current (DC), Radio Frequency (RF), and ion beam sputtering (IBS), pulsed laser deposition (PLD)[24], and the sol–gel method[25,26].
These type of thin films can be used in microelectronics and device manufacturing that require miniaturization, down to micron and sub-micron sizes, exploiting material properties in new, size-reduced devices[27].
The idea behind this work is to try to provide alternative materials for achieving spintronic devices through electrodeposition, a procedure that is not widely covered in this field according to the current state of the art[28,29]. Compared with the most common production processes for these kinds of compounds, electrodeposition offers a simpler experimental setup, allowing to work at ambient temperature and pressure conditions and in an aqueous solution without the use of toxic solvents, providing clear environmental advantages. Moreover, it is less expensive, offers high deposition rates, is easily scalable, allows excellent control of the deposition thickness and morphology, and it is also possible to vary the properties of the product by adjusting the operating conditions[30].
MnAs has shown the capability to be used as a spin injection material, featuring large carrier spin polarization, a small coercive field, relatively high saturation magnetization[27], and a Curie temperature (Tc) of 313-318 K, unlike many ferromagnetic semiconductors with lower Tc[31]. In the literature, it is reported that at the Curie temperature, the first-order phase transition occurs from hexagonal (NiAs-type) to orthorhombic (MnP-type), accompanied by a ferromagnetic-paramagnetic transition[32,33].
Electrochemically obtaining a film of MnAs has clear advantages when compared to the methods reported in the literature, such as high-temperature MBE[34].
The selection of the compound to be synthesized was based on the work of Ma et al., who evaluated the spintronic properties of all possible Heusler alloys using DFT calculations[35,36]. Among these alloys, manganese arsenides were identified as the compounds of interest for this study. Previous work has shown the possibility of obtaining MnAs magnetic devices integrated with Si circuits, corroborating the potential of the examined compound[37,38].
To the best of our knowledge, there are no articles in the literature addressing the electrodeposition of MnAs.
Electrodeposition of manganese is a non-trivial task due to a low current efficiency, high cell voltage, and the catalyzation of hydrogen evolution during manganese deposition. Manganese is conventionally electrodeposited from ammonium sulfate media in a diaphragm cell, which is mainly used to mitigate the oxidation of manganese in solution in contact with the anode[39]. With increasing deposition time,

the manganese deposit gradually becomes rougher and more dendritic, increasing the rate of manganese dissolution. In most articles present in the literature, $NaAsO_2$ is used as a precursor for the electrodeposition of arsenic[40].

Firstly, the alloy to be deposited was identified, the solubility of possible compounds to be used was evaluated, and electrochemical studies of all employed compounds were performed using cyclic voltammetry techniques. The optimal operating pH was identified as a trade-off between the solubility of the chemical species used and deposition potentials, also utilizing Pourbaix diagrams[41]. The effects of deposition time and the presence of O_2 during the potentiostatic experiment on the morphology of the obtained deposits, the chemical species to be used, and their optimal concentrations were assessed. The use of different substrates was investigated, and the best deposition potential was identified to achieve deposition with a 2:1 Mn/As stoichiometry. This was obtained using multivariate analysis to find optimized operating conditions.

The deposits were characterized by analyzing their morphology and composition using a Scanning Electron Microscope equipped with Energy Dispersive X-ray Spectroscopy (SEM-EDS) and X-Ray Diffraction (XRD) analyses. The resulting images show the formation of a thin film on the gold-coated silicon wafer. X-ray Photoelectron Spectroscopy (XPS) and XRD investigations confirmed the presence of MnAs and MnO_2, which are of great interest in the field of spintronics[42,43].

The magnetic properties of the obtained sample were characterized by magnetometry using a SQUID apparatus.

3.2 Experimental

Reagents

All the solutions were prepared using ultrapure water (< 0.059 μS/cm). All reagents were of analytical grade and were used as received without further purification. The following reagents were used: nitric acid HNO_3 (69.5%) was used to clean the anode; hydrogen peroxide H_2O_2 (30%) was used in the treatment of the cathode; potassium hydroxide KOH 0.1 M and sulfuric acid H_2SO_4 0.1 M were used to correct the pH; all the above-mentioned reagents were obtained from Carlo Erba, Val de Reuil, France. Sodium arsenite $NaAsO_2$ in various concentrations, manganese (II) sulfate monohydrate $MnSO_4 \cdot H_2O$ 0.1 M, and ammonium sulfate $(NH_4)_2SO_4$ 0.1 M aqueous solutions were used to carry out the electrodeposition; potassium persulfate $K_2S_2O_8$ 0.07 M was used in the treatment of cathode; the above-mentioned reagents were obtained from Merck KGaA, Darmstadt, Germany.

$NaAsO_2$ was chosen as the precursor for the electrodeposition of arsenic because it is widely used in many articles in the literature[40]. $MnSO_4$ was used because electrolytic manganese is conventionally produced from ammonium sulfate media[44]. Ammonium sulfate plays two important roles: first, it increases the solution's conductivity, thereby decreasing the cell voltage and reducing energy consumption; second, it buffers the pH and forms manganese–ammonia complexes, preventing the precipitation of manganese hydroxides and oxides at the cathode surface in a neutral or weak alkaline solution[44].

Experimental set-up

The electrochemical measurements were conducted using a three-electrode setup: the working electrode (WE) was a commercial (100) silicon wafer, 0.75 ± 0.025 mm thick, and coated with approximately 100 nm of gold (111) (Siegert Wafer). The adhesion layer between Si and Au comprised approximately 10 nm of Ti. Ag/AgCl sat. KCl served as the reference electrode (RE), and a platinum mesh acted as the counter electrode (CE). A 5 mm diameter glassy carbon (GC) WE was also used for preliminary studies. A tailor-made electrochemical cell made of polypropylene (PP) was utilized.

The structure of the electrochemical cell was specifically designed for this work: a cylinder with a diameter of 2.2 cm and a height of 2.2 cm. At the bottom of the cell is a hole, 8.5 mm in diameter, through which the WE was in contact with the solution (**Figure 6**). The total solution volume in the cell was approximately 8 mL. This setup ensures reproducible measurements by maintaining a prefixed solution volume, constant deposition area, and fixed electrode position. The electrolyte was renewed after each electrodeposition.

In this work, a diaphragm cell was not used to avoid complicating the experimental setup. Anodizing problems were mitigated using an anode with a much larger area than the working electrode and employing short deposition times.

The "Autolab PGSTAT204" galvanostat-potentiometer from METROHM S.R.L. was used for all electrochemical analyses performed using NOVA software from Metrohm Autolab.
Density-Functional Theory (DFT) calculations reported were conducted using the Vienna Ab-Initio Simulation Package (VASP), employing a plane wave basis set and projector-augmented wave (PAW) based pseudo-potentials. A cut-off energy of 520 eV was chosen for all calculations, and the *k* points were generated over a 15 × 15 × 15 Γ-centered Monkhorst-Pack grid. The Perdew-Burke-Ernzerhof (PBE) version of the generalized gradient approximation (GGA) for the exchange-correlation functional of DFT was adopted.
SEM images and analyses were acquired using a Hitachi SU3800 equipped with an Ultim Max 40 Analytical Silicon Drift EDS Detector. EDS-SEM measurements performed at 10 kV were used to analyze the Lα (1.28 keV) emission of As and the Kα (5.89 keV) emission of Mn. SE-SEM and BSE-SEM images were obtained at 5 kV.
XRD diffractograms were acquired using a "Bruker New D8 Da Vinci" diffractometer (Cu-Kα1 radiation = 1.54056 Å, 40 kV × 40 mA), equipped with an Euler cradle and a "Bruker LYNXEYE-XE" detector. The Powder X-ray Diffraction (PXRD) technique was employed, and the results are based on the database PDF-4+ 2021 (ICDD). The measurement conditions included a fixed incident θ angle of 1.7° (grazing), 2θ scanning in an interval between 25 and 80°, with an increment of 0.03°, and a time per step of 5 s. The Grazing Incidence X-ray Diffraction (GIXD) technique was utilized to minimize the contribution of the underlying gold to the deposit. A 0D detector was used, and a mirror was implemented in the instrumental setup to maximize the focus on the sample.
XPS was performed using an instrument equipped with a non-monochromatic X-ray source (VSW Scientific Instrument Limited model TA10, Al Kα radiation 1486.6 eV[45]), operating at 120 W (12 kV and 10 mA) and a hemispherical analyzer (VSW Scientific Instrument Limited model HA100). The analyzer was equipped with a 16-channel detector and a dedicated differential pumping system maintaining the pressure in the chamber below the 10^{-8} mbar range. The pass energy was set to 22 eV. The measured spectra were analyzed using CasaXPS software (version 2.3.19, Casa Software Ltd., Teignmouth, UK). The inelastic background was subtracted using Shirley's method[46], and mixed Gaussian and Lorentzian contributions were used for each component. Charge referencing of the binding energy (BE) scale of the spectra was obtained by shifting to the lowest component relative to the 1s transition of carbon for adventitious carbon[47].
Field-dependent direct current (DC) magnetic measurements were conducted using a Quantum Design MPMS SQUID magnetometer at 5 K and 300 K, with the field oriented parallel to the sample plane.

a **b**

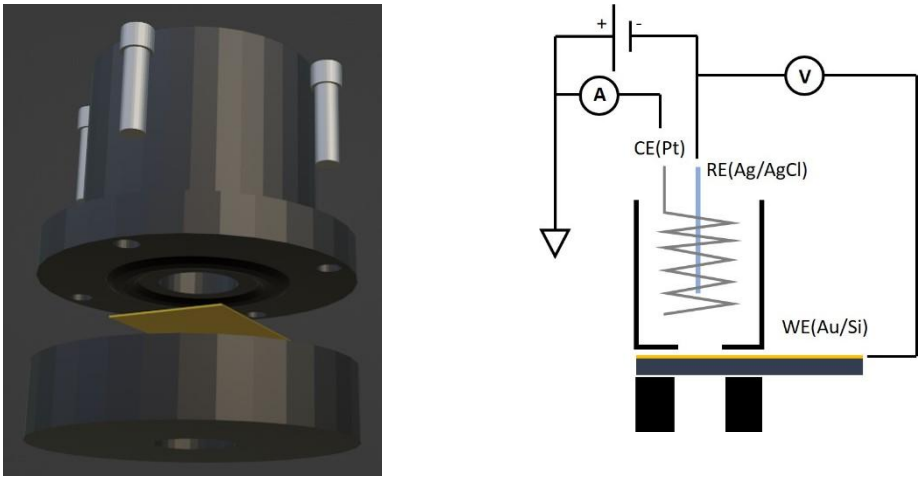

Figure 6 (**a**) 3D model of the electrochemical cell used; (**b**) Schematic view of the experimental setup.

3.3 Results and discussion

Identification of the Heusler Compound

The first step in this work was to identify the Heusler alloy for electrodeposition. Utilizing the Heusler database of the Center for Materials for Information Technology at the University of Alabama, a systematic search was conducted among all the possible alloys in the database[35,36].

The database authors calculated the electronic and magnetic properties of 180 full, 378 half, and 408 inverse Heusler alloys using the density-functional theory (DFT). Alloys of the formula X_2YZ and XYZ (Half-Heusler) were evaluated, with X = Co, Cr, Fe, Mn, Ni, Cu, Sc, Ti, Rh, Ru, V; Y = Co, Cr, Fe, Mn, Ni, Cu, Zn, Sc, Ti, V; and Z = Al, As, Ga, Ge, In, P, Sb, Si, Sn. Initially, alloys with a spin polarization at Fermi level of >95% and a low saturation magnetization (below 250 emu/cc) were selected, as these are key characteristics in spintronics applications[14]. Subsequently, compounds with a formation energy of less than 0 were chosen. The alloys meeting these criteria were further assessed based on their electrochemical behavior using Pourbaix diagrams.

At the conclusion of this process, the alloy with the formula MnMnAs was selected. The fact that the compound consists of only two elements offers the advantage of simplifying the electrochemical deposition process. The calculated characteristics of this alloy are 100% spin polarization at the Fermi level with a gap width of 1.112 eV, a formation energy of -0.131 eV/atm, and a saturation magnetization of 207.85 emu/cc[35].

Electrochemical study

The electrochemical behavior of the precursors was evaluated on GC to exploit its wide potential window[48]. The pH of the solution was selected based on the Pourbaix diagrams of the precursors. It was determined that the optimal pH is 7 considering the formation of MnO_2 at a more alkaline pH and the challenges in reducing manganese at a more acidic pH. It was observed that the manganese-containing solution tends to form a milky suspension in a basic environment, which eventually takes on a pink-orange coloration over time. X-ray diffraction analysis performed on the precipitate revealed the presence of Mn_3O_4 in the crystal structure.

All electrochemical solutions used in this phase of the research were deaerated by bubbling nitrogen gas to minimize oxide formation during the electrochemical study and reduce the intensity of oxidation and oxygen reduction peaks. During the deaeration, the pH drifted to more alkaline values, so, it was readjusted to 7 before the electrochemical measurements.

The cyclic voltammetry (CV) of arsenic was investigated (**Figure 7a**), and the effect of $NaAsO_2$ concentration on the deposition potential of As was evaluated. From the 5 CVs obtained from solutions containing concentrations ranging from 0 to 0.05 M of $NaAsO_2$, it is evident that the reduction potential of the As^{3+} shifts to more negative potentials as the concentration of $NaAsO_2$ decreases. The reduction for the solution containing As 5 mM begins around -1.6 V, while for the solution with As

50 mM, it starts around -1.2 V. The deposition of As appears to be irreversible, as no evident anodic peaks are visible in the return scan. Only low anodic currents were recorded around 1.0 V in the case of As 5 mM solution and at -0.2 V for the solution with As 0.05 M.
The electrochemical behavior of manganese is illustrated in **Figure 7b**. Comparing the CVs performed with 0.01 M and 0.1 M $MnSO_4$ solutions respectively, it can be concluded that the Mn(II) concentration in solution, in these conditions, does not significantly influence the deposition potential of manganese, in fact, the reduction starts around -1.4 V for both solutions. An anodic peak is present near the reduction onset, attributed to the redissolution of the metal to Mn^{2+}, the other anodic peaks are given by the great variety of oxidation numbers that manganese can assume and the relatively high oxidation potential applied. Regardless, the focus of this article is not on the behavior of manganese at oxidation potentials.
Finally, CVs in the presence of Mn (0.1 M) and As (0.035 M) simultaneously in solution were conducted. The concentration of $NaAsO_2$ was chosen to approach a hypothetical codeposition potential. In **Figure 7c,** only one reduction peak is observed, in addition to the hydrogen discharge, suggesting the presence of codeposition.
The reduction peak starts around -1.2 V, similar to the onset potential observed in the CV relative to the $NaAsO_2$ 0.035 M, $(NH_4)_2SO_4$ 0.1 M solution. The oxidation peak starts at -0.9 V, a potential greater than the anodic peak observed in the CV relative to the $MnSO_4$ 0.1 M, $(NH_4)_2SO_4$ 0.1 M solution, possibly due to the preferential oxidation of manganese, rather than the stripping of MnAs.

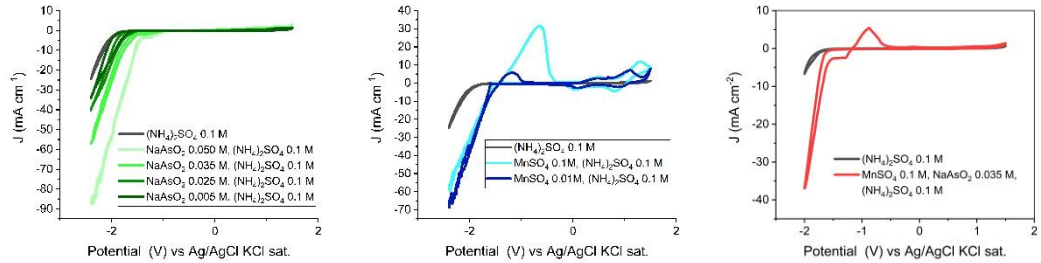

Figure 7 (**a**) CV of $(NH_4)_2SO_4$ 0.1 M and $NaAsO_2$ at various concentrations (0.005 M, 0.025 M, 0.035 M, 0.05 M) solutions compared with $(NH_4)_2SO_4$ 0.1 M solution, between −2.4 V and 1.5 V, scan rate 50 mV s−1, pH 7, on GC WE; (**b)** CV of $(NH_4)_2SO_4$ 0.1 M and $MnSO_4$ at concentrations of 0.01 M and 0.1 M solutions compared with $(NH_4)_2SO_4$ 0.1 M solution, between −2.4 V and 1.5 V, scan rate 50 mV s−1, pH 7, on GC WE; (**c**) CV of $(NH_4)_2SO_4$ 0.1 M, $MnSO_4$ 0.1 M and $NaAsO_2$ 0.035 M solution compared with $(NH_4)_2SO_4$ 0.1 M solution between −2.0 V and 1.5 V, scan rate 50 mV s−1, pH 7, on GC WE.

After conducting the electrochemical study on GC, the same measurements were repeated also on gold. The overall behavior observed on GC was confirmed, but the

reduced electrochemical window on gold did not permit observation of all the details seen on GC. Again, a trend compatible with codeposition was observed.

Optimization of the electrodeposition

A preliminary deposition was performed on silicon wafers coated with a gold thin film, applying -1.6 V vs Ag/AgCl in KCl sat. for 300 s in a non-deaerated solution containing 0.02 M $NaAsO_2$, 0.1 M $MnSO_4$, 0.1 M, and $(NH_4)_2SO_4$.

The resulting deposit was analyzed through SEM-EDS (**Figure 8**), which proved the presence of a deposit containing both As and Mn (15.6 at% Mn and 7.9% As). O and C, accounted for 46.0% and 13.6%, respectively. The high oxygen concentration is likely due to oxide formation during the time between deposition and spectroscopic measurements, as well as reactions between Mn and H_2O. The substrate contribution was 12.3% of Au and 2.9% of Si. Other contaminants were present at 1.7%.

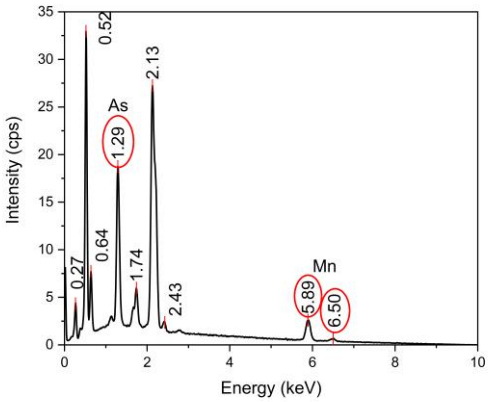

Figure 8 EDS-SEM analysis conducted at 300x magnification, on the deposit obtained at a potential of −1.6 V vs Ag/AgCl in KCl sat. for 300 s, on silicon wafers coated with gold thin film, in a solution of 0.02 M $NaAsO_2$, 0.1 M $MnSO_4$ and $(NH_4)_2SO_4$ 0.1 M.

SEM-EDS analysis performed on small areas with a homogeneous deposit and without dendritic structures showed an Mn/As molar ratio close to 2. EDS-SEM measurements at 5 kV yielded lower manganese concentrations than those obtained at 10 kV, indicating a lower presence of manganese on the surface.

SEM morphology analysis of the sample clearly revealed the presence of a deposit (**Figure 9a)**. The film exhibited poor adhesion to the substrate, with partial detachment and the presence of rolled ribbons, indicative of high tensile stresses. Two distinct morphological structures were observed: a continuous film and a

dispersed globular deposit. For a more comprehensive evaluation of the deposit's morphology, a cross-section of the wafer was performed (**Figure 9b**), revealing a film thickness of a few hundred nanometers, classifying it as a thin film[49]. The irregular structures were a few micrometers tall.

a **b**

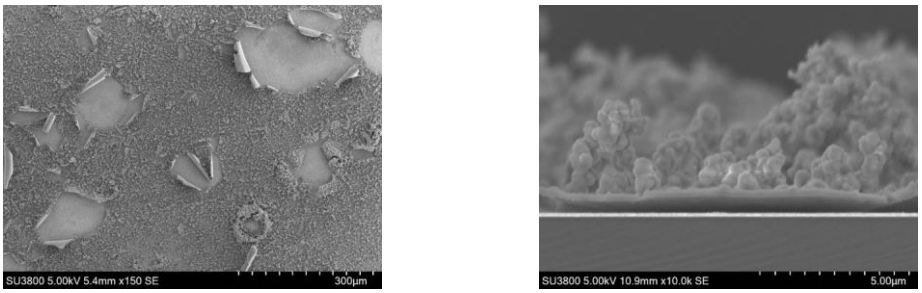

Figure 9 (**a**) SE-SEM image of the deposit obtained at a potential of −1.6 V vs Ag/AgCl in KCl sat. for 300 s, on silicon wafers coated with gold thin film, in a solution of 0.02 M $NaAsO_2$, 0.1 M $MnSO_4$ and $(NH_4)_2SO_4$ 0.1 M. (**b**) Cross-section SE-SEM image of the deposit obtained at a potential of −1.6 V vs Ag/AgCl in KCl sat. for 300 s, on silicon wafers coated with a gold thin film, in a solution of 0.02 M $NaAsO_2$, 0.1 M $MnSO_4$ and $(NH_4)_2SO_4$ 0.1 M.

The globular structures were situated above the deposited film.
To mitigate the tensile stresses in the deposit, the deposition time was reduced to 30 s. Despite varying the duration of the deposition, large quantities of oxygen persisted in the deposit, and although reduced, irregular structures were still present atop the continuous film deposit (**Figure 10a)**. Consequently, the possibility of further reducing the presence of oxygen during the experiments was assessed. Electrochemical depositions were conducted by excluding oxygen from the solution via nitrogen gas in the experimental environment, and using a glove box to exclude oxygen in the whole process: both during the deposition (**Figure 10b**) and in storage (**Figure 10c**). Reducing the deposition time significantly impacted film adhesion, and deaerating the solution diminished the number of globular deposits above the continuous film, though they did not entirely disappear.

a **b** **c**

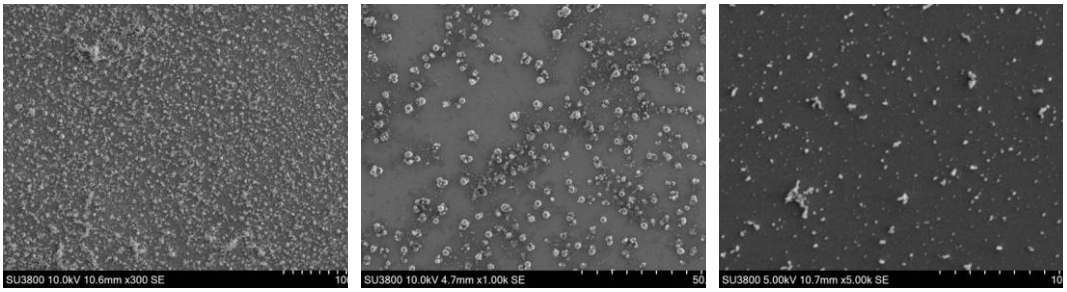

Figure 10 SE-SEM analysis of the deposit obtained at a potential of −1.6 V vs Ag/AgCl in KCl sat. for 30 s, on silicon wafers coated with gold thin film, in a solution of 0.02 M $NaAsO_2$, 0.1 M $MnSO_4$ and $(NH_4)_2SO_4$ 0.1 M. (**a**) SE-SEM image of the surface of the sample obtained without oxygen exclusion during the deposition; (**b**) SE-SEM image of the surface of the sample obtained with oxygen exclusion during the deposition; (**c**) SE-SEM image of the surface of the sample prepared and stored under N^2 atmosphere using a glove box.

After determining that a 30-second deposition conducted in an oxygen-free environment yielded the best results, these parameters were fixed and a systematic experimental campaign was conducted by varying the arsenic concentration and the deposition potential to optimize the Mn/As atomic ratio. The experimental design considered two independent variables: the deposition potential (−1.6 V, −1.8 V, and −2.0 V vs Ag/AgCl) and the $NaAsO_2$ concentration (0.020 M, 0.035 M, and 0.050 M), while the concentrations of $MnSO_4$ (0.1 M) and $(NH_4)_2SO_4$ (0.1 M) were kept constant. The response variable was the Mn/As atomic ratio, determined by EDS-SEM analyses. Multivariate data analysis was performed using the Design-Expert software. The model was constructed using compositional data obtained from EDS-SEM analyses carried out at an accelerating voltage of 10 kV, as these measurements were found to be more representative of the bulk composition than those acquired at 5 kV, which were more affected by surface oxidation and contamination effects. The EDS-SEM results were further cross-validated with quantitative compositional estimates obtained using the PyMca software, based on XRF spectra acquired at 50 kV. For completeness, EDS-SEM data acquired at 5 kV were also evaluated but subsequently excluded from the multivariate model. The Mn/As atomic ratio for all samples is provided in **Table 2**. Additionally, adventitious signals of carbon and gold from the substrate were also detected.

Table 2 Stoichiometric ratios (Mn/As) obtained from EDS-SEM analyses performed on deposits obtained from chronoamperometric deposition at -1.6 V, -1.8 V and -2.0 V and with a solution containing $MnSO_4$ 0.1 M, $(NH_4)_2SO_4$ 0.1 M, and variable concentrations of $NaAsO_2$: 0.020 M, 0.035 M and 0.050 M. The reported errors are calculated based on three independent measurements.

E_{Dep} vs Ag/AgCl in KCl sat. (V)	[As] (mM)	Mn/As atm
-1.6	20	1.59 ± 0.09
-1.8	20	1.89 ± 0.04
-2.0	20	2.32 ± 0.06
-1.6	35	1.91 ± 0.16
-1.8	35	2.15 ± 0.07
-2.0	35	2.23 ± 0.11
-1.6	50	2.17 ± 0.04
-1.8	50	2.22 ± 0.04
-2.0	50	2.18 ± 0.04

The experimental data were initially analyzed using a two-factor interaction (2FI) model, in which the applied reduction potential (factor A) and the precursor concentration (factor B) were treated as independent variables. The resulting model was statistically significant, with a Model F-value of 11.26, corresponding to a probability of only 1.16% that such a value could arise from random noise. The p value was 0.0116, p-values lower than 0.0500 were considered significant. The coefficient of determination (R^2) for the 2FI model was 0.8711, indicating a satisfactory description of the experimental variability. Adequate Precision, which measures the signal-to-noise ratio, yielded a value of 9.640, well above the minimum desirable threshold of 4. Optimization was performed by applying a desirability function approach, targeting an atomic Mn/As ratio of 2:1, with maximum weighting assigned at both the lower and upper bounds and centered on the target value. The resulting 2FI model equation is: $Y = -4.18854 - 3.28609A + 0.116750B + 0.060026AB$. The experimentally optimal conditions, however, were ultimately identified using a quadratic desirability model, defined as the intersection point of the maximum relative desirability derived from SEM analyses performed at 10 kV and from XRF data processed using the PyMCA software. In this final step, second-degree polynomial fits were applied separately to the EDS-SEM and XR.
. The implemented dataset and model fitting are shown in **Figure 11**.

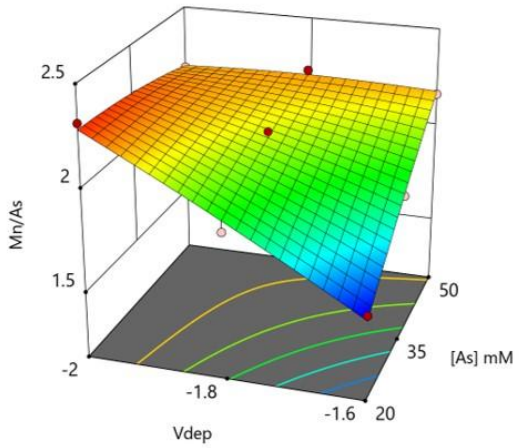

Figure 11 Graphical representation of the data obtained by multivariate analysis using Design Expert software.

By imposing the constraint of a stoichiometric Mn/As ratio equal to 2:1, the multivariate model predicted optimal deposition conditions corresponding to a deposition potential of −1.664 V vs Ag/AgCl and a $NaAsO_2$ concentration of 0.043 M. To validate the model prediction, three independent depositions were performed under the optimized conditions on three different electrodes. EDS-SEM analysis yielded an average Mn/As atomic ratio of 2.01 ± 0.08, confirming the reliability of the multivariate optimization.
Further characterizations were carried out on samples prepared under these optimized conditions.

Compositional and crystallographic characterization
XPS analyses were employed to characterize the electrodeposited material (**Figure 12**).

a **b**

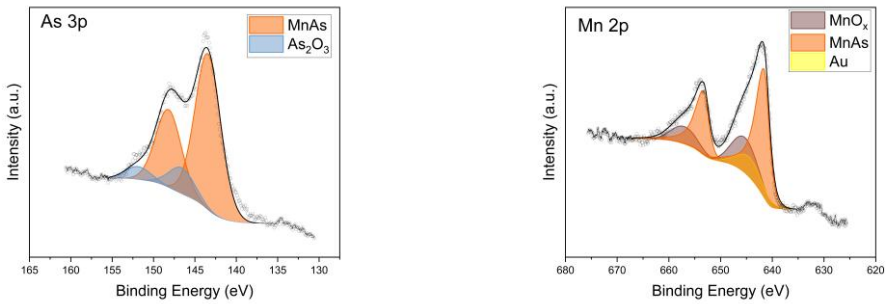

Figure 12 XPS spectra of deposits obtained on silicon wafers coated with gold thin film by chronoamperometry at a potential of −1.66 V vs Ag/AgCl, in 0.043 M $NaAsO_2$, $MnSO_4$ 0.1 M and $(NH_4)_2SO_4$ 0.1 M solution, (**a**) In As 3p region; (**b**) In Mn2p region.

Few authors have reported XPS studies concerning MnAs[50,51,52].The As 3p and Mn 2p regions were examined. Although the As 3d core level is generally preferred for arsenic chemical state analysis and As Auger transitions can provide complementary information for speciation, their application was limited in the present study. Only low-resolution Auger features were observed in the XPS survey spectra, where an arsenic-related Auger signal was detected in the region near 270 eV. However, the limited energy resolution and signal-to-noise ratio of these features did not allow a reliable chemical state determination based on Auger parameters.With regard to the core-level analysis, the As 3d spectral region was found to strongly overlap with the Mn 3p signal, which is particularly intense in the Mn-rich deposits investigated. This overlap prevented a reliable deconvolution and quantitative interpretation of the As 3d components. Consequently, the As 3p region, which appeared better resolved and less affected by spectral interference under the present experimental conditions, was selected for the identification and qualitative analysis of arsenic in the samples.
In the As region, two signals compatible with As 3p3/2 were identified: one more intense centered at 143.4 eV, consistent with the MnAs intermetallic compound, and the other signal, less intense and centered at 146.6 eV, attributed to As_2O_3 resulting from the partial oxidation of the deposit[53,54]. In the Mn 2p3/2 region, three signals were observed: (i) at 641.6 eV, attributable to MnAs[55]; (ii) at 644.3 eV, attributable to the Au 4p1/2 of the substrate; (iii) one at and one at 644.3 eV, compatible with manganese oxides[56]. The behavior of compounds consisting of elements of similar electronegativity, such as MnSb, was also observed to gather additional information. The report by Biesinger et al.[57] was also used to evaluate the manganese environment.

Normalization of the areas subtended by the peaks was performed using the Atomic Sensitivity Factors (ASFs) of the Handbook of Photoelectron Spectroscopy [54] and the data from the Elettra Sincrotrone Trieste[58,59].
The signal attributed to MnAs represented 70% of the total Mn. The total Mn/As ratio was found to be 1.3, contrary to the results obtained with EDS-SEM analysis. This discrepancy is likely due to the superficial nature of the technique, consistent with the results of EDS-SEM analyses performed at 5 kV, which provided lower stoichiometric Mn/As ratios than analyses performed at 10 kV. The normalized area subtended by the peaks for Mn_{MnAs} and As_{MnAs} had a ratio of 1.06, corroborating the presence of MnAs. The presence of significant oxygen content, even in the case of samples obtained and stored in a deaerated environment, is probably due to reactions of the metals with H_2O.
XPS results indicated the presence of As and Mn primarily in the form of MnAs and Mn oxides, suggesting that the deposit did not consist of the Half-Heusler alloy MnMnAs. Therefore, the crystalline structure of the sample has been evaluated.
In the literature, crystal structures of α-birnessite, H-birnessite, and Krautite are often reported for structures containing Mn and As[60,61]. However, these structures did not yield significant Figure of Merit (FOM) values in any of the diffractograms obtained. Consequently, it can be concluded that the deposit did not exhibit such crystalline structures.
There is limited information in the literature on the crystalline structure of electrochemically obtained thin films of MnAs. However, several papers describe the crystalline structure and magnetic properties of MnAs thin films epitaxially grown on GaAs by MBE[33,27,62]**.** It is noted that the magnetic properties depends on the crystalline structure of the deposit[33].
MnAs layers epitaxially grown on GaAs by MBE exhibit a very complex domain structure in their demagnetized state, with an average domain size of approximately 0.5 μm by 1.5 μm[62]. In a 300 nm thin film, the large anisotropic lattice mismatch induces epitaxial strain, which the system relieves by inserting over a large temperature range around RT β-MnAs domains, which have a smaller lattice mismatch with the substrate. The lattice parameter discontinuity between α and β-phases translates into the onset of a characteristic stripe pattern of alternating ridges and grooves along the MnAs $[11\bar{2}0]$ direction[27]. The width of the α and β stripes depends both on the temperature and film thickness, while the period of the stripes increases linearly with the thickness and does not depend on the temperature.
The strain induced by the strong lattice mismatch with the GaAs substrate is strongly temperature dependent[27]. The phase coexistence range is directly linked to the strain relaxation and thus to the film thickness and the growth conditions. Due to the large atomic lattice parameter difference between the hexagonal and the orthorhombic phase, a 1.7% corrugation with respect to the film thickness, is reported within the phase coexistence temperature range[27].
Since the case treated in this article is not found in the literature, it was essential to carry out a crystallographic characterization of the samples obtained. XRD analyses

were conducted on samples obtained in a deaerated environment, derived from deposits produced on silicon wafers coated with a gold thin film by chronoamperometry for 30 s at a potential of -1.66 V vs Ag/AgCl, in a solution containing 0.043 M $NaAsO_2$, 0.1 M $MnSO_4$, and 0.1 M $(NH_4)_2SO_4$. The XRD results are depicted in **Figure 13**.

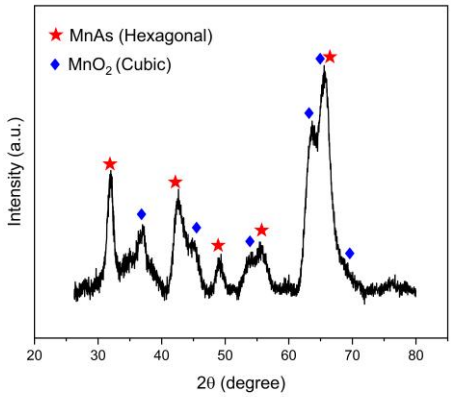

Figure 13 Diffractogram concerning XRD analysis on a deposit obtained on silicon wafers coated with a gold thin film by chronoamperometry for 30 s at a potential of −1.664 V vs Ag/AgCl, in 0.043 M $NaAsO_2$, 0.1 M $MnSO_4$, and $(NH_4)_2SO_4$ 0.1 M solution. 2θ scanning, in an interval between 25 and 80°, with a time per step of 5 s, an θ angle of 1.7°(grazing), and an increment of 0.03°.

The Grazing Incidence X-ray Diffraction (GIXD) technique was employed to minimize the contribution of gold and silicon from the wafer. The structure showing the highest correspondence was hexagonal MnAs, with cubic and orthorhombic (Ramsdellite) MnO_2 also relevant, confirming results obtained from XPS analysis. Compared to the results obtained without the use of deaeration during deposition, diffractograms with fewer peaks were observed, possibly due to the structure having fewer crystal structures within it. However, the structures most frequently observed in deposits that did not undergo deaeration were hexagonal MnAs and cubic MnO_2, although the presence of other structures with a relatively low FOM, such as tetragonal Mn_2As, cannot be excluded.
The accuracy of powder XRD phase analysis was assessed utilizing the Pawley Fitting[63]. Refined lattice parameters, crystallite size (Double Voight Approach, evaluating the Integral Breadth IB), and dislocation density for each phase are reported in **Table 3**.

Table 3 Refined lattice parameters, crystallite size (Double Voight Approach,

evaluating the IB) and dislocation density of MnAs, MnO_2 (Cubic), and MnO_2 (Orthorhombic).

	Crystallite size (nm)	Dislocation density ($1/nm^2$)	Lattice parameters (Å)
MnAs	4.1 ± 0.8	0.059 ± 0.016	a = 3.711 ± 0.004 c = 5.69 ± 0.01
MnO_2 (Cubic)	4.4 ± 1.4	0.052 ± 0.02	a = 8.015 ± 0.008
MnO_2 (Orthorhombic)	3.3 ± 0.9	0.092 ± 0.04	a = 4.67 ± 0.05 b = 9.28 ± 0.04 c =2.91 ± 0.06

The weighted profile R-factor (Rwp) is 2.337. The mean linear intercept method[64] was utilized to estimate the grain size, yielding a value of 70 ± 11 nm (the reported error is calculated based on ten independent measurements). The relative texture coefficient (RTC)[65] was extrapolated using the spectrum calculated using Mercury software (Crystal Structure Visualization, Exploration and Analysis software) from the Crystallographic Information File (CIF) of hexagonal MnAs[66]. The plane (103) of hexagonal MnAs was found to be preferentially parallel to the (111) plane of gold, with the in-plane lattice constant of hexagonal MnAs 3.71 Å and that of gold 4.17 Å, resulting in a considerable strain of 12.4%, indicating a significative mismatch between the substrate and MnAs.

It is important to underline that, the influence of lattice mismatch and the different linear thermal expansion coefficients of the film and the substrate can affect the lattice parameters[67,68].

The results obtained from the previously reported analyses suggest that the deposit is mainly composed of MnAs and MnO_2[69]. These chemical species contained in the electrochemically deposited thin film are very interesting as they both have properties suitable for applications in spintronics[70,42].

MnAs is a half-metal[71] typically obtained through physical deposition, it presents ferromagnetic properties, and spin anisotropy, which are key features for spintronic applications[18,72]. Previous papers in the literature report how an MnAs deposit was obtained by physical deposition and had interesting properties of ferromagnetism and spin anisotropy[72]. To the best of our knowledge, there is no literature on the electrodeposition of MnAs; therefore, the results obtained are noteworthy. The combined deposition of two chemical species with properties suitable for application in the field of spintronics in the form of thin films arouses considerable interest.

Using the Open Quantum Materials Database (OQMD)[73], a database of DFT-calculated thermodynamic and structural properties, it was possible to assess that in an Mn-As system, the most stable species is MnAs, although Mn_2As is still a stable species, as is Mn_3As. These assessments were confirmed by the data from the

Materials Project[74], an open-access database based on DFT calculations. The predicted formation energy of Mn_2As is -0.161 eV/atom, but this compound is predicted not to be stable; in fact, it tends to dismutate to MnAs and metallic Mn. On the other hand, the predicted formation energy of MnAs is -0.265 eV/atom, and this chemical species is predicted to be stable.
The reactions involved in the degradation of the compound, which are in accordance with our results, are as follows:

$$Mn_2As \rightleftharpoons MnAs + Mn \quad (11)$$

$$Mn + 2H_2O \rightleftharpoons MnO_2 + 4H_2 \quad (12)$$

Magnetic study
In the literature, it is noted that in a MnAs thin film epitaxially grown on GaAs by MBE, α-MnAs has a large negative magnetocrystalline anisotropy with three easy $[11\bar{2}0]$ axis in the basal plane and a hard axis perpendicular to it (c-axis). As a consequence, the magnetization is pointing perpendicular to the stripe direction, predominantly in-plane. This leads to a complicated, thickness-dependent magnetic domain structure in the interior of the α-phase. Starting from a critical thickness ($\geq$ 100 nm), the demagnetization energy induced by the lateral confinement of the α-phase, is reduced by the formation of 3D flux-closure domains at the cost of the exchange energy. Three magnetic configurations are generally observed: Type I (S and/or Landau states), type II (diamond state) and type III (double diamond state). The prevalence of three domain configurations depends on the film thickness and the temperature[27].
For p-type ferromagnetic (Ga,Mn)As, a diluted magnetic semiconductor, the ferromagnetic transition temperatures calculated based on the Ruderman-Kittel-Kasuya-Yosida (RKKY) interaction using the exchange reproduce remarkably well the observed ferromagnetic transition temperatures, demonstrating that ferromagnetism of (Ga,Mn)As has its origin in the RKKY interaction mediated by holes[75].
However, it is important to note that there is limited literature available on the properties of electrodeposited MnAs thin films, thus emphasizing the innovation brought by this work.
For this reason, the deposit obtained under the optimized conditions was further characterized using the magnetometry SQUID technique to evaluate its magnetic properties[76]. Two hysteresis measurements were performed: one at 5 K and the other at 300 K to better evaluate the magnetic behavior of the deposit as the temperature changes.
The results are shown in **Figure 14**, where the values on the Y-axis are normalized to the saturation magnetization[77].

a **b**

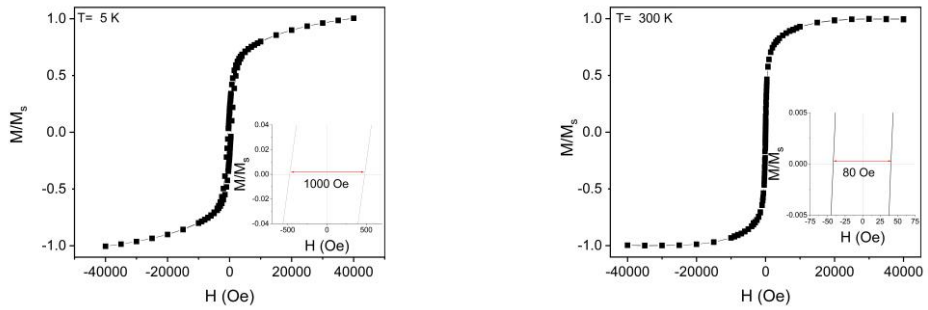

Figure 14 Magnetic hysteresis loops measured with a SQUID magnetometer on a sample obtained by chronoamperometry for 30 s, at a potential of −1.66 V vs Ag/AgCl, in a solution of $NaAsO_2$ 0.043 M, $MnSO_4$ 0.1 M and $(NH_4)_2SO_4$ 0.1 M. Y-axis values normalized to saturation magnetization. (**a**) operating temperature 5 K; (**b**) operating temperature 300 K.

The two insets make it possible to assess the coercive field; for the analysis obtained at 5 K, it is about 1000 Oe, while for the other temperature, it is about 80 Oe. As expected the coercive field decreases with the increase in temperature.
These results are encouraging evidence of the magnetic properties of the deposit. In the literature, MnAs is reported to be a ferromagnetic compound[78] and the hysteresis loop shown above clearly exhibits a ferromagnetic component. Previous studies have reported that a MnO_2 monolayer presents a Tc of 140 K[79], while a thin film of MnAs on GaAs (23 nm) presents a Tc greater than 350 K[80]. Looking at the results related to the magnetic study, it is possible to conclude that the Tc of the deposit is above 300 K.

3.4 Conclusions

In this work, a MnAs-based thin film was successfully co-electrodeposited subsequent to research aimed at identifying the most promising material for electrodeposition. This represents a novel advancement in the field with no prior literature precedent to the best of our knowledge.

Additionally, MnAs and MnO_2, chemical species contained in the electrochemically deposited thin film, present properties suitable for applications in spintronics, as reported in the literature.

The magnetic study conducted through the magnetometry SQUID technique showed the presence of a ferromagnetic component even at 300 K.

It has thus been demonstrated that a MnAs-based film with interesting magnetic properties can be electrochemically deposited, indicating that electrochemistry may play a role in the hot field of spintronics and next-gen devices.

An interesting further step forward for this work could be the realization of a spintronic device based on MnAs thin film obtained following the co-electrodeposition procedure proposed here.

4 Electrodeposition of Nanostructured Metals on n-Type Silicon with Focus on Rhodium

The second stage of this doctoral research focused on deepening the understanding of metal electrodeposition processes on silicon substrates. Particular attention was given to the formation and characterization of metallic nanostructures, with the aim of elucidating the fundamental mechanisms governing nucleation, growth, and film morphology. This study provided essential insights into the interaction between metallic species and semiconductor surfaces, forming the experimental basis for subsequent investigations on silicon.

4.1 Introduction

The electrodeposition of metal films, patterns, and nanostructured materials on silicon substrates provides a means to combine the desirable properties of metals with the exceptional electronic properties of silicon, providing useful tools in the fields of integrated circuits, electrodes in batteries, supercapacitors, fuel cells, sensors, water-splitting devices, and photovoltaic cells[81–83].

Currently, thin film depositions on silicon are obtained mainly using vapor deposition methods. Among physical deposition methods are physical vapor deposition (PVD)[84], including vacuum evaporation[85], molecular beam epitaxy (MBE)[86], sputtering[87], and pulsed laser deposition (PLD)[88]. Other physical techniques for thin film synthesis include spin coating[89] and spray coating[90].

On the other hand, the electrodeposition of thin films and metal nanoparticles onto semiconductors offers numerous advantages and presents high technological importance, especially for metal/semiconductor contacts. This deposition technique is an inexpensive, easily scalable, and quick synthesis route that shows low costs, is carried out at room temperature and atmospheric pressure, in aqueous solution, and with adjustable deposit properties[91].

Electrochemical Atomic Layer Deposition (E-ALD) allows the deposition of variable thickness thin films on an electrode substrate, controlling the morphology and composition of the deposited film with a low percentage of defects and contaminations[92]. This technique also enables the deposition of atomic monolayers by utilizing surface-limited reactions (SLRs), such as underpotential deposition (UPD)[93,94]. Furthermore, E-ALD is often limited by the need to use substrates with high crystalline order, exhibiting a strong affinity for deposition and allowing morphologically ordered growth. As a result, this technique has primarily focused on the use of crystalline gold[95] and silver substrates[96].

However, due to the high cost of these materials, their widespread industrial use for thin film production is currently challenging. Instead, the use of monocrystalline silicon wafers represents a viable alternative as substrates, thanks to the relatively low cost and the large availability due to the abundance of Si in the Earth's crust and the large production for the electronics sector.

Despite UPD offering greater quantitative control over the deposition process, electroless deposition has garnered significant interest due to its simplicity. The latter technique is particularly studied for metals like copper (Cu), gold (Au), and platinum (Pt) due to their excellent conductivity and chemical stability in technological contexts, such as microelectronics[97]. The field of electrodeposition of metals on silicon still presents great room for improvement in semiconductor–metal contact technology [3], and it shows technological relevance, as it leads to the formation of the Schottky barrier[98]. This barrier allows conduction in one polarity but not in the opposite, making it crucial for various applications in electronics. When a semiconductor comes into contact with an electrolyte during the deposition process, the resulting barrier is known as the Mott–Schottky junction[99]. The deposition of a continuous ultrathin film (<50 nm) onto silicon is not straightforward due to the band structure of the semiconductor, which affects both the thermodynamics and the kinetics of metal deposition processes[100–102]. Most of the literature reports on the deposition of rather thick and clustered films. An excellent example of an ultra-thin film is reported by Allongue with the production of a continuous epitaxial gold film of just 4 nm under the mass transport limit[102]. However, there is still no evidence of works in which an SLR is reported.

In this paper, the deposition of technologically relevant metals on silicon substrates through electrodeposition was investigated, exploring the possibility of obtaining monolayers, thin films, and nanostructured deposits. A metal monolayer can serve as a platform for further surface functionalization, such as introducing functional groups, nanoparticles, or molecular species onto the surface. This could open up possibilities for applications in molecular electronics, biosensors, and surface-enhanced spectroscopies.

The first selection of metals to be electroplated was made through the evaluation of Density Functional Theory (DFT) calculations, considering the metal–silicon formation energy, allowing the evaluation of which metals had a higher affinity with silicon compared to the metal itself[103].

Voltammetric studies were carried out using solutions containing the metals Mn, Co, Ni, Ru, Pd, Rh, and Pt to investigate the presence of cathodic processes related to metal deposition processes. The possibility of obtaining atomic monolayers or ultra-thin deposits was evaluated. The risk of uncontrolled electroless depositions was also assessed.

Finally, controlled charge electrodeposition measurements were performed on the most promising metal. Rhodium showed the best results; therefore, multi-cycle charge-controlled depositions were performed to evaluate the possibility of obtaining a tunable nanostructured deposit and/or a thin film. To the best of our knowledge, there are limited studies specifically addressing the electrodeposition of nanostructured rhodium on silicon substrates[104]. Electrodeposition of nanostructured rhodium metal on silicon and the ability to achieve different surface coverings as operating conditions change is an important result for many high-impact technology applications, especially in hydrogen and oxygen evolution reactions, thanks to the

excellent catalytic properties of rhodium[105,106]. Moreover, rhodium-coated silicon can be used to develop sensitive and selective sensors[107], robust interconnects and contacts in semiconductor devices, and to fabricate nanoscale electronic devices[108], to improve the efficiency of silicon-based solar cells[109], in the development of LEDs, where the rhodium layer can enhance the emission efficiency[110], and in corrosion resistance and protective coatings that extend the lifespan and reliability of electronic and mechanical components[111]. The results obtained in this work show potential applications in the cutting-edge fields of photonic devices for scalable quantum information applications[112], enhanced electrocatalytic oxidations in direct alcohol fuel cells[113], and photoinduced wave modulation using hybrid metal–silicon met surfaces[114].

4.2 Materials and Methods

Reagents

All the solutions were prepared using ultrapure water (<0.059 μS/cm). All reagents were of analytical grade and were used as received without further purification. The following reagents were used for the RCA (Radio Corporation of America) procedure[115,116] for the activation of the silicon electrode: sulfuric acid H_2SO_4 (98%) supplied by chemPUR, Karlsruhe, Germany; hydrochloric acid HCl (37% w/w) and hydrofluoric acid HF (48% w/w) from VWR International, Fontenay-sous-Bois, France; acetone AcOH, ethanol EtOH, and hydrogen peroxide H_2O_2 (30% w/w) supplied by Carlo Erba, Val de Reuil, France. The following salts were used for the electrolytic solutions: rhodium (III) chloride hydrate $RhCl_3 \cdot xH_2O$, supplied by chemPUR, Karlsruhe, Germany; potassium (II) tetrachloroplatinate K_2PtCl_4, and cobalt (II) sulfate heptahydrate $CoSO_4 \cdot 7H_2O$, by Sigma-Aldrich, St. Louis, MO, USA; manganese (II) sulfate monohydrate $MnSO_4 \cdot H_2O$, fromMerck KGaA, Darmstadt, Germany; Hexaammineruthenium (III) chloride $[Ru(NH_3)_6]Cl_3$, supplied by Acros Organics, Geel, Belgium; tetraammine palladium (II) sulfate, $[Pd(NH_3)_4]SO_4$, by Thermo Fisher Scientific, Waltham, MA, USA; nickel (II) sulfate hexahydrate $NiSO_4 \cdot 6H_2O$ from Carlo Erba, Val de Reuil, France. For the studies conducted in this work, metal solutions with a concentration of 1 mM metal salt in 0.1M sulfuric acid were used. Furthermore, a 0.1M sulfuric acid solution was prepared for instrument treatment and reference measurements.

Experimental Setup

The experimental setup used in this work for the electrochemical characterization and deposition is a fully computerized system that allows control over the solution input and permanence time in the cell using a solenoid valve system[117,118]. The solutions are stored in Pyrex glass, and deaerated with nitrogen gas, and are remotely injected in a Kel-F (polychlorotrifluoroethylene) electrochemical cell.

The potentiostat used is an AMEL, Model 551, and the personal computer is equipped with a National Instruments data acquisition card. A three-electrode setup was used: a monocrystalline (100) n-Si (0.1–1 Ω·cm) working electrode, with an exposed electrode surface of 0.785 cm^2; a gold counter electrode; and an Ag/AgCl saturated KCl reference electrode. All cyclic voltammetry measurements were conducted at a scan rate of 10 mV/s.

Before the measurements, the silicon electrodes were cleaned and activated using the RCA method.

The procedure can be summarized in **Table 4:**

Table 4 RCA Procedure Summary.

Step	Process	Duration
1	H_2SO_4-H_2O_2(4:1)	5 minutes
2	milliQ.	5 minutes sonication
3	H_2SO_4-H_2O_2(4:1)	5 minutes
4	milliQ	5 minutes sonication
5	H_2SO_4-H_2O_2(4:1)	5 minutes
6	milliQ	5 minutes sonication
7	H_2SO_4-H_2O_2(4:1)	5 minutes
8	milliQ	5 minutes sonication
9	NH_4OH-H_2O_2-H_2O (0.05:1:5), 90 °C	10 minutes
10	milliQ	Few seconds
11	AcOH	10 minutes (sonication)
12	EtOH	10 minutes (sonication)

SEM analyses were performed using a Hitachi SU3800 (Hitachi High-Tech Corporation, Tokyo, Japan) that was equipped with an Ultim Max 40 Analytical Silicon Drift EDS Detector (Oxford Instruments plc, Abingdon, UK). EDS measurements were carried out using the Layer Probe program of AZteclive (Version 5.0) to investigate the average equivalent thickness of the metallic rhodium deposit.

XPS was performed using an instrument equipped with a non-monochromatic X-ray source (VSW Scientific Instrument Limited model TA10, Al Kα radiation 1486.6 eV[45], set to work at 120W (12 kV and 10 mA), and a hemispherical analyzer (VSW Scientific Instrument Limited model HA100, Manchester, UK). The analyzer was equipped with a 16-channel detector and a dedicated differential pumping system maintaining the pressure in the chamber below the 10−8 mbar range. The pass energy was set to 22 eV. The measured spectra were analyzed using CasaXPS software (version 2.3.19, Casa Software Ltd., Teignmouth, UK). The inelastic background was subtracted using Shirley's method[46], and mixed Gaussian (70%) and Lorentzian (30%) contributions were used for each component. Charge referencing of the binding energy scale was performed by imposing the lowest component relative to the 1 s transition of carbon for adventitious carbon at 284.8 eV and the signal of elemental silicon at 99.4 eV[47,119]. For the fitting of each peak of the three elements analyzed, the Handbook of Photoelectron Spectroscopy was consulted[54].

4.3 Results and Discussion

Metals' Selection

The initial selection of metals for the electrodeposition on the silicon substrate was conducted through the study of the data obtained from computational calculations thanks to The Open Quantum Materials Database (OQMD)[73] based on Density Functional Theory (DFT) at the PBE/PAW level. The data were also compared with those of the Formation Energy Predictor[120–122] data mining algorithms of Northwestern University (Evanston, IL, USA) using PRB'14, ICDM'16, and ElemNet models and Material Project[123] DFT calculations at the PBE/PAWlevel. The data obtained from these alternatives is mostly in line with OQMD results.

Figure 15 reports the formation energies (eV/atom) of each element with silicon, considering the most stable phase. This study focused on identifying elements with favorable formation energies for bonding with silicon.

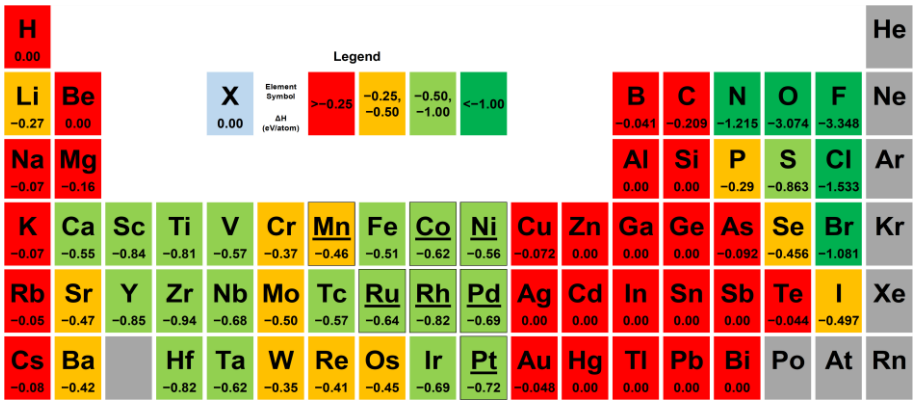

Figure 15 Periodic table of elements highlighting the formation energy (eV/atom) with silicon; the metals used in this work are highlighted (nickel, ruthenium palladium, rhodium, platinum, manganese, and cobalt).

The feasibility of electrodeposition of the elements was also evaluated[123], as well as observing the theoretical value of the metal–silicon Schottky barrier, which is a factor to consider for device applications[124]. For instance, in an ohmic contact, a very low Schottky barrier is preferable to obtain a linear current with no potential barrier in either direction; in fact, the lower the barrier height, the lower the specific contact resistivity is[125]. After considering the above, the following metals were selected: nickel, ruthenium, palladium, rhodium, platinum, manganese, and cobalt.

The possibility of achieving electroless deposition for all the metals used in this paper was also evaluated. If a metal undergoes electroless deposition under these experimental conditions, that metal is not ideal for achieving controlled deposition. Only the Pt-containing solution showed clear signs of electroless deposition.

Cyclic Voltammetry Measurements and Characterization

CVs were performed, using solutions containing the metal salts, to investigate the presence of any faradic processes associated with reduction reactions that could be attributable to the electrodeposition of the metals. The measurements were carried out by first performing cyclovoltammetries with the blank solution (0.1 M H_2SO_4) only, so as to have a term of comparison between the CV concerning the metal solution and the CV of the supporting electrolyte, both carried out in the chosen range. The potential range selected was −0.6 V to 0 V vs. Ag/AgCl/sat. KCl to avoid hydrogen evolution at the low potential end and oxidation of the silicon surface at more positive potentials. For each session of cyclovoltammetry measurements with a given metal solution, three CVs were performed with the metal solution, reciprocating the solution within the electrochemical cell after each CV scan. Finally, the electrochemical cell was washed several times with the washing solution, i.e., the supporting electrolyte.

The CVs obtained for each solution are given in **Figure 16**. CVs were performed in the potential range of −0.6 V to 0 V vs. Ag/AgCl/KCl (sat.), with a 10 mV/s scan rate, H_2SO_4 0.1 M solution (black scans), H_2SO_4 0.1 M, 1 mM metal solution, the first metal solution scan (red), the second metal solution scan (blue), and the third metal solution scans (green) relative to (a) Ni ($NiSO_4 \cdot 6H_2O$); (b) Pd ($[Pd(NH_3)_4]SO_4$); (c) Pt (K_2PtCl_4); (d) Rh ($RhCl_3 \cdot xH_2O$); and (e) Ru ($[Ru(NH_3)_6]Cl_3$). In the first scan (red curve) of the CVs of the solution containing nickel (**Figure 16a**), it is possible to observe an onset of a weak and broad peak covered by the hydrogen evolution, which is not present in the second and third CVs (blue and green curves). The hypothesis could be of a possible UPD. This would suggest a particular affinity of nickel toward the substrate and thus its deposition at a less negative potential than the reduction potential predicted by the Nernst equation[126].

Subsequent depositions hypothetically would be metal on metal and consequently at more negative potentials, which is perhaps why no cathode peaks are observed in the other two CV scans.

a

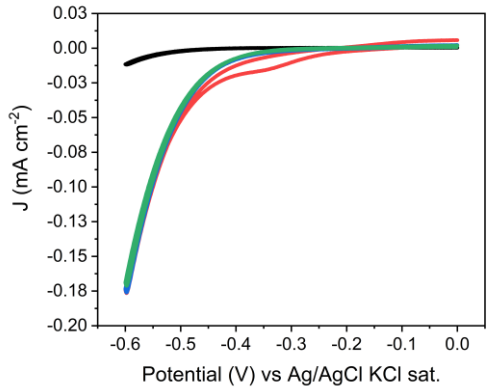
0.03
0.00
-0.03
-0.05
-0.08
-0.10
-0.13
-0.15
-0.18
-0.20
J (mA cm-2)
-0.6 -0.5 -0.4 -0.3 -0.2 -0.1 0.0
Potential (V) vs Ag/AgCl KCl sat.

b

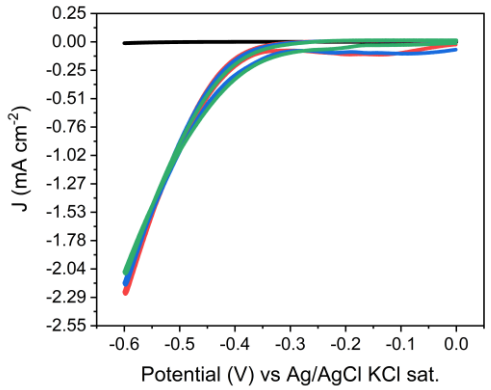
0.25
0.00
-0.25
-0.51
-0.76
-1.02
-1.27
-1.53
-1.78
-2.04
-2.29
-2.55
J (mA cm-2)
-0.6 -0.5 -0.4 -0.3 -0.2 -0.1 0.0
Potential (V) vs Ag/AgCl KCl sat.

c

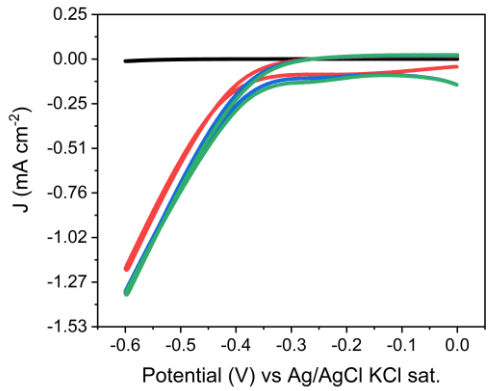
0.25
0.00
-0.25
-0.51
-0.76
-1.02
-1.27
-1.53
J (mA cm-2)
-0.6 -0.5 -0.4 -0.3 -0.2 -0.1 0.0
Potential (V) vs Ag/AgCl KCl sat.

d

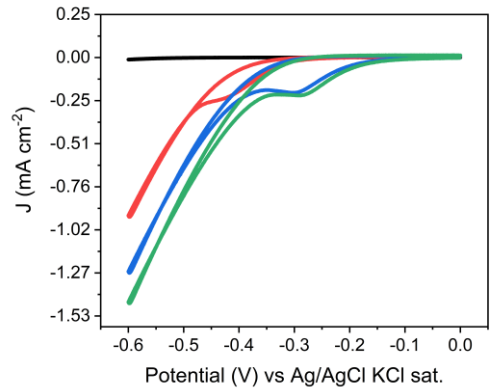
0.25
0.00
-0.25
-0.51
-0.76
-1.02
-1.27
-1.53
J (mA cm-2)
-0.6 -0.5 -0.4 -0.3 -0.2 -0.1 0.0
Potential (V) vs Ag/AgCl KCl sat.

e

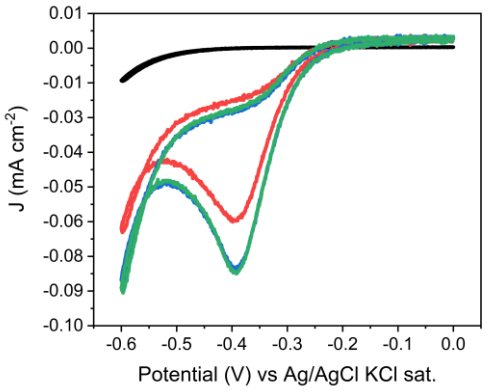
0.01
0.00
-0.01
-0.03
-0.04
-0.05
-0.06
-0.08
-0.09
-0.10
J (mA cm-2)
-0.6 -0.5 -0.4 -0.3 -0.2 -0.1 0.0
Potential (V) vs Ag/AgCl KCl sat.

Figure 16 CVs performed in the potential range of −0.6 V to 0 V vs. Ag/AgCl/KCl (sat.), 10 mV/s scan rate, H_2SO_4 0.1 M solution (black scans), H_2SO_4 0.1 M, 1 mM metal solution, first metal solution scan (red), second metal solution scan (blue), and the third metal solution scans (green) relative to (**a**) Ni ($NiSO_4 \cdot 6H_2O$); (**b**) Pd ($[Pd(NH_3)_4]SO_4$); (**c**) Pt (K_2PtCl_4); (**d**) Rh ($RhCl_3 \cdot xH_2O$); and (**e**) Ru ($[Ru(NH_3)_6]Cl_3$).

In the CVs of palladium solution (**Figure 16b**), the first two scans (blue and red curves) show very similar trends, while for the last CV (green), the trend is different, probably a symptom of a change in the electrode surface. In the first two CVs, two cathodic peaks very close to each other are observed, while in the last scan, only a rather broadened peak is present, partially overlapped by the onset of hydrogen evolution. Moreover, cathodic currents already begin to develop at 0 V. The observed cathodic currents are very high since the deposited palladium is an efficient catalyst for hydrogen evolution[127].
In the CVs of the platinum salt solution (**Figure 16c**), rather high cathodic currents are observed already at a potential of 0 V. This is probably due to the fact that the reduction in Pt (II) to Pt occurs already at 0 V. In the second and third CVs (blue and green), a shift in the curve to more positive potential is observed, probably due to a change in the surface area and thus a hypothetical metal deposition. The observed cathodic currents are very high since the deposited platinum is a well-known catalyst for hydrogen evolution[128].
The rhodium solution (**Figure 16d**) first scan shows the onset of a rather broadened peak, attributable to the reduction in the metal, which at lower potentials is covered by the cathodic current due to the evolution of hydrogen. Subsequent scans show a broadened peak again attributable to metal reduction; also, a shift in the cathodic peak to more positive potential is noted, probably due to metal deposition. The observed cathodic currents are very high, as in the previous cases; rhodium is a catalyst for the evolution of hydrogen[129].
The CVs of the ruthenium solution (**Figure 16e**) (red, blue, and green curves) all show a reduction peak centered at a potential of −0.4 V attributed to the reduction of Ru(III) to Ru(II)[130].
The CVs of the metal solution containing cobalt and manganese showed a similar trend to the scan performed with the supporting electrolyte, so it is assumed the exclusion of cathodic processes is attributable to a reduction in the metal ion.
No anodic peaks related to silicon oxidation are observed in the CVs in **Figure 16**, which is probably related to the value of the metal–silicon Schottky barrier; a higher potential may be needed to overcome the Schottky barrier, resulting in an increased onset potential for redox reactions[124,131].
Contrary to what is typically observed in the literature[91], no crossover (e.g., no overpotential deposition) was observed in the CVs, confirming the high affinity of the metals with silicon.

The silicon electrodes used during the cyclic voltammetry measurements were analyzed by SEM-EDS in order to evaluate the morphology and composition of the surface and consequently to assess the presence of a metal deposit. SEM analysis conducted on electrodes used in CVs showed the presence of a metallic deposit for Pd, Pt, and Rh; this is confirmed by both morphological and compositional characterization **Figure 17**. The observed particles are within the nanometer size range. One possible explanation for the variation in particle sizes between the three metals is the difference in nucleation overpotentials among palladium, platinum, and rhodium, which results in varying numbers of nucleation sites. Additionally, differences in surface energy between the three metals may also contribute to the differences in particle size.

These results agree with the cathodic peaks present in the CVs performed using the solutions of these metals. In the EDS spectra, in addition to the peaks relating to the metals, which can be clearly observed for Pd, Pt, and Rh, the peaks of the silicon substrate, carbon, and oxygen due to the air contamination are also recognizable. As expected, the intensity of the peaks corresponding to the metals is relatively low due to the little amount of the deposit.

In contrast, no metal was detected for Mn, Co, Ni, and Ru. The SEM EDS results of cobalt and manganese agree with what was observed in the CVs. For ruthenium, the results are consistent if the cathodic peaks are attributed to the reduction of Ru (III) to Ru (II) (**Figure 16e**). In the case of nickel, a cathodic peak was observed in the CVs, but it did not give evidence of the metal deposition by SEM-EDS.

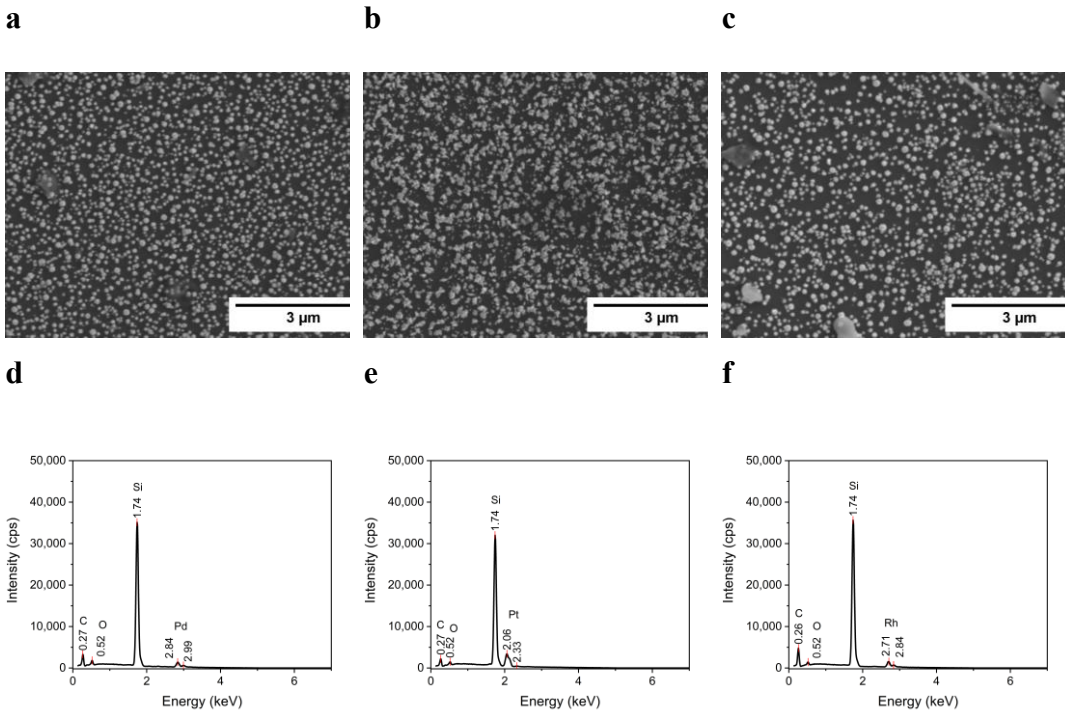

Figure 17 SE-SEM images and EDS-SEM spectra of the Si working electrode after the cyclovoltammetry measurements in H_2SO_4 0.1 M, 1 mM metal solution relative to (**a,d**) 1 mM $[Pd(NH_3)_4]SO_4$ solution; (**b,e**) 1 mM K_2PtCl_4 solution; (**c,f**) 1 mM $RhCl_3$ solution.

Charge-Controlled Deposition

Charge-controlled deposition of Ni, Ru, Pd, Rh, and Pt was attempted to deposit the equivalent amount of a single monolayer[117]. The theoretical deposition charge was calculated using Faraday's laws, considering the silicon lattice constant of 543.09 pm[132], its face-centered cubic (FCC) crystal structure[3], and the 100 exposed face. The moles required to coat the substrate with a monolayer have been calculated, considering the stoichiometric silicon-metal combination that is most thermodynamically stable. The most stable phases formed by silicon and the deposited metal were identified using "the Open Quantum Materials Database" (OQMD)[73]. The calculated charge was increased by 15% to consider capacitive contributions. The properties of the metals, the estimated charges, and deposition potentials derived previously from the peaks present in the CVs are summarized in **Table 5**.

Table 5 Experimental parameters for charge-controlled deposition of Rh, Pt, Pd, Ru, and Ni.

	Oxidation number of the metal in the salt	Metal/silicon most stable stoichiometry	Number of electrons exchanged	Charge (μC)	Peak potential
Rh	3+	1:1	3	256 + 15%	-0.425 V
Pt	2+	1:2	4	341 + 15%	-0.150 V
Pd	2+	1:2	4	341 + 15%	-0.170 V
Ru	3+	1:1	3	256 + 15%	-0.400 V
Ni	2+	1:2	4	341 + 15%	-0.375 V

The SEM analysis (**Figure 18**) of the samples showed the deposition of particles in the nanometer size range for palladium, platinum, and rhodium. Notably, obtaining metal nanoparticles via electrodeposition on silicon is significant for several reasons, such as enhancing catalytic properties, electrical conductivity, and magnetic properties, while leveraging all the advantages of electrochemical deposition (e.g., tunable properties of the deposit, scalability, and low-cost fabrication). However, in the case of charge-controlled deposition of nickel and ruthenium, no detectable presence of these metals was detected. Although no Ni and Ru deposits electrodeposited on n-silicon were obtained under the conditions used, such results are reported in the literature and were obtained using different working conditions than those used for this article. These conditions were not ideal for the implementation with the experimental setup used in this work[133] or were not suitable for obtaining deposits with the characteristics sought[134].

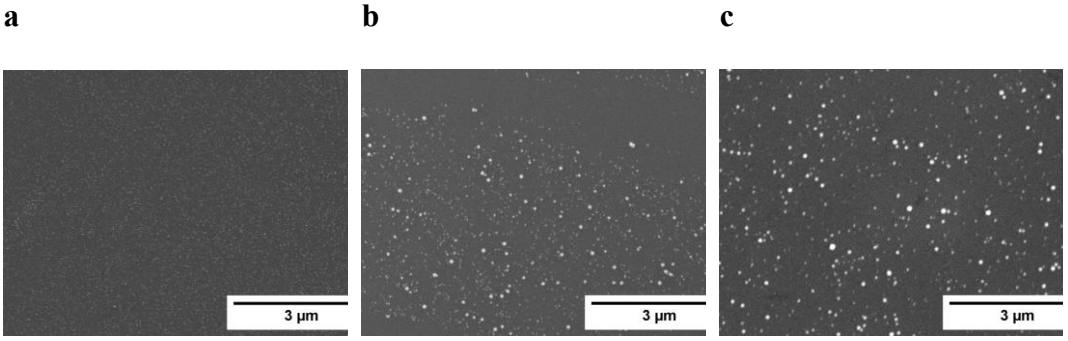

Figure 18 SE-SEM images of the deposit obtained through charge-controlled deposition on the Si working electrode in H_2SO_4 0.1 M, 1 mM metal solution (**a**) 1 mM $[Pd(NH_3)_4]SO_4$ solution; (**b**) 1 mM K_2PtCl_4 solution; (**c**) 1 mM $RhCl_3$ solution.

XPS analyses were performed on the samples to confirm the presence of the metals and their oxidation state (**Figure 19**). The presence of the peaks related to the photoelectronic emission of Pd, Rh, and Pt was confirmed by studying the corresponding emission lines. In Figure 5a, the doublet constituting the 3D emission of palladium is analyzed. The fitting of the doublet was performed as per the literature, considering a Shirley-type background, an LA ($\alpha = 1.9$, $\beta = 7$, $m = 2$) curve shape[119,135], a ratio of the d3/2 and d5/2 peak areas of 0.667, the same full width at half maximum (FWHM) for the 2 peaks, and the relative binding energies of the 2 peaks of 5.26 eV. A value of 335.4 eV was obtained from the peak analysis, which, according to the literature, is within the expected value for metallic palladium (335.4 eV)[135].

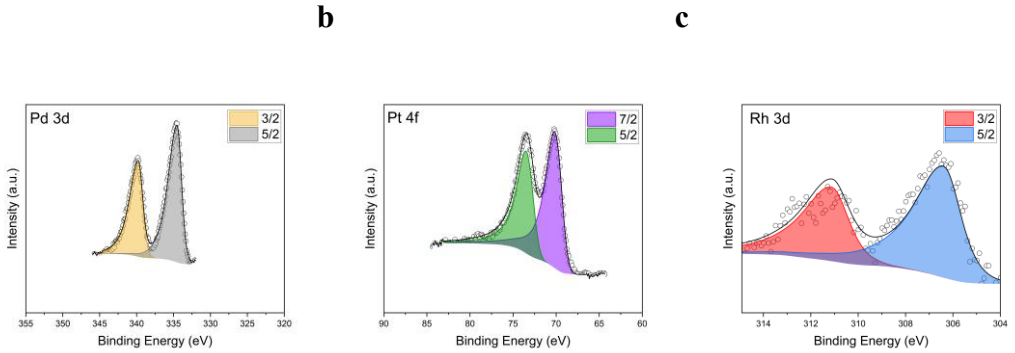

Figure 19 XPS analysis performed on the silicon electrodes used after charge-controlled deposition on the Si working electrode in H_2SO_4 0.1 M, and 1 mM metal solution: (**a**) 1 mM $[Pd(NH_3)_4]SO_4$ solution; (**b**) 1 mM K_2PtCl_4 solution; (**c**) 1 mM $RhCl_3$ solution.

In **Figure 19b**, the doublet constituting the 3f emission of platinum is analyzed. The doublet was fitted as per the literature[136], considering a Shirley-type background, an LA(1.2, 85, 70) curve shape, a ratio between the f5/2 and 7/2 peak areas of 0.75, the same FWHM for the 2 peaks, and the relative binding energies of the 2 peaks (3.33 eV). A value of 71.0 eV was obtained from the analysis of the peak, which, according to the literature, is within the expected value for metallic platinum (71.1 eV)[136]. In Figure 5c, the doublet constituting the 3D emission of rhodium is analyzed. The doublet was fitted as per the literature[137], considering a Shirley-type background, an LA(1.2, 3, 2) curve shape, a ratio between the d3/2 and d5/2 peak areas of 0.667, the same FWHM for the 2 peaks, and the relative binding energies of the 2 peaks (4.74 eV). A value of 307.2 eV was obtained from the peak analysis, close to the value of binding energy present in the literature for rhodium metal (307.0 eV)[137]. XPS analysis showed no metal presence in the case of nickel and ruthenium charge controlled deposition, confirming the EDS-SEM analyses results.

Multi-Cycle Charge-Controlled Deposition

Multi-cycle charge-controlled depositions were performed to evaluate the possibility of obtaining a deposit whose morphology can be modulated as deposition cycles change, varying between a thin film and a nanostructured deposit. The metal selected for these tests was rhodium. This metal was found to be the most promising for these experiments, as it exhibits a cathodic peak attributable to the deposition of the metal within the selected potential range and does not exhibit deposition phenomena occurring in an electroless mode. To the best of our knowledge, there are limited articles in the literature dealing with the rhodium deposition on silicon. To observe the variation in deposit morphology as the number of deposition cycles changes, five charge-controlled deposition sessions were carried out at 1 cycle, 10 cycles, 20 cycles, 30 cycles, 40 cycles, and 50 cycles. One cycle corresponds to 256 + 15% μC. In **Figure 20**, it is possible to observe an increasing coverage of rhodium on the silicon surface; however, even at 50 cycles, there is not total coverage of the surface, and a complete film is not observed. Instead, a nanostructured porous deposit of rhodium was observed.

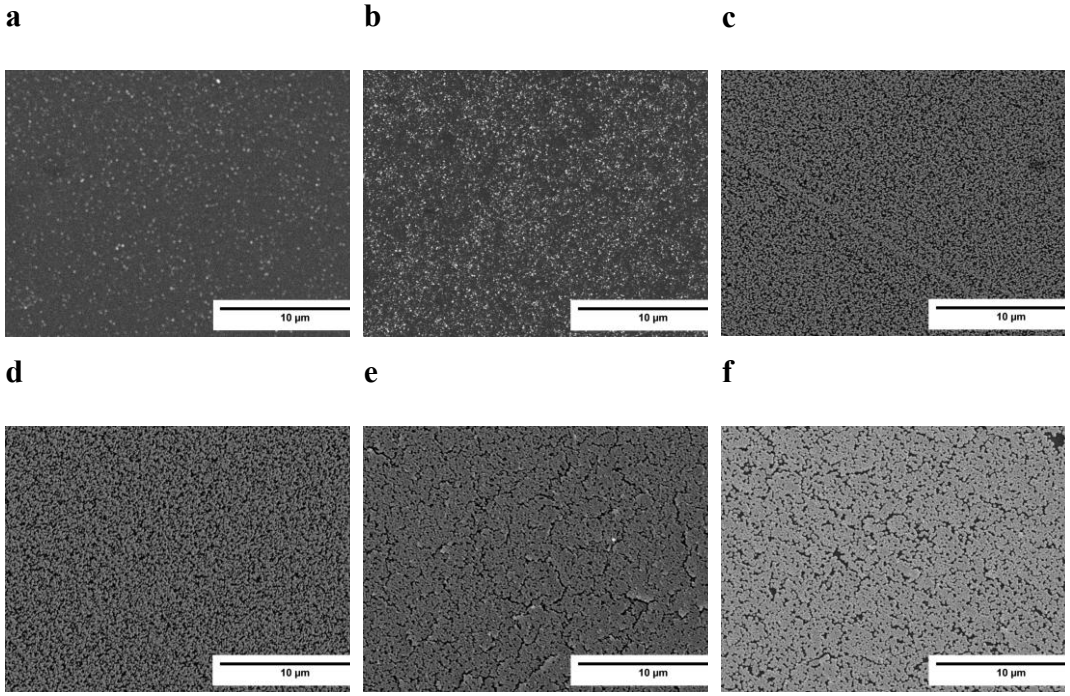

Figure 20 SEM images of the deposits obtained through a variable number of charge-controlled deposition cycles on the Si working electrode in H_2SO_4 0.1 M and $RhCl_3$ 1 mM solution: (**a**) 1 cycle; (**b**) 10 cycles; (**c**) 20 cycles; (**d**) 30 cycles; (**e**) 40 cycles; and (**f**) 50 cycles.

Quantification of silicon surface coverage was performed using the ImageJ (Version

1.54d) program by analyzing SEM images related to controlled rhodium deposition at 1 cycle, 10 cycles, 20 cycles, 30 cycles, 40 cycles, and 50 cycles. **Figure 21a** shows the overall increasing trend of the surface coverage as the number of deposition cycles rises. For a charge-controlled deposition at 50 cycles, a surface coverage of almost 85 percent is obtained.

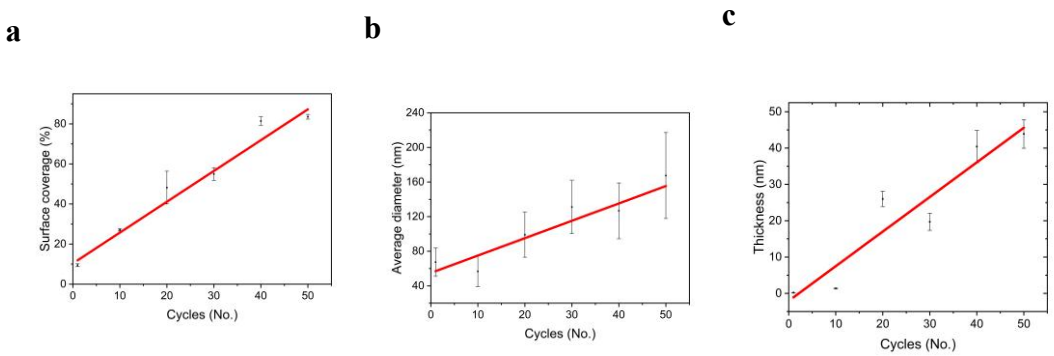

Figure 21 (**a**) Surface coverage trend; (**b**) average particle diameter size trend; (**c**) equivalent thickness trend of the deposits, obtained through a variable number of charge-controlled deposition cycles (1, 10, 20, 30, 40, and 50 cycles) on the Si working electrode using H_2SO_4 0.1 M and $RhCl_3$ 1 mM solutions. The reported errors are calculated based on three independent measurements.

Rhodium particle size distribution analyses were also performed using the ImageJ program. **Figure 21b** the average particle diameter is shown, and an overall increasing trend is visible. The results show an average diameter of about 67 nm for one-cycle deposition and up to about 168 nm for 50-cycle deposition, confirming the achievement of a nanostructured deposit. EDS measurements were carried out using the Layer Probe program of AZteclive. These measurements were aimed at investigating the average equivalent thickness of the metallic rhodium deposit on the silicon surface. In addition, to improve the fitting of the EDS spectrum, an additional layer containing carbon and oxygen in varying amounts was included within the theoretical layered model; this allows for oxides and carbon residues found on the surface to be considered. The EDS spectra of the sample and the measured thickness values after 1, 10, 20, 30, 40, and 50 cycles were recorded. The analysis yielded the average metal deposit thickness for each cycle. These thickness values were then plotted as a function of the number of cycles, as shown in **Figure 21c**. The observed trend aligns with previous results regarding surface coverage and the average particle diameter. The data demonstrate that an average thickness of less than a few hundred nanometers was achieved. Consequently, it can be confirmed that a nanostructured deposition was successfully obtained[138].

4.4 Conclusions

In this work, the controlled electrochemical deposition of metals on silicon surfaces was evaluated, exploring the potential for underpotential deposition (UPD), thin and ultra-thin films, and nanostructured deposits. Mn, Co, Ni, Ru, Pd, Rh, and Pt were selected based on their high affinity for silicon, as predicted by DFT calculations. Electrochemical characterization revealed cathodic peaks for Ni, Pd, Ru, Rh, and Pt, with further SEM-EDS and XPS analyses confirming metallic deposits only for Pd, Rh, and Pt, forming nanosized particles. Despite the theoretically high affinity of the chosen metals with silicon, UPD phenomena were not observed for any of the studied metals under the experimental conditions. The study of rhodium electrodeposition was deepened: multi-cycle charge-controlled deposition on n-doped silicon demonstrated tunable surface coverage and particle size, starting from an average diameter of 67 nm for 1 cycle and reaching 168 nm after 50 deposition cycles, with a surface coverage of 84%. The equivalent deposit thickness, estimated in tens of nanometers, correlated with surface coverage and particle size, confirming the formation of nanostructured rhodium. These results highlight the potential of rhodium electrodeposition on silicon to develop materials with tailored structural, electrical, and catalytic properties. Future work should focus on optimizing deposition processes and assessing the long-term stability and adhesion of these nanostructures to expand their applicability in catalysis, electronics, and sensing.

5 Electrodeposited Metal Catalysts for Controlled Fabrication of Silicon Nanowires via metal assisted chemical etching (MACE)

The third phase of this doctoral work built upon the knowledge gained from the electrodeposition of metallic nanostructures on silicon. The research was extended to the fabrication of silicon nanowires (NWs) through the metal-assisted chemical etching (MACE) process, employing electrodeposited metals as catalytic templates. The objective was to develop a controlled and scalable method for producing silicon nanowires with tunable morphology, suitable for applications in energy conversion, sensing, and nanotechnology.

5.1 Introduction

The electrochemical deposition of metallic films, patterns, and nanostructures onto silicon substrates enables the integration of the advantageous characteristics of metals with the remarkable electronic properties of silicon. This approach offers valuable applications in various field, including integrated circuits, battery electrodes, supercapacitors, fuel cells, sensors, water-splitting systems, and photovoltaic devices [82,83]. Silicon is one of the most abundant elements on the Earth's crust. Its semi-conductive nature makes it suitable for many applications such as the energy, sensing and electronic fields [3,139]. Highly ordered crystalline substrates are already available at relatively low cost, thanks also to the large production for the electronics sector, hence monocrystalline silicon wafer represents an optimal substrate.

Among the most commonly used techniques for depositing metals on silicon at the state of the art are physical and vapor deposition methods, e.g., Chemical Vapor Deposition (CVD), Atomic Layer Deposition (ALD), Physical Vapor Deposition (PVD) [84,140,141]. Among physical deposition methods are PVD, including vacuum evaporation, Molecular Beam Epitaxy (MBE), sputtering, and Pulsed Laser Deposition (PLD) [85–87]. Other physical techniques for coating include spin coating and spray coating [89,90].

The electrodeposition of metal patterns and nanoparticles onto semiconductor surfaces provides several benefits and holds significant technological value, particularly in creating metal/semiconductor contacts. This deposition method is extremely versatile, cost-effective, scalable, and requires minimal deposition time. It operates at room temperature and atmospheric pressure, using an aqueous solution, and allows for the modulation of the deposited material's properties while maintaining low operating costs [142,143].

It should be noted that silicon is a substrate with some critical issues: chemically inactive surface due to passivation, bad nucleation and growth, and difficulties in electrochemical characterization.

The field of electrodeposition of metals on silicon continues to hold significant potential for advancements in semiconductor-metal contact technology [100], and it is

of notable technological importance due to its role in forming the Schottky barrier [98]. This barrier permits current flow in one direction while blocking it in the opposite direction, making it essential for various electronic applications.
When a semiconductor interacts with an electrolyte during the deposition process, the resultant barrier is called the Mott-Schottky junction [99]. When a silicon electrode is immersed in the solution and the equilibrium is reached, a depletion or accumulation layer of the charge carriers is formed depending on the doping. In this condition, a Schottky diode is formed. For this reason, p-type doping promotes anodic currents and blocks cathodic ones while n-type doping vice versa. This is true in dark conditions, while in the light the photonic pumping occurs. The Schottky barriers can be even bigger after the deposition depending on the nature of the metal. A positive barrier height for an n-type semiconductor means the current tends to flow more easily into the semiconductor.
No Under Potential Deposition (UPD) or Surface-Limited Reactions (SLRs) were found on silicon and deposition of continuous ultrathin films (<50 nm) is very difficult [144,145] due to the semiconductor's band structure, which influences both the thermodynamics and the kinetics of the metal deposition process [101,146]. Most studies in the field focus on the deposition of thicker and more clustered films. A notable example of an ultrathin film is presented by Allongue, who successfully produced a continuous epitaxial gold film of just 4 nm, constrained by the mass transport limit [102]. However, to date, there is a lack of studies reporting on the occurrence of SLR in this context.
In this paper, the possibility of obtaining Silicon Nanowires (NWs) through Metal-assisted Chemical Etching (MACE) technique was evaluated.
Similarly to what has been said about obtaining metal deposits on silicon, among the most widely used methods in the literature to obtain deposits suitable for MACE are physical deposition methods, electroless deposition and galvanic displacement [147–149]. The possibility of obtaining nanowires using electrodeposition to obtain MACE shows an interesting innovation, allowing all the previously mentioned advantages of electrodeposition to be exploited.
The etching step was performed using a solution containing hydrogen peroxide (oxidizing agent) and hydrofluoric acid (dissolving agent) as reported in the literature.
It is known that MACE begins with the catalytic reduction of the oxidant at the Si/metal interface, generating holes (h^+). These holes are then injected into the silicon substrate beneath the metal catalyst, where they weaken Si-Si bonds. The silicon is then oxidized in the contact area with the metal and subsequently dissolved by hydrofluoric acid. Metal nanoparticles gradually sink into silicon, forming pores, and the etching occurs as a localized electrochemical process [150].
Figure 22 shows the diagram of the MACE mechanism and the operational steps.

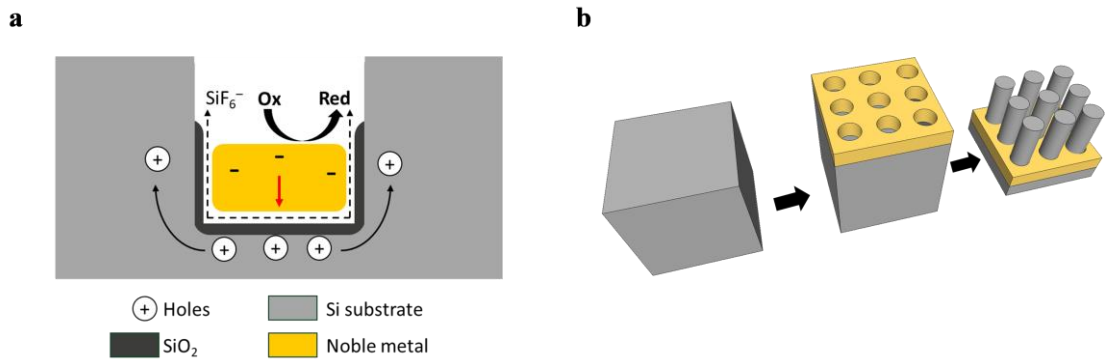

Figure 22 (**a**) Metal Assisted Chemical Etching (MACE) mechanism diagram; (**b**) MACE operational steps, first the metal deposition and then the chemical etching. The metal can be removed in a further step.

Anodic (silicon) and cathodic (metal) sites are formed on the etched surface with local currents flowing between them during etching. This current is due to holes injected into the silicon valence band by the metal particle. Since holes are provided by the reaction of the oxidant with the metal particle, etching depends on the rate at which the oxidant can generate holes under the metal particles. Etching proceeds slowly on the uncovered silicon surface because the oxidizing agent preferentially captures electrons from metal particles due to their strong catalytic activity for the cathodic reaction, so the role of the metal is to locally increase the hole injection, accelerating the dissolution of silicon [149].
During the etching, at the metal-silicon interface, the formation of silicon oxide is promoted, this layer is continuously removed by fluoride ions and the metal particle travels down in the silicon shaping the holes. After the MACE the metal can be dissolved and even recycled, minimizing the cost of the overall process.
The ratio of HF to H_2O_2, denoted as $\mu = HF/(HF + H_2O_2)$, plays a crucial role in determining the morphology and etching depth of silicon nanostructures. Extreme ratios ($\mu = 0$ or 1), where either HF or H_2O_2 is absent, result in negligible etching. When only H_2O_2 is present ($\mu = 0$), the high concentration rapidly dissolves the metal nanoparticles that catalyze the etching process. In the absence of H_2O_2 ($\mu = 1$), the oxidation rate of silicon is very low, leading to very slow etching.
Intermediate ratios of HF to H_2O_2 lead to varying degrees of etching and different morphologies. Another important factor is the silicon doping type and level [151]. For low-conductivity silicon (LC-Si), large aspect ratio features were obtained for most ratios, with the maximum etch depth observed at $\mu = 0.71$ [152]. For high-conductivity silicon (HC-Si), high concentrations of H_2O_2 ($\mu \leq 0.7$) resulted in the formation of large trenches rather than nanowires. This is because the excess H_2O_2 dissolves a significant amount of metal, which then redeposits at various sites on the silicon surface, causing and lateral etching. Well-defined Si-NWs with good surface

morphology were obtained on HC-Si for μ = 0.90 and 0.95. These ratios had relatively low H_2O_2 concentrations, minimizing metal dissolution and redeposition and leading to more controlled etching [152].

Although some studies suggest that the etching direction is mainly determined by the molar ratio of HF to H_2O_2 (ε = [HF]/[H_2O_2]) irrespective of the crystal orientation of the starting silicon wafer, a study found no correlation between the etching direction and the concentration ratio of HF to H_2O_2. However, ε appears to affect the morphology of the resulting SiNWs. At $\varepsilon \geq 1.15$, the result is solid non-porous SiNWs, while at $0.3 < \varepsilon < 1.15$, SiNWs tend to be porous [153].

The etching rate is determined by two competing events: the injection of holes into the bulk silicon through the metal-silicon quasi-Schottky interface, and the removal of oxidized silicon by HF from just underneath the catalyst metal.

The number of holes injected into silicon is proportional to the H_2O_2 concentration or its decomposition activity. The removal of oxidized silicon by HF is associated with the cleavage of its back bonds, which increases in different crystal planes with the order ⟨100⟩ < ⟨110⟩ < ⟨111⟩.

The etching direction is mainly dictated by the etching rate. At low etching rates, etching occurs along vertical ⟨100⟩ directions, while at high etching rates, etching occurs along slanted ⟨110⟩ directions [153].

When etching solutions have a high HF concentration, catalytic decomposition of H_2O_2 would become the rate-determining process. This means the etching rate is proportional to the number of holes injected into silicon.

At low H_2O_2 concentrations, the injection of holes into silicon atoms will be localized at the ⟨100⟩ plane, resulting in etching along the ⟨100⟩ direction. As the concentration of H_2O_2 increases, and thereby the number of holes exceeds a certain threshold, the removal of silicon atoms would occur rapidly in the crystal plane, where there are more silicon bonds to polarize, resulting in ⟨110⟩ and even possibly ⟨111⟩ etchings. For solutions with a high H_2O_2 concentration, the removal of oxidized silicon by HF governs the overall etching reaction and etching direction.

At low HF concentrations, the removal of oxidized silicon will occur slowly in the ⟨100⟩ plane, resulting in porous SiNWs. At high HF concentrations, removal of oxidized silicon would be kinetically favored in the crystal planes with a higher density of silicon back bonds, resulting in etchings along non-⟨100⟩ directions. Both high H_2O_2 concentration and low HF concentration are necessary if porous nanowire formation is desired [153].

For the reasons listed above, and after some preliminary testing, it was chosen to employ a 5 M HF and 0.44 M H_2O_2 etching solution, with μ = 0.92 and ε = 11.36. In these conditions, etching is likely to proceed preferentially along the ⟨100⟩ direction, yielding vertically aligned solid, non-porous SiNWs, showing a moderately high etching rate, limited by the relatively low H_2O_2 concentration.

Among all metals, the most used for MACE are silver and gold, Ag is cheaper while Au has higher catalytic activity, for this reason in this study it was chosen to proceed

with gold. Electrodeposition of gold is widely discussed in the literature [154] and commonly uses gold salts containing cyanides, which are proven to be stable even in acid solutions thanks to the very high stability constants of the complexes: $Au(CN)_2^-$, $\beta 2 \approx 10^{38}$ [155]; $Au(CN)_4^-$, $\beta 4 \approx 10^{56}$ [156]. On the other hand, electrodeposition of thin films or gold nanoparticles on silicon is not a common practice [102]. As reported in the literature, gold plating electrolytes can be formulated using Au(I) or Au(III) salts.

Au(I) formulations are more efficient in terms of electricity consumption. For the same level of efficiency, a given amount of current will deposit a greater amount of gold from a monovalent gold complex compared to a trivalent gold complex. On the other hand, deposits obtained from acid Au(I) baths have low ductility and cannot be deformed without the risk of cracking in the surface coating.

The most common Au(I) baths are based on the cyanide complex $KAu(CN)_2$. These baths can operate under alkaline, neutral, or acidic conditions. However, deposits with the most desirable properties for contact applications are obtained from acidic baths (pH 3.5–5.0). Under acidic conditions, the low concentration of free cyanide ions promotes the formation of HCN. This increases the concentration of available Au^+ ions for deposition, making the plating process more efficient.

However, at pH levels below 3, the $Au(CN)_2^-$ complex tends to decompose with the precipitation of AuCN, limiting the usable pH range.

Au (III) formulations can be used to plate acid-resistant substrates, such as stainless steel. Au(III) deposits can be bright, hard, as well as ductile and relatively pore-free. The deposition rate from Au(III) is slow, and the solutions are also corrosive due to the low pH. Au(III) baths typically use the cyanide complex $KAu(CN)_4$. These baths exhibit excellent plating characteristics at pH values ranging from 0.1 to 5.0, with optimal performance in the pH range of 1.0 to 3.0 [154]. This lower pH is often necessary to plate acid-resistant substrates and to increase the adhesion of the coating. In Au(III) baths, lower pH levels can enhance deposition rate and improve deposit hardness.

The cyanide complex of this metal was used to avoid uncontrolled electroless deposition, employing a typical acid electrodeposition formulation.

Different deposition parameters, such as the oxidation state of the gold salt, pH level, applied potential, and deposition duration, were examined to identify the ideal conditions for fabricating thin and uniform NWs through MACE. The deposited materials and NWs were extensively analyzed using a scanning electron microscope (SEM).

The identified procedure could open up new possibilities for compact, high-performance sensors and electrodes with a large specific surface area, especially when the nanowires are adorned with metals or other chemical substances.

5.2 Materials and methods

Reagents

All solutions were prepared using ultrapure water with a conductivity of less than 0.059 μS/cm. All reagents were of analytical grade and were used as received without further purification. The RCA (Radio Corporation of America) method [3] was employed to activate the silicon electrode using the following reagents: sulfuric acid (H_2SO_4, 98%) sourced from chemPUR, Karlsruhe, Germany; hydrochloric acid (HCl, 37% w/w) and hydrofluoric acid (HF, 48% w/w) obtained from VWR International, Fontenay-sous-Bois, France; and acetone (AcOH), ethanol (EtOH), and hydrogen peroxide (H_2O_2, 30% w/w) provided by Carlo Erba, Val de Reuil, France.

The following salts were used for the electrolytic solutions: potassium dicyanoaurate (I) ($KAu(CN)_2$), potassium dihydrogen citrate ($KH_2C_6H_5O_7$) Merk KGA, Darmstadt, Germany and potassium tetracyanoaurate (III) ($KAu(CN)_4$) Valmet Spa, Calenzano, Italy.

Experimental set-up

The electrochemical characterization and deposition system employed in this study is a fully automated setup designed to regulate solution input and residence time within the cell using a solenoid valve system. The solutions, stored in Pyrex glass containers, are deaerated with nitrogen gas and remotely introduced into a Kel-F (polychlorotrifluoroethylene) electrochemical cell. The flow rate of the solution in the cell is about 2 mL/s, and the cell contains 2 mL of solution. To prevent photonic pumping effects on silicon, the electrochemical cell was consistently kept in dark conditions throughout the electrodeposition process. The setup was designed to ensure reproducible depositions while minimizing silicon surface oxidation. For the electrochemical measurements, an AMEL Model 551 potentiostat was utilized, interfaced with a personal computer equipped with a National Instruments data acquisition card. A three-electrode configuration was employed, consisting of a monocrystalline (100) n-Si working electrode (0.1–1 Ω·cm) with an exposed surface area of 0.785 cm^2, a gold counter electrode, and an Ag/AgCl (saturated KCl) reference electrode. Cyclic voltammetry measurements were conducted at a scan rate of 10 mV/s. Prior to the measurements, the silicon electrodes underwent cleaning and activation following the RCA procedure, as described in 4.2 Materials and Methods, and in previous works [3,145].

The silicon etching process was conducted in plastic beakers resistant to hydrofluoric acid using a 5 M HF and 0.44 M H_2O_2 etching solution.

The two gold electroplating solutions contain, unless otherwise stated: i) 1 mM $KAu(CN)_4$ and 0.1 M H_2SO_4, pH 1; ii) 1 mM $KAu(CN)_2$, 170 g/L potassium dihydrogen citrate, and 35 g/L dipotassium hydrogen citrate, pH 4.

SEM analysis was performed using a Hitachi SU3800 (Hitachi High-Tech Corporation, Tokyo, Japan), equipped with an Ultim Max 40 Analytical Silicon Drift

EDS Detector (Oxford Instruments plc, Abingdon, UK). Energy-dispersive spectroscopy (EDS) measurements were conducted using the Layer Probe feature of AZteclive (Version 5.0) to determine the average equivalent thickness of the metallic deposit.

The surface coverage and particle size distribution were evaluated using ImageJ software (Version 1.54d) by analyzing SEM images acquired at 10 kV and 10,000× magnification. The etch depth was determined from SEM cross-sectional images by taking measurements at multiple points across the sample and calculating the average value.

5.3 Results and discussion

Cyclic Voltammetry (CV) was performed, using solutions containing the gold salt, to investigate the presence of any faradic processes associated with reduction reactions that could be attributable to the electrodeposition of the metal. The measurements were carried out by performing cyclovoltammetries with the blank solution (0.1 M H_2SO_4) and using a solution containing 0.1 mM $KAu(CN)_4$, and 0.1M H_2SO_4. In both cases, no distinct cathodic peak attributable to Au deposition is observed, as the cathodic current is dominated by hydrogen evolution at negative potentials as is observable in **Figure 23**. This behavior does not indicate the absence of gold reduction, but rather that the reduction process occurs concurrently with hydrogen evolution.

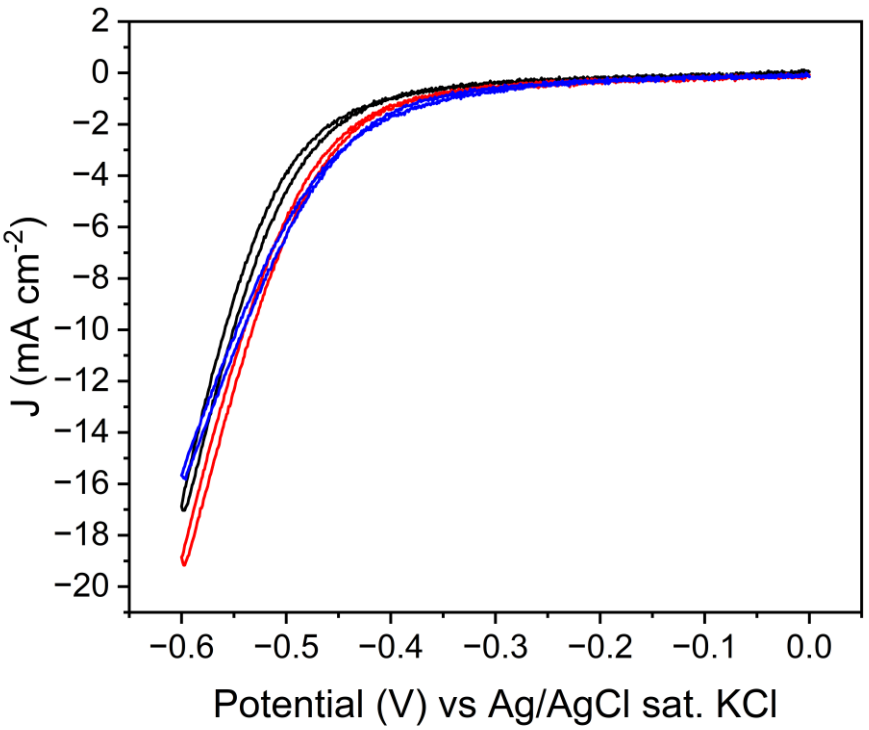

Figure 23 CVs performed in the potential range of 0.0 V to -0.6 V vs. Ag/AgCl sat. KCl, 10 mV/s scan rate. In black the scan related to the solution containing 0.1 M H_2SO_4; in red 0.1 M H_2SO_4 + 0.1 mM $KAu(CN)_4$ solution; in blue 0.1 M H_2SO_4 performed after the CV scan executed with the solution containing the gold salt.

A preliminary sample was prepared, performing the electrodeposition of gold at -1.5 V using the solution containing 0.1 mM $KAu(CN)_4$ and 0.1 M H_2SO_4. Before

deposition, the 0.1 M H_2SO_4 solution was flushed into the cell. The electrolyte containing gold flowed through the cell for 3 seconds, after which a potential was applied to the electrochemical cell for 5 seconds. Subsequently, the solution was flowed again for 3 seconds. This process was repeated for 10 cycles, resulting in a total deposition time of 80 s. At the end of the cycling procedure, the electrode was rinsed in the cell using an H_2SO_4 0.1 M solution before being removed. The sample was then washed with ultrapure water and dried with a nitrogen flow. Then etching was performed on the obtained sample for 30 minutes.
The result of the sample obtained at -1.5 V deposition potential can be observed in **Figure 24**.

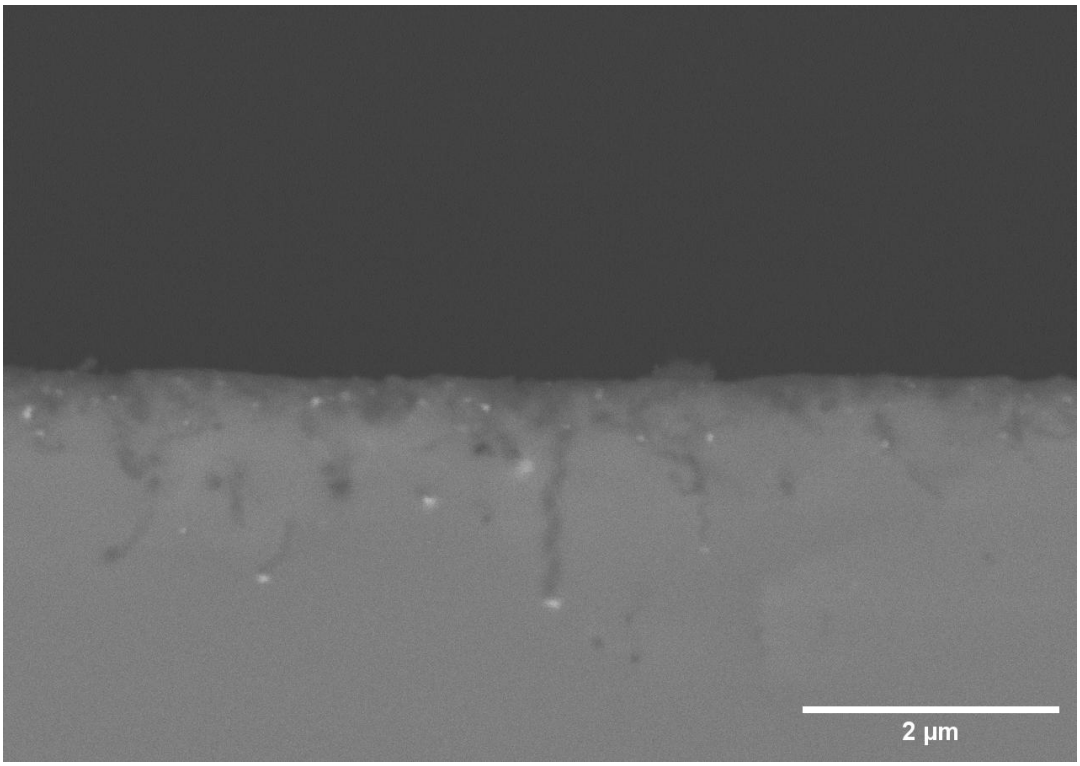

Figure 24 BSE-SEM cross-section image relative to the sample obtained at -1.5 V for 10 cycles of deposition after etching.

As can be seen, the nanostructured deposit of gold on silicon was obtained; however, the etching did not result in nanowires, although there were areas where the etching process occurred.
Given the unsatisfactory results obtained, it was decided to develop a new procedure of electrodeposition, using a 1 mM gold salt solution. Several parameters besides the concentration of gold in the solution were then tested: deposition durations (50 s and 100 s total time of applied potential), and potentials (-1.0 V, -1.5 V and -2.0 V). Again, no satisfactory results were obtained, but it was observed that the most

promising results were achieved in cases where a larger amount of gold had been deposited.
After these preliminary results, several deposition tests were carried out, using two different formulations with gold salts at oxidation numbers I and III, respectively. Two different gold salts were tested to observe the effect of lower and higher formulation pH, as well as the effects of different gold oxidation states on the results. For each formulation, three different potentials (-1.0, -1.5 V, and -2.0 V) and two different deposition times (5 and 10 minutes) were used, so that an overall picture of the influence of the three variables on the characteristics of the final deposit was obtained, for a total of twelve samples. A set of six samples, prepared under varying deposition potentials and durations, was characterized to determine the most suitable surface for chemical etching.
Prior to deposition, the solution containing 0.1 M H_2SO_4 alone was flushed into the cell as a wash, also ensuring that there was no loss of solution in the system. During the deposition, the potential is kept fixed and the solution containing the gold salt was fluxed inside the electrochemical cell for 1 second at the beginning of each minute. In **Figure 25**, are reported the current transients recorded during the deposition.

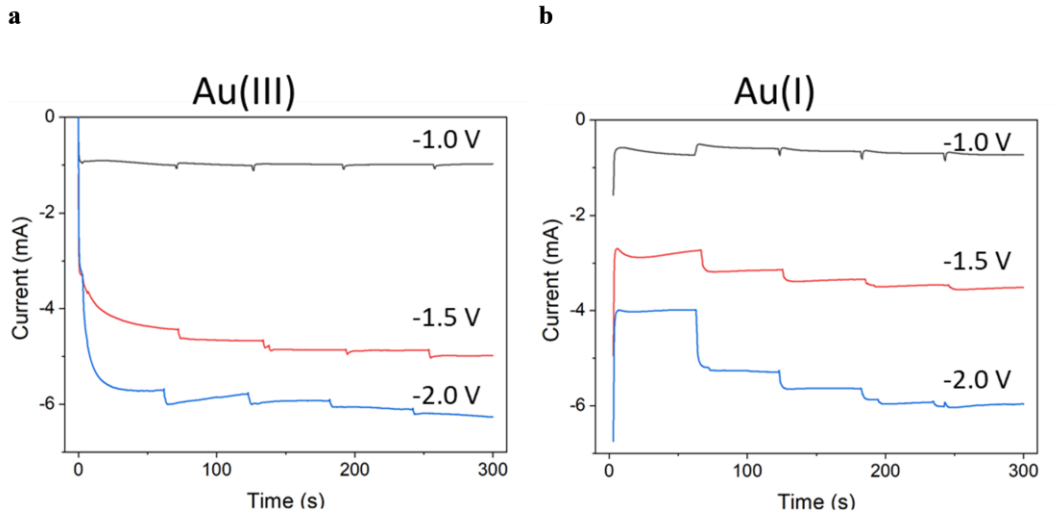

Figure 25 Chronoamperogram of solution containing (**a**) 1 mM $KAu(CN)_4$, 0.1 M H_2SO_4; (**b**) 1 mM $KAu(CN)_2$, 170 g/L $C_6H_7KO_7$, and 35 g/L $C_6H_6K_2O_7$. Obtained at -1.0 V, -1.5 V and 2.0 V vs Ag/AgCl sat. KCl reference electrode for 5 min.

At the end of this procedure, the electrode was washed back into the cell with 0.1 M H_2SO_4 solution before being extracted, and then the sample was washed with

ultrapure water and dried using a flow of nitrogen and analyzed with SEM. Then the etching procedure was conducted on each sample for 15 minutes.
The results of the 5-minute deposition using the Au(III) solution, before and after the etching, can be observed in **Figure 26**.

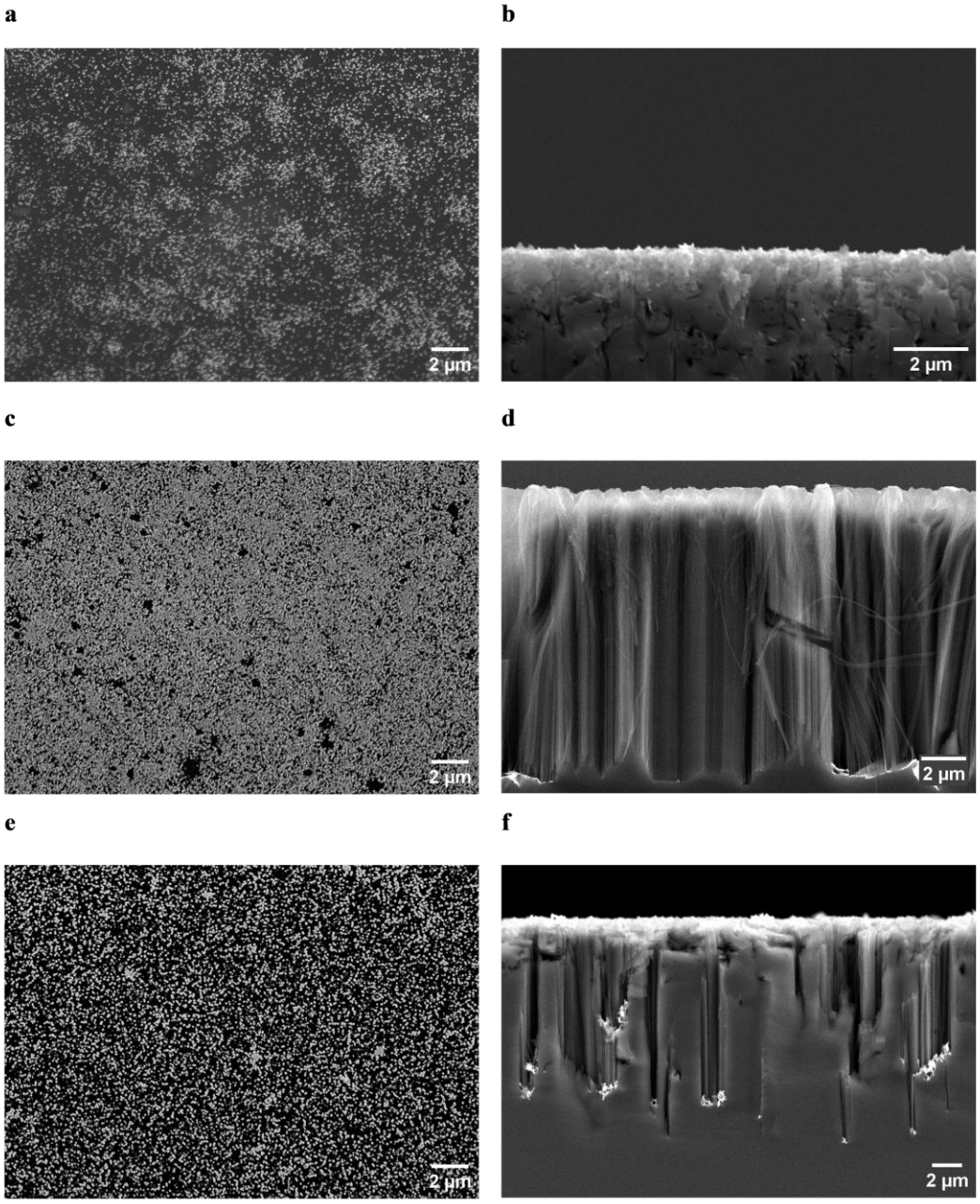

Figure 26 On the left (**a, c,** and **e**), BSE-SEM top-view of the gold deposit on the silicon working electrode obtained using the Au(III) solution; on the right (**b, d,** and **f**) BSE-SEM cross-sections of the of the same samples after the etching process. Deposit obtained at (**a,b**) -1.0 V; (**c,d**) -1.5 V; (**e,f**) -2.0 V vs Ag/AgCl sat. KCl reference electrode for 5 min of deposition and 15 min of etching time.

The same experiments were repeated by performing 10-minute electrodepositions (**Figure 27**).

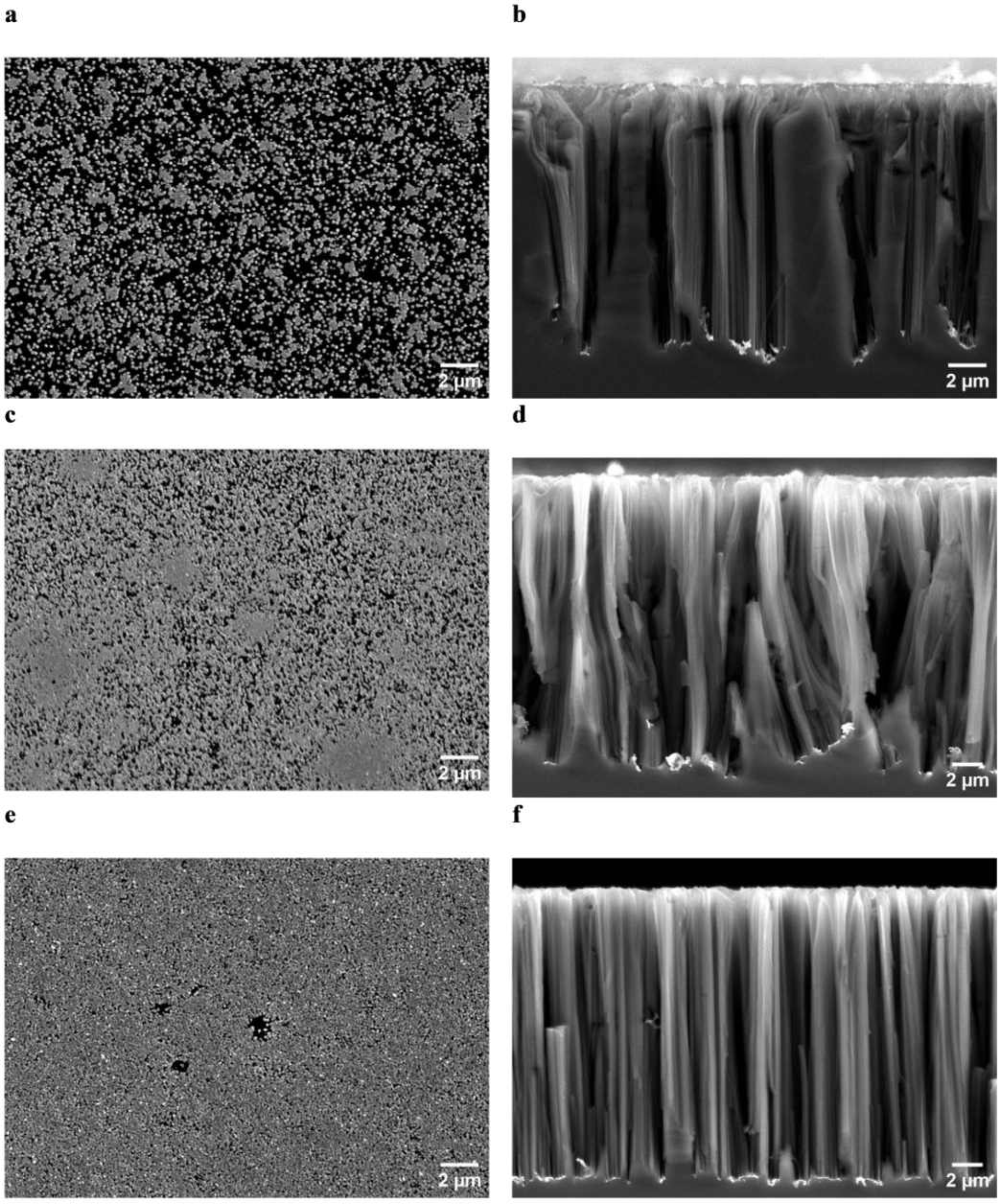

Figure 27 On the left (**a, c,** and **e**), BSE-SEM top-view of the gold deposit on the silicon working electrode obtained using the Au(III) solution; on the right (b, d, and f) BSE-SEM cross-sections of the of the same samples after the etching process. Deposit obtained at (**a,b**) -1.0 V; (**c,d**) -1.5 V; (**e,f**) -2.0 V vs Ag/AgCl sat. KCl reference electrode for 10 min of deposition and 15 min of etching time.

The same experiments were repeated using the Au(I) solution. The results of the 5-minute deposition are shown in **Figure 28**.

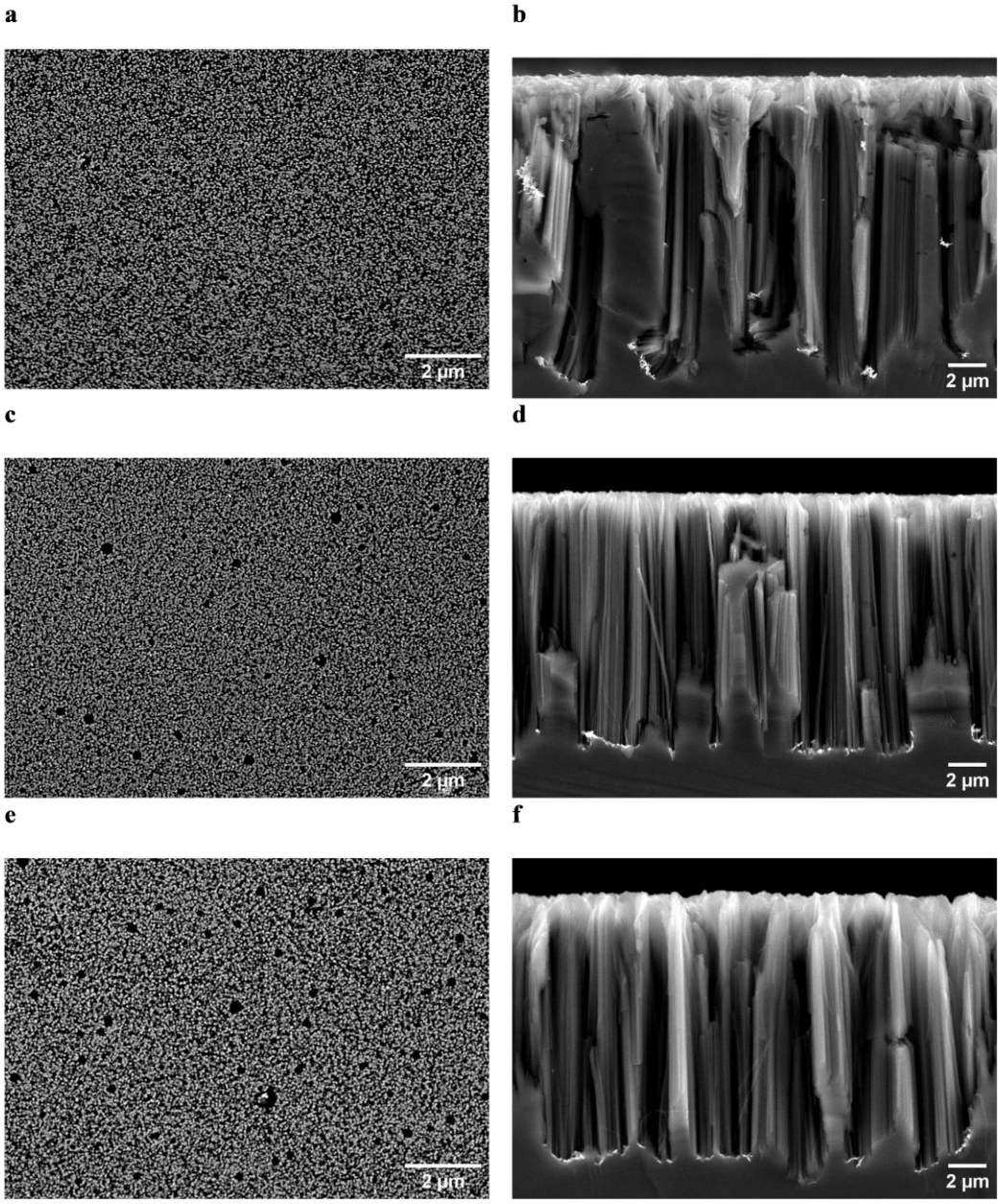

Figure 28 On the left (**a, c** and **e**), BSE-SEM top-view of the gold deposit on the silicon working electrode obtained using the Au(I) solution; on the right (**b, d**, and **f**) BSESEM cross-sections of the of the same samples after the etching process. Deposit obtained at (**a,b**) -1.0 V; (**c,d**) -1.5 V; **(e,f)** -2.0 V vs Ag/AgCl sat. KCl reference electrode for 5 min of deposition and 15 min of etching time.

The results of the 10-minute deposition using the Au(I) solution are shown in **Figure 29**.

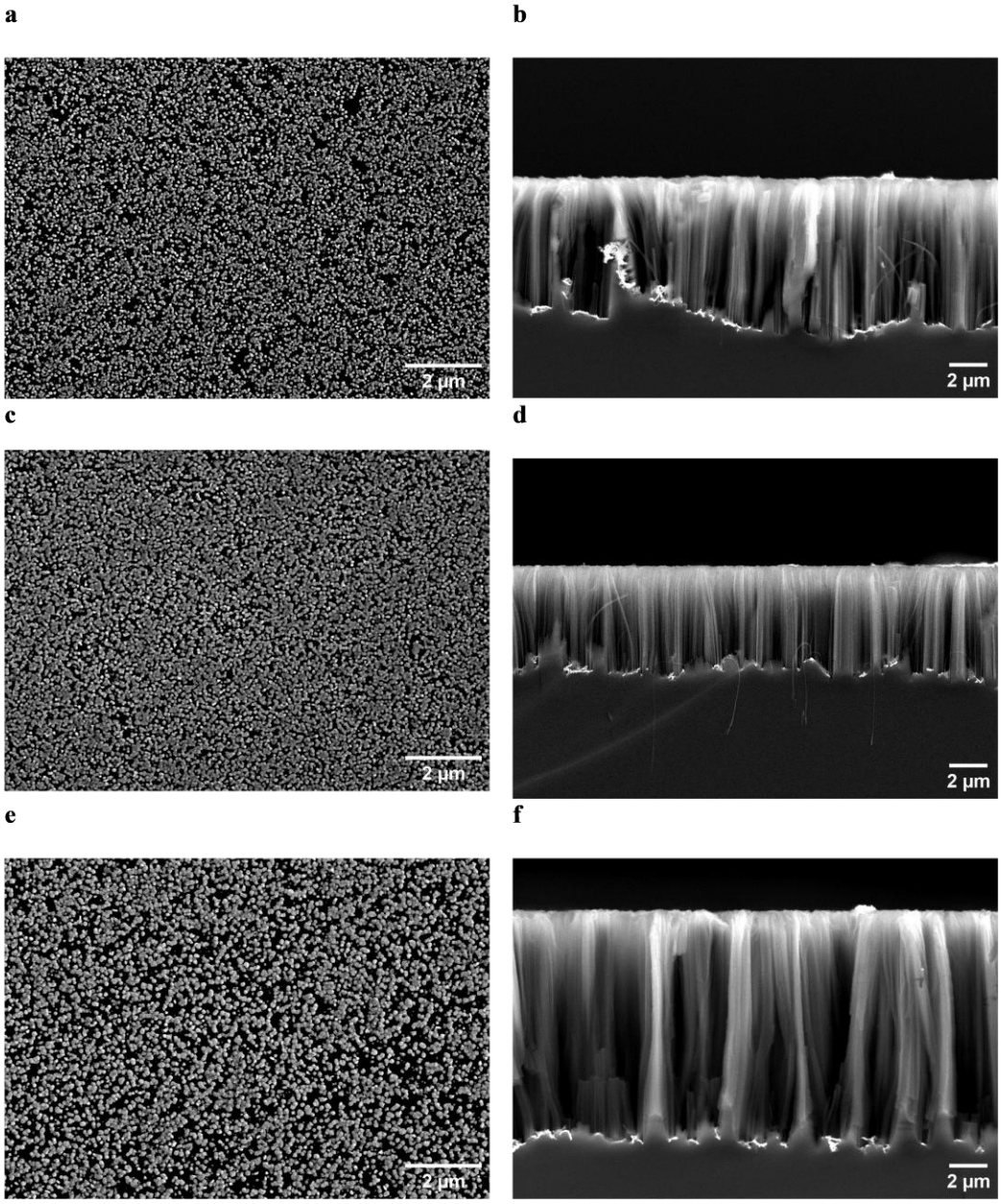

Figure 29 On the left (**a, c** and **e**), BSE-SEM top-view of the gold deposit on the silicon working electrode obtained using the Au(I) solution; on the right (**b, d**, and **f**) BSE-SEM cross-sections of the of the same samples after the etching process. Deposit obtained at (**a,b**) -1.0 V; (**c,d**) -1.5 V; (**e,f**) -2.0 V vs Ag/AgCl sat. KCl reference electrode for 10 min of deposition and 15 min of etching time.

The depositions from the Au(I) solution were much more homogeneous (top-views), and the nanowires production presented (cross-sections) overall better separation and narrowness of the silicon nanowires with a pronounced aspect ratio.
The deposits were characterized before the etching in terms of equivalent thickness and coverage. Regarding the Au(III) solution, it was found that the best result was obtained at potential -2 V for 10 minutes, suggesting that a higher amount of deposition helps to obtain better nanowires.
The use of the Au(I) solution resulted in the formation of nanowires under a wider range of deposition conditions. For this solution, nanowires were not obtained only for the deposition carried out at -1 V for 5 minutes, suggesting once again that a more abundant deposition favors the formation of high-quality nanowires. In **Figure 29d**, the formation of silicon nanowires is clearly observed, with individual wires of approximately 50 nm of diameter and a length of 3.7 μm. Nanowires of this type yield a surface area enhancement of approximately 300 times relative to the initial planar surface. The metal nanoparticles produced across the 12 tests had diameters ranging from approximately 50 to 120 nm. The smallest particles were obtained using a -1 V potential for 5 minutes in the Au(III) solution, while the largest were observed at -2 V for 10 minutes in the Au(I) solution. As the applied potential and deposition time increase, the average diameter of the nanoparticles increases. The use of the two different formulations does not significantly differentiate the average nanoparticle size.
The nanowires and cavities obtained show average lengths from 5 μm to 19 μm, with the greatest depth of etching obtained in the case of deposition at -2 V for 10 minutes in the Au(III) solution and the lowest at -1.5 V for 10 minutes in the Au(I) solution. The average etching rate was in the range of 0.4-1.3 micrometers per minute. The lowest average etching rate was found in the case of the deposition obtained in Au(I) solution with 10-minute depositions at a potential of -1.5 V. The highest etching rate was obtained in the case of deposition carried out at -2 V for 10 minutes in Au(III) solution.
The average equivalent thickness of the deposit and the surface coverage were evaluated and reported in **Figure 30**. EDS measurements were carried out using the Layer Probe program of AZteclive. These measurements were aimed at investigating the average equivalent thickness of the gold deposit on the silicon surface. The best results in terms of nanowire morphology were obtained in the case of the depositions with higher surface coverage and equivalent thickness, confirming the hypotheses previously made.

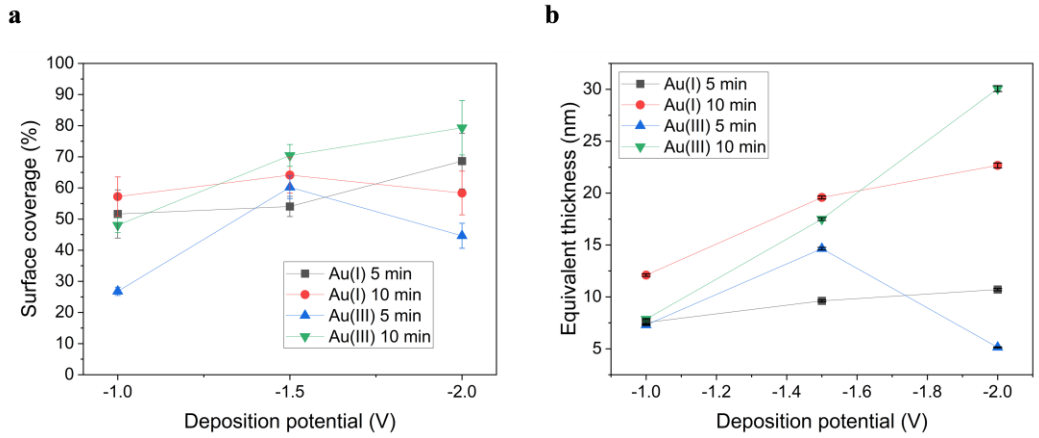

Figure 30 (**a**) Surface coverage; (**b**) equivalent thickness characteristics of the gold deposit obtained on the silicon working electrode. The reported errors are calculated based on three independent measurements.

Table 6 provides a step-by-step summary of the process, highlighting key findings related to deposition time and applied potential.

Table 6 Step-by-step table summarizing the experimental process, with a summary of the deposition conditions and results.

Step	Parameters	Details	Results/Observations
1	Substrate Preparation	RCA cleaning of n-type Si (100) wafers	Clean, oxide-free silicon surface
2	Electrochemical Cell Setup	Dark conditions, 3-electrode cell	Minimized photonic effects, reproducibility ensured
3	Gold Salt Selection	Au(I): $KAu(CN)_2$, pH 4; Au(III): $KAu(CN)_4$, pH 1	Comparative study of oxidation states and pH effects. The Au(I) solution produced more homogeneous deposits and yielded silicon nanowires with better separation, and higher aspect ratios
4	Deposition Parameters	Potential: -1.0 V, -1.5 V, -2.0 V Time: 5 and 10 min	Comparative study of deposition potential and duration. 12 samples total (6 per formulation). Using a more negative applied potential and longer deposition time generally promotes the growth of high-quality nanowires
5	SEM + EDS Analysis	Gold deposition analysis	Surface coverage, particle size, equivalent thickness measured
6	MACE Etching	5 M HF + 0.44 M H_2O_2, 15 minutes	Vertically aligned nanowires, etching rate range 0.4–1.3 μm/min
7	Final NW Characterization	SEM cross-sections	Best results: 50 nm diameter, 3.7 μm length

Table 7 offers an overview of the deposition conditions along with the corresponding characterization results.

Table 7 Summary of the deposition conditions and the corresponding characterization results. The reported errors are calculated based on three independent measurements.

		Surface coverage (%)		Particle size (nm)		Equivalent thickness (nm)		Nanowires length (µm)	
		Formulation		Formulation		Formulation		Formulation	
Time	Potential	Au I	Au III	Au I	Au III	Au I	Au III	Au I	Au III
5 min	-1.0 V	52 ± 8	27 ± 1	15 ±2	57 ± 33	7.5 ± 0.1	7.3 ± 0.1	15 ± 2	x
	-1.5 V	54 ± 3	60 ± 4	14 ± 1	88 ± 34	9.6 ± 0.1	14.7 ± 0.1	14 ± 1	13 ± 1
	-2.0 V	69 ± 9	45 ± 4	14 ± 1	77 ± 31	10.7 ± 0.1	5.1 ± 0.1	14 ± 1	12 ± 2
10 min	-1.0 V	57 ± 6	48 ± 2	8 ± 1	80 ± 18	12.1 ± 0.1	7.9 ± 0.1	8.0 ± 1.01	13 ± 2
	-1.5 V	64 ± 6	70 ± 4	5.5 ± 0.4	125 ± 54	19.6 ± 0.1	17.5 ± 0.1	5.5 ± 0.4	18 ± 3
	-2.0 V	58 ± 7	79 ± 9	12 ± 1	128 ± 47	22.7 ± 0.2	30.1 ± 0.3	12 ± 1	19 ± 1

Although nanowires with a diameter of 50 nm are significantly larger than the 5–9 nm range required to observe quantum confinement effects, as reported by Irrera et al. [157], they fall within the lower end of the typical diameter range (30–200 nm) observed in metal salt-assisted etching processes [149]. Notably, they closely matches the mean diameter of 49.1 ± 5.1 nm reported by Kim et al. using a patterned Au/Ag metal mesh technique [153]. This suggests that the SiNWs produced in this work are more comparable in size to those fabricated using patterned MACE methods designed for structural control, rather than the ultrathin wires specifically synthesized for quantum confinement luminescence.

The measured length of 3.7 µm is also consistent with values typically reported for SiNWs obtained via MACE, which generally range from several to many micrometers [149].

SiNWs with dimensions comparable to those obtained in this work show strong potential for both sensing and high surface-area electrode applications. The observed diameter of 50 nm is close to the average diameter reported for SiNWs used in battery applications (approximately 89 nm with a standard deviation of 45 nm) and falls within the size range relevant for sensing devices, which often utilize diameters around 10 to 20 nm [158,159]. Importantly, the functional advantages of these applications generally extend across nanoscale diameters. Additionally, the nanowire length of 3.7 µm lies within the typical micrometer-scale range reported for both sensing and electrode uses [159].

5.4 Conclusions

In this study, SiNWs were successfully fabricated using the MACE technique, with the electrodeposition of gold, a method that diverges from the approaches commonly reported in the literature, which primarily utilize methods like PVD or galvanic displacement.

A systematic investigation was conducted on the electrodeposition parameters, including the oxidation state of the gold precursor, pH, applied potential, and deposition duration, to optimize the formation of a nanostructured gold deposit. The influence of these parameters was thoroughly examined through SEM characterization. The most suitable etching solution was identified. The correlation between deposit thickness, surface coverage, and final NWs morphology was confirmed, supporting the hypothesis that increased catalyst loading enhances the NWs formation. Key findings include the successful fabrication of NWs with diameters averaging around 50 nm and length of 3.7 μm, resulting in a surface area increase of approximately 300 times compared to the initial flat surface. Nanowires with the thinnest diameter measured 57 nm, while the longest ones reached a height of approximately 19 μm. These findings highlight the potential of electrodeposition as a viable alternative to traditional deposition techniques for MACE, also thanks to the ability to fine-tune nanowire dimensions by adjusting deposition parameters to meet diverse application requirements.

These nanowires demonstrate significant potential for applications such as high-specific surface-area electrodes, particularly when functionalized with catalytically active metals. However, this represents a prospective application of the developed systems rather than an experimentally demonstrated outcome of the present study, which was primarily focused on fabrication and morphological–structural characterization

6 Electrodeposition and Characterization of Ni–Mn–As Alloy for Oxygen Evolution Reaction (OER) optimization applications

Building on the results obtained from the electrodeposition of MnAs-based films on gold-coated silicon and from the deposition of rhodium on silicon, this part of the work aimed to synthesize a ternary Ni–Mn–As alloy on silicon substrates. The primary objective was to obtain an alloy with the desired stoichiometry and investigate its structural properties, with particular emphasis on its potential use as material for the optimization of Oxygen Evolution Reaction (OER). The Ni–Mn–As alloy system was selected as a candidate material for oxygen evolution reaction (OER)–oriented investigations due to the well-established catalytic activity of nickel-based materials and the possibility of tuning electronic and surface properties through multicomponent alloying. In particular, the incorporation of manganese is reported to influence catalytic kinetics, while NiMnAs is related in literature to Heusler-type systems, which are known for their highly tunable electronic structure and robust magnetic properties. It was therefore considered attractive to explore electronically versatile transition-metal alloys that may be favorable for electrocatalysis. Within the framework of this work, electrodeposition enables the formation of nanostructured films with increased electrochemically active surface area, features commonly associated with improved OER performance. The choice of the Ni–Mn–As system therefore aligns with both the methodological focus of the thesis on controllable alloy electrodeposition and the broader objective of investigating multifunctional alloys with potential electrocatalytic relevance. This study also served as a conceptual bridge between the electrochemical development of magnetic thin films on silicon and their future integration into nanostructured systems such as silicon nanowires.

6.1 Introduction

The electrochemical deposition of metal alloys onto silicon substrates offers a versatile strategy for integrating functional metallic properties with the electronic advantages of silicon. In this study, a ternary Ni–Mn–As alloy was electrodeposited onto silicon wafers under ambient conditions using aqueous electrolytes with controlled composition[146]. These features present clear advantages over conventional deposition methods, such as physical vapor deposition (PVD)[160]. The primary objective was to investigate the formation of a Heusler-type alloy with potential spin-filtering properties, aimed at enhancing the performance of the OER[142].

Although dedicated electrochemical OER performance tests were not the primary focus of this chapter, the morphological and compositional features of the electrodeposited Ni–Mn–As films are consistent with characteristics commonly associated with efficient OER catalysts. In particular, the formation of nanostructured and rough surfaces is known to increase the electrochemically active surface area and to promote the availability of catalytic sites. Moreover, nickel-based

alloys are widely reported as active OER materials[161], while the incorporation of additional transition metals such as manganese improves catalytic kinetics[162]. The multicomponent nature of the Ni–Mn–As system may therefore contribute to synergistic catalytic effects at the surface.

Furthermore, Ni–Mn–As compositions are related in the literature to Heusler-type alloys[163]. The theoretical prediction of a new family of materials, the semi-Heusler NiMnZ alloys (where Z = Si, P, Ge, or As), has been extensively investigated in the literature[164]. These compounds have attracted considerable interest for their potential use in future spintronic applications, mainly because, as reported in previous studies[165], they exhibit a half-metallic nature. In such systems, electrons of one spin channel behave as conductors, while those of the opposite spin act as insulators or semiconductors. This property is crucial for achieving high spin polarization.

Based entirely on computational approaches, such as ab initio molecular dynamics, several studies have analyzed their structural stability, density of states, and magnetic interactions in order to predict the Curie temperature (Tc), i.e., the temperature above which the material loses its ferromagnetism. The literature reports notably high Curie temperatures for various NiMnZ compounds, including NiMnP, NiMnAs, NiMnGe, and NiMnSi, at their equilibrium lattice constants. These predicted Tc values, significantly exceeding room temperature, together with the expected robustness of half-metallicity over a wide range of lattice parameters, make these NiMnZ alloys highly promising candidates for high-temperature spintronic devices[164].

As also discussed by Wei *et al.*[166], the half-metallic nature of these compounds, characterized by 100% spin polarization at the Fermi level, makes them ideal candidates for spintronic applications. Theoretical predictions for NiMnAs, for instance, indicate a Curie temperature (Tc) of approximately 840 K. However, the experimental realization of materials exhibiting the ideal properties predicted by theory often faces significant challenges, particularly related to synthesis and deposition processes. An experimental investigation of NiMnAs thin films grown by molecular beam epitaxy (MBE) on GaAs (110) substrates compared theoretical predictions obtained from computational methods with the properties of the real material[166]. Among the most relevant techniques to elucidate the structure and properties of these intriguing alloys is X-ray diffraction (XRD), which revealed that the NiMnAs (111) crystalline plane was deposited parallel to the GaAs (110) plane[166], an epitaxial relationship that was unexpected compared to other studies on (001) substrates. This behavior has been attributed to atomic diffusion at the film–substrate interface.

Beyond XRD, magnetic characterization is crucial to further understand these materials, particularly through measurements such as the Curie temperature (Tc). Electronic and magneto-transport investigations can provide additional insight into their intrinsic properties. For instance, measurements of resistivity as a function of temperature ($\rho(T)$) have shown a metallic behavior at low temperatures (ρ increases with T) and semiconducting behavior at higher temperatures (ρ decreases with T). Magnetoresistance (MR) analyses can also be performed: while negative MR is

common in ferromagnets, it is generally not expected in half-metals due to the absence of spin-dependent scattering. Therefore, the observation (or absence) of negative MR can help determine whether spin-dependent scattering occurs, thereby indicating the presence or absence of half-metallicity [166].

Another valuable measurement concerns the angular dependence of anisotropic magnetoresistance (AMR), which is considered particularly useful for probing half-metallicity in ferromagnetic materials[166]. In the literature, several controlled-growth techniques, such as molecular beam epitaxy (MBE), have been proposed to synthesize NiMnAs on GaAs substrates[167]. The use of electrodeposition to deposit this alloy represents an important innovation.

Characterization was therefore conducted to examine the morphology, elemental composition, and crystalline structure of the deposited material using X-Ray Fluorescence (XRF), Scanning Electron Microscopy (SEM), Energy-Dispersive X-ray Spectroscopy (EDS), X-ray Diffraction (XRD), and X-ray Photoelectron Spectroscopy (XPS). The results demonstrate the effectiveness of electrodeposition as a method for fabricating complex multi-element alloys on semiconducting substrates. The evaluation of the magnetic and spin-filtering properties will be carried out in future work.

6.2 Materials and method

Reagents

All solutions were prepared using ultrapure water with a conductivity of less than 0.059 μS/cm. All reagents were of analytical grade and were used as received without further purification. The RCA method was employed to activate the silicon electrode using the following reagents: sulfuric acid (H_2SO_4, 98%) sourced from chemPUR, Karlsruhe, Germany; hydrochloric acid (HCl, 37% w/w) and hydrofluoric acid (HF, 48% w/w) obtained from VWR International, Fontenay-sous-Bois, France; and acetone (AcOH), ethanol (EtOH), and hydrogen peroxide (H_2O_2, 30% w/w) provided by Carlo Erba, Val de Reuil, France.

The following salts were used for the electrolytic solutions: Sodium arsenite $NaAsO_2$, manganese (II) sulfate monohydrate $MnSO_4 \cdot H_2O$ 0.1 M, ammonium sulfate $(NH_4)_2SO_4$ 0.1 M, boric acid H_3BO_3, nickel (II) sulfate hexahydrate $NiSO_4 \cdot 6H_2O$, and sodium sulfate Na_2SO_4.

The above-mentioned reagents are from Merck KGaA, Darmstadt, Germany.

Experimental set-up

The electrochemical characterization and deposition system used in this study is a fully automated setup designed to control the solution input and residence time within the cell via a solenoid valve system. The solutions, stored in Pyrex glass containers, were deaerated with nitrogen gas and remotely introduced into a Kel-F (polychlorotrifluoroethylene) electrochemical cell. The solution flow rate through the cell was maintained at approximately 2 mL/s, with a total cell volume of 2 mL. To avoid photonic pumping effects on silicon, all electrodeposition processes were conducted under dark conditions. This configuration ensured reproducible depositions while minimizing surface oxidation of the silicon substrate.

Electrochemical measurements were carried out using an AMEL Model 551 potentiostat, interfaced with a personal computer equipped with a National Instruments data acquisition card. A conventional three-electrode setup was employed, consisting of a monocrystalline (100) n-type silicon working electrode (0.001–0.005 Ω·cm) with an exposed surface area of 0.785 cm^2, a gold counter electrode, and an Ag/AgCl (saturated KCl) reference electrode. Prior to measurements, the silicon electrodes were cleaned and activated according to the RCA procedure, as detailed in section 4.2 Materials and Methods.

Scanning Electron Microscopy (SEM) analyses were performed using a Hitachi SU3800 microscope (Hitachi High-Tech Corporation, Tokyo, Japan) equipped with an Ultim Max 40 Analytical Silicon Drift EDS Detector (Oxford Instruments plc, Abingdon, UK). Energy-dispersive X-ray spectroscopy (EDS) measurements were carried out using the Layer Probe function of AZtecLive software (Version 5.0) to estimate the average equivalent thickness of the metallic deposits.

6.3 Results and discussion

Preliminary electrochemical studies were performed using an Au working electrode in an electrolyte solution. The blank solution consisted of 0.10 M H_3BO_3 and 0.10 M $(NH_4)_2SO_4$. Metal salt solutions were prepared by adding 0.01 M $NiSO_4 \cdot 6H_2O$, 0.01 M $AsNaO_2$, and 0.01 M $MnSO_4 \cdot H_2O$ to the electrolyte.
Figure 31 shows the cyclic voltammograms recorded in the blank electrolyte and in the presence of individual metal ions (Ni, As, and Mn). The comparison highlights the different cathodic and anodic current responses associated with each species. In particular, the increase in cathodic current at negative potentials is mainly related to hydrogen evolution, apart from the As-containing solution, where a reduction peak is observable around −0.4 V. The anodic features observed close to -0.3 V in the Ni- and As-containing solutions indicate the onset of oxidation processes. The absence of additional well-defined reduction peaks for As and Mn suggests that their electrochemical responses are either kinetically hindered or partially masked by dominant background reactions.

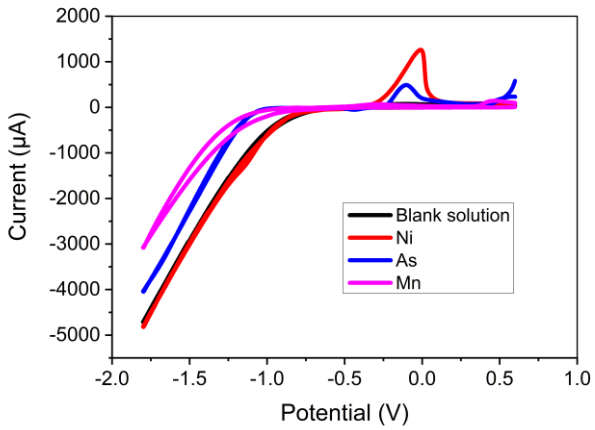

Figure 31 CV of 0.10 M H_3BO_3 and 0.10 M $(NH_4)_2SO_4$. Metal salt solutions were prepared by adding respectively 0.01 M $NiSO_4 \cdot 6H_2O$, 0.01 M $AsNaO_2$, and 0.01 M $MnSO_4 \cdot H_2O$ to the electrolyte. Between 0.6 V and -1.8 V vs Ag/AgCl sat. KCl, scan rate 10 mVs^{-1}, pH 7, on gold WE.

A series of trial-and-error experiments were carried out to evaluate the effects of deposition potential, deposition time, pH, and electrolyte concentration.
The best deposition conditions to obtain a deposit with an atomic ratio close to 1:1:1 were achieved at a deposition potential of −2.0 V for 60 seconds, using an electrolyte containing 0.02 M $AsNaO_2$, 0.01 M $NiSO_4 \cdot 6H_2O$, 0.10 M $MnSO_4 \cdot H_2O$, and 0.50 M $(NH_4)_2SO_4$ at pH 7. The composition of the resulting deposit, determined by XRF

analysis, was Mn 24.9 ± 0.9%, Ni 39.8 ± 0.1%, and As 35.3 ± 0.3% (atomic percentage, excluding all other elements).
The obtained deposit can be observed in **Figure 32**. As shown, the film consists of an agglomerate of globular structures characterized by nanometric dimensions.

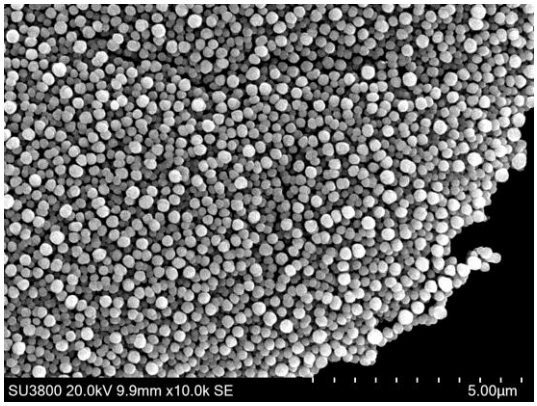

Figure 32 SE-SEM image of the deposit obtained at −2.0 V vs vs Ag/AgCl sat. KCl, for 60 seconds, using an electrolyte containing 0.02 M $AsNaO_2$, 0.01 M $NiSO_4 \cdot 6H_2O$, 0.10 M $MnSO_4 \cdot H_2O$, and 0.50 M $(NH_4)_2SO_4$ at pH 7, Au working electrode.

Drawing on the information obtained from the assessment of deposition conditions on gold substrates, experimental deposition trials were performed on silicon electrodes.
With the aim of achieving a stoichiometric Ni:Mn:As ratio of 1:1:1, the deposition parameters were optimized by evaluating different experimental conditions. Specifically, two concentrations of the nickel-containing salt (0.02 M and 0.01 M), two concentrations of the arsenic-containing salt (0.02 M and 0.01 M), and four concentrations of the manganese-containing salt (0.2 M, 0.1 M, 0.05 M, and 0.035 M) were tested. The selected nickel concentrations were chosen based on values commonly reported in the literature and were subsequently fine-tuned following preliminary experimental trials.[168]
Additionally, two different electrolytes ($(NH_4)_2SO_4$ 0.5 M and Na_2SO_4 0.5 M) were compared, along with the presence or absence of 0.1 M H_3BO_3. The effect of three deposition pH values (8, 7, and 6), three deposition times, and six different deposition potentials (-2.5 V, -2.0 V, -1.75 V, -1.5 V, -1.25 V, and -1.0 V) were also investigated.
The best stoichiometric ratio was obtained under the following operating conditions: a deposition potential of –1.75 V applied for 60 seconds, using an electrolyte containing 0.01 M $AsNaO_2$, 0.02 M $NiSO_4 \cdot 6H_2O$, 0.035 M $MnSO_4 \cdot H_2O$, and 0.5 M Na_2SO_4, with the deposition carried out at pH 7. The composition of the resulting deposit, determined by XRF analysis, showed an atomic percentage of Mn 38.8%,

Ni 31.1%, and As 30.1%. The NiMnAs film exhibited a thickness of 0.077 μm, as evaluated through SEM analysis using the Layer Probe software, as previously described in this thesis.
The structural morphology of the deposit grown on silicon can be assessed by examining **Figure 33**, which provides a detailed view of the surface features.

a **b**

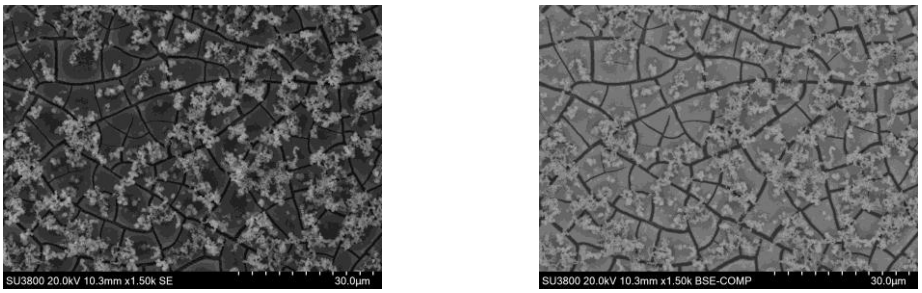

Figure 33 (**a**) SE-SEM and (**b**) BSE-SEM images of the deposit obtained at −1.75 V vs vs Ag/AgCl sat. KCl, for 60 seconds, using an electrolyte containing 0.01 M $AsNaO_2$, 0.02 M $NiSO_4 \cdot 6H_2O$, 0.0.35 M $MnSO_4 \cdot H_2O$, and 0.50 M $(NH_4)_2SO_4$ at pH 7, Si working electrode.

The observed differences in deposit morphology between silicon and gold substrates can be attributed to the distinct surface and structural properties of the two materials. Differences in crystal structure, surface energy, and nucleation behavior influence the initial stages of metal growth. Moreover, the presence of a native oxide layer on silicon and its different surface wettability compared to gold can further affect adhesion and growth mechanisms, leading to variations in grain size, roughness, and overall morphology of the electrodeposited films.
Table 8 and **Table 9** show the complete list of deposition tests carried out on silicon substrates**. Table 8** reports the results obtained using the $(NH_4)_2SO_4$ electrolyte, while **Table 9** presents those obtained with the Na_2SO_4 electrolyte.

Table 8 Summary of all depositions performed on silicon substrates using the $(NH_4)_2SO_4$ electrolyte (0.5M). The reported results are calculated based on five independent measurements.

Sample	t (s)	Pot. (V)	pH	Mn (M)	Ni (M)	As (M)	Thickness (µm)	Mn (atm%)	Ni (atm%)	As (atm%)
2	60	OC*	7.0	0.1	0.01	0.02	0.061	2.1%	58.0%	39.9%
3	60	-2.0	7.0	0.1	0.01	0.02	0.104	19.6%	46.9%	33.5%
4	60	-2.5	7.0	0.1	0.01	0.02	0.119	15.1%	45.5%	39.4%
6	60	-1.5	7.0	0.1	0.01	0.02	0.055	8.9%	55.3%	35.8%
7	60	-1.0	7.0	0.1	0.01	0.02	0.026	0.0%	56.5%	43.5%
8	60	-2	7.0	0.2	0.01	0.02	0.121	15.0%	50.9%	34.1%
9	60	-1.5	7.0	0.2	0.01	0.02	0.060	9.0%	52.3%	38.7%
10	60	-2.5	7.0	0.2	0.01	0.02	0.086	9.7%	52.1%	38.2%
11	60	OC*	7.0	0.2	0.01	0.02	0.038	0.0%	56.3%	43.7%
12	60	-2.0	7.0	0.1	0.01	0.01	0.089	11.4%	57.0%	31.6%
13	60	-1.5	7.0	0.1	0.01	0.01	0.049	14.8%	54.4%	30.7%
14	60	-2.5	7.0	0.1	0.01	0.01	0.101	11.6%	58.2%	30.2%
17	120	-2.0	7.0	0.1	0.01	0.01	0.159	15.6%	55.6%	28.7%
18	30	-2.0	7.0	0.1	0.01	0.01	0.048	11.4%	55.3%	33.4%
19	60	-2.0	5.9	0.1	0.01	0.01	0.092	12.6%	56.3%	31.1%
20	60	-2.0	8.0	0.1	0.01	0.01	0.108	18.8%	54.1%	27.1%

*Overcurrent (OC)
Potential (Pot.)

Table 9 Summary of all depositions performed on silicon substrates using the Na_2SO_4 electrolyte (0.5M), deposition time 60 seconds. The reported results are calculated based on five independent measurements.

Sample	Pot. (V)	pH	Mn (M)	Ni (M)	As (M)	Thickness (μm)	Mn (atm%)	Ni (atm%)	As (atm%)
22	-2.0	7.0	0.100	0.01	0.01	0.17	76.5%	11.9%	11.6%
23	-1.5	7.0	0.100	0.01	0.01	0.06	55.8%	18.1%	26.1%
24	-2.5	7.0	0.100	0.01	0.01	0.51	78.1%	11.1%	10.7%
25	-2.0	7.0	0.050	0.01	0.01	0.16	67.0%	17.7%	15.3%
26	-1.5	7.0	0.050	0.01	0.01	0.10	59.2%	19.8%	20.9%
27	-2.5	7.0	0.050	0.01	0.01	0.01	39.1%	21.2%	39.7%
28*	-2.0	7.0	0.050	0.01	0.01	0.14	50.1%	22.4%	27.5%
29*	-2.5	7.0	0.050	0.01	0.01	0.17	60.7%	20.5%	18.9%
31*	-1.5	7.0	0.050	0.01	0.01	0.04	5.9%	52.3%	41.9%
32	-2.0	7.0	0.050	0.02	0.01	0.24	55.1%	30.2%	14.7%
33	-1.5	7.0	0.050	0.02	0.01	0.10	51.5%	32.2%	16.3%
34	-2.5	7.0	0.050	0.02	0.01	0.04	58.2%	24.9%	17.0%
36	-2.0	7.0	0.035	0.02	0.01	0.01	25.4%	54.2%	20.4%
38	-1.75	7.0	0.035	0.02	0.01	0.08	38.8%	31.1%	30.1%
37	-1.5	7.0	0.035	0.02	0.01	0.10	48.0%	35.9%	16.1%
39	-2	7.0	0.035	0.02	0.01	0.02	34.3%	48.3%	17.5%
40	-1.75	7.0	0.035	0.02	0.01	0.04	44.7%	39.3%	16.0%
41	-1.25	7.0	0.035	0.02	0.01	0.04	27.2%	45.2%	27.6%
44A	-1.5	7.0	0.035	0.02	0.01	0.08	46.3%	37.1%	16.6%
44B	-1.5	7.0	0.035	0.02	0.01	0.12	48.1%	34.2%	17.7%
44C	-1.5	7.0	0.035	0.02	0.01	0.13	48.3%	35.7%	15.9%
44D	-1.5	7.0	0.035	0.02	0.01	0.06	41.6%	37.5%	20.9%
44E	-1.5	7.0	0.035	0.02	0.01	0.06	43.7%	37.1%	19.3%
45	-2	7.0	0.035	0.01	0.01	0.07	60.3%	16.8%	22.9%

* Solution also containing H_3B0_3 0.1 M
Potential (Pot.)

The deposition time appears to have a significant impact on the final film thickness, with longer deposition times resulting in thicker deposits. However, the available data on elemental composition is too limited to draw reliable conclusions regarding the influence of time on the relative percentages of Ni, Mn, and As.
Changing the electrolyte leads to a substantial variation in the manganese concentration, with the Na_2SO_4 electrolyte showing an increase in Mn content. This is probably due to the fact that ammonium sulfate forms manganese–ammonia complexes[44]. Although the average proximity of the results to the desired 1:1:1 stoichiometric ratio is comparable between the two electrolytes, the use of Na_2SO_4 tends to yield compositions closer to the ideal ratio.

The concentration of the individual metal salts, on the other hand, does not appear to have a clear or systematic effect on the stoichiometric ratio of the three metals in the final deposit.
The use of boric acid, tested as an additive due to its common employment in formulations used for nickel electrodeposition, did not lead to evident improvements when compared with results obtained under the same operating conditions. For this reason, it was not employed in subsequent experiments, in order to avoid introducing additional variables into the system.
Preliminary XRD analyses performed on the deposits did not reveal any clear evidence of crystalline structures attributable to NiMnAs compounds.
XPS analysis confirmed the presence of all three elements Ni, Mn, and As in the deposit. However, quantitative evaluation of their relative concentrations is rather complex. The sample was analyzed both as-deposited and after argon sputtering for 15 minutes to remove the outermost surface layer. It is well known that ion sputtering can induce modifications in the chemical composition and oxidation states of multicomponent materials due to preferential sputtering, and beam-induced reduction effects. In this work, Ar^+ ion sputtering was performed using an Ar^+ ion beam with an acceleration energy of 3 keV and a beam current of 10 mA, under an argon pressure of approximately 5×10^{-5} bar.
In the first case (before sputtering), the approximate atomic composition was Ni 43%, Mn 26%, and As 31%. After sputtering, the composition changed to Ni 26%, Mn 54%, and As 21%. The observed compositional changes after argon sputtering could indicate that the as-deposited surface was enriched in Ni and As, likely as a result of surface segregation or oxide formation, whereas the underlying bulk is Mn-rich, which is revealed upon removal of the outermost layer.

In figure **Figure 34** is possible to observe the results obtained.

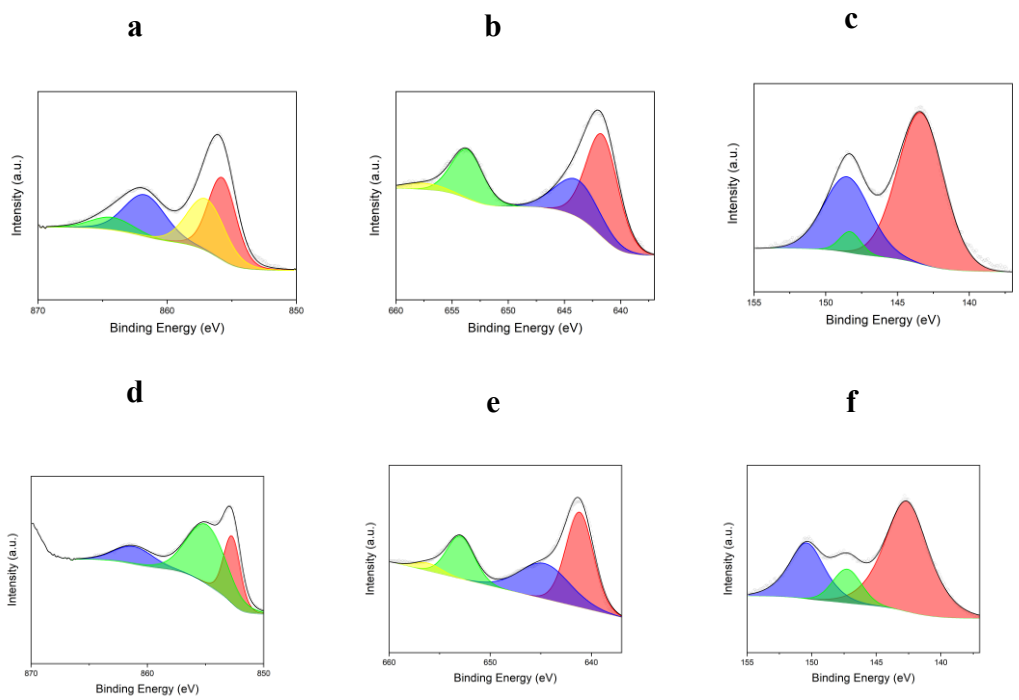

Figure 34 XPS spectra of the deposit obtained on the silicon substrate: (**a**) Ni $2p_{3/2}$; (**b**) Mn 2p; (**c**) As 3p; (**d**) Ni $2p_{3/2}$ after Ar sputtering; (**e**) Mn 2p after Ar sputtering; (**f**) As 3p after Ar sputtering.

6.4 Conclusions

Comprehensive analytical characterization was conducted to examine the morphology, elemental composition, and crystalline structure of the deposited material using X-Ray Fluorescence (XRF), Scanning Electron Microscopy (SEM), Energy-Dispersive X-ray Spectroscopy (EDS), X-ray Diffraction (XRD), and X-ray Photoelectron Spectroscopy (XPS). The results demonstrate the effectiveness of electrodeposition as a method for fabricating complex multi-element alloys on semiconducting substrates and underscore the critical role of analytical techniques in optimizing material properties for electrochemical applications.

in any case, no crystal structure attributable to a NiMnAs compound was found, therefore further deposition tests and characterization will be necessary to evaluate the possibility of obtaining a Heusler alloy.

In the present phase of the study, the primary objective was the simultaneous co-deposition of Ni, Mn, and As with controlled compositional ratios rather than a systematic optimization of surface morphology. Nevertheless, it is well established that deposition parameters such as applied potential, ion concentration, and deposition time strongly influence nucleation and growth mechanisms, and consequently the resulting film morphology. In this work, variations in morphology were observed qualitatively as a secondary effect of the compositional optimization process.

Future work will focus on the detailed characterization of the morphology and magnetic properties of the deposits. This step is essential to evaluate whether the synthesized material exhibits the ferromagnetic behavior and spin polarization.

7 Advances and Challenges in Sustainability of the Decorative Electroplating Industry

A further and equally significant component of this doctoral research addressed the industrial and environmental dimensions of electrodeposition. This chapter focuses on the transition toward sustainable practices in the decorative electroplating industry, emphasizing the elimination of cyanide-based baths, the recovery and reuse of metals, and the implementation of environmentally responsible technologies. The study provides a critical evaluation of current industrial practices and highlights the progress, challenges, and strategic directions necessary to achieve full compliance with international sustainability standards and regulatory objectives.

7.1 Introduction

The process of electroplating is vital in many industries that produce modern aerospace materials and electronics[142,169], heavy equipment, cars, decoration and fashion[170,171]. The increasing focus on sustainability within several areas has also seen a critical re-evaluation of electrodeposition practices within the context of the United Nations' sustainable development goals (SDGs)[172]. The main critical items regarding the plating industry lie within the environmental sector, from production to disposal, and health within the workplace[173,174]. Electroplating, in many instances, involves hazardous agents such as cyanides, chromium and nickel, which adversely affect the environment and human beings[175]. Some of the traditional processes consume a great deal of energy, thus contributing to the carbon footprint of the industry[176,177]. The production of galvanized items often involves the extensive use of scarce materials such as gold and palladium, which have challenges associated with their mining processes. The issue of toxic manufacturing waste and how to dispose of it is a major environmental concern, involving high costs and risks.

These are well-known problems that drive research in this area; major themes include finding ways to replace toxic compounds with less hazardous alternatives. For instance, cyanide-free[178–182] electroplating baths and nickel-free processes are among the ways of reducing such risks. Others are the use of innovative alloys that minimize precious materials, as well as solutions seeking to ensure the needed performance whilst employing small quantities of costly metals and to carry out cleaner fabrication, minimizing the production of toxic wastes. Additional measures include encouraging recycling efforts to regain valuable components from electroplating waste, expansion of investment into more energy-efficient technology in processes[183–185] and the use of pulsed or modulated currents to enhance deposition efficiency[186–188].

The issue is complicated and linked almost exclusively to the ecological problems such as pollution relating to the industry of electroplating. However, it is important to recall that sustainability is a wider and more complex notion. Economic and social elements frequently remain disregarded as attention is primarily directed toward ecological issues. Therefore, corporate strategies embrace green topics that are tied to the communities where the corporations operate and reflect on economic

considerations as well. However, only through a single vision that takes into consideration these needs can the electroplating industry and all the others respond to these challenges equitably and responsibly.

To make the industrial process more sustainable, there is a need to train operators in sustainable practices and environmental awareness with a view that such procedures will take root on the industrial scale. Collaboration between industries and research institutions is essential to set up sustainable guidelines for the electroplating sector as well as share the benchmarks. Furthermore, government-backed policies and incentives should be established for promoting cleaner technology, sustainable R&D, etc., within industry. Finally, investors should be encouraged in the development of green technologies as well as research efforts towards sustainability and, ultimately, the adoption of greener processes.

Mathematical models have been developed as well as artificial intelligence methods used to optimize processes and reduce the effect on the environment as part of addressing sustainability problems[170,189,190]. Some of them consist of activity such as "Pollution prevention" (P2) which has played an integral role in the development and implementation of technologies designed to prevent the amount of waste generated at a facility. The P2 approach is extended to "Profitable P2" (P3), which seeks economic benefits with environmental reduction[191], and even "Cooperative P3" (CP3) for industrial areas to aid in decision making toward sustainable development[192].

Song[193], in 2016, explained the prevalent sustainability measurement systems but stressed the need to generate a specific system of metrics for evaluating the sustainability performance of the electroplating industry. These comprise economic sustainability indicators, environmental sustainability indicators and social sustainability indicators. These indicators focus on issues that include profit, value addition, energy, material usage, water consumption and emissions, among many other factors.

In 2015, the United Nations stated 17 SDGs for development of the world's agenda in elimination of global challenges, improvement of the living standards of people and protection of the planet until 2030. The 17 SDGs are a universal call for an end to poverty and a beginning to prosperity, health and life on earth. The electroplating industry is also based on a thorough critical analysis of the SDGs as a starting point to identify directions for improving sustainability.

Several SDGs are closely related to electrodeposition in a direct perspective. One such example could be SDG 9 (industry, innovation, and infrastructure), which could advance efficiency and lessen environmental effects with such technologies as electrodeposition. This is why modern electrodeposition technologies have been adopted as an element of innovations that enhance efficiency and reduce environmental pollution. The development of more sustainable processes through research is key for the industry's growth. New materials and novel electroplating processes can also be utilized to the benefit of the decorative sector and, to a certain extent, of the technical sector, supplying eco-aesthetic solutions. Simultaneously, attention to responsible utilization of chemical resources that follows SDG 12 becomes vital. Reducing the content of precious metals in electroplating processes

is an important contributor to the more responsible use of resources and answers consumers' demand for more sustainable products. The development of cyanide- and nickel-free electrolytes is one step towards a safer and more sustainable operation process. The strategy can achieve SDG 7 (clean and accessible energy) due to the implementation of low-energy-consumption and ambient-temperature processes that lead to lower environmental impacts associated with energy consumption; it is related to SDG 13 (climate action) as well. Water resource management and sustainability in the context of SDG 6 (clean water and sanitation), where efforts are taken for the reduction of water consumption in electroplating. Investment in research and development of the electroplating industry by innovative methods can lead to improved economic growth and skilled jobs according to SDG 8 (decent work and economic growth). There are other issues relating to employment and economic development, even in the artisanal contexts.

Sustainability of the electroplating system can be regarded as an integration of waste minimization, production enhancement and social sustainability [193]. Environmental impact and health burdens can be effectively reduced by waste reduction. In addition, waste reduction refers to chemicals, sludge, water and energy. Social sustainability involves looking at issues that relate to customer satisfaction, employee satisfaction and local community satisfaction.

Economic globalization has put a strain on the electroplating industry [194–196]. Most electroplating companies are usually working at a loss, as well as using rather obsolete technologies. Moreover, the industry is one of the most polluted among the manufacturing industries. The sustainability of a production is also the consequence of the efficiency of the process, management and workflows. There are already existing management methods and new ones are being developed constantly to meet this goal. Lean production and manufacturing are methodologies which are designed for the improvement of efficiency, the reduction of waste and the enhancement of the quality in the production processes. The idea of lean production was born in the 1950s with the Toyota Production System and was greatly developed by Taiichi Ohno at Toyota, thus forming the Toyota Production System (TPS)[197]. This system is mainly centered on the reduction of waste and the improvement of the processes to attain the total quality. The production of any product must be sustainable, and this means the processes, management and workflows must be streamlined. The fundamental elements of lean manufacturing are the 5S method (Sort, Set in order, Shine, Standardize, Sustain) for workplace organization, Just-In-Time (JIT) production to cut down on inventory and produce only when required and Poka-Yoke devices to prevent errors. The lean model, which is based on Eastern philosophy, then spread globally, highlights the idea of production flow and takt time, which is the main feature of its approach.

Six Sigma, a quality management methodology that was created by Motorola in the 1980s, is another system that aims at the improvement of product quality by the reduction of the process defects[198]. Six Sigma uses a number of statistical tools to minimize variability and reach the point of perfection, that is, few defects per million opportunities. The methodology follows two main approaches: DMAIC (Define, Measure, Analyze, Improve, Control)[199,200] for the enhancement of the existing

processes and DMADV (Define, Measure, Analyze, Design, Verify)[201,202] for the design of new processes or products. It is a highly analytical and numerical model, which is basically a data- and statistics-based model that aims at making improvements.

The Lean Six Sigma is the method that combines the principles of the lean manufacturing and Six Sigma[203]. This combination of theory and practice is designed to cut down waste and process variability; thus, the productivity will be increased, and the quality will be improved. The Lean Six Sigma methodology employs lean tools to make the processes efficient and Six Sigma tools to guarantee the process control and quality enhancement.

In decorative electroplating, lean principles could be used to make the process of work more efficient, reduce waste and enhance the quality of the plated products[204,205]. The 5S method could be used to organize the workspace, so that the tools and materials are within easy reach, thus, it will reduce the time spent searching for them and minimize the delays. JIT could be applied to the inventory management; thus, the only amount of the raw materials is available when needed, thus, reducing the storage costs and the waste. The Poka-Yoke devices could be used to avoid the usual errors in the plating process, for example, wrong chemical mixtures or the improper handling of materials.

Six Sigma methodologies, mostly DMAIC, could be used in the electroplating process to discover and eliminate the causes of defects; thus, each step of the process can be improved for high quality[206]. To illustrate, by finding out the thickness and the uniformity of the plating, the causes of the variations and the ways of improvement can be investigated, and the process can be made more consistent and of higher quality.

The Lean Six Sigma concept has given powerful tools to improve the efficiency, cut the waste and to enhance the quality in different industries including decorative electroplating and fashion[207]. These methods create a culture of continuous growth, which in turn makes the organizations more competitive and customer oriented.

This thesis discusses in detail some newly established eco-friendly practices in this industry that may benefit the environment, human beings and society. The aim will be to present a vision for a future in which electrodeposition does not only respond to the technological requirements but goes further towards a more sustainable environment through case studies and analysis of challenges faced today. Several computations techniques for predicting new formulations without using harmful substances are described specifically. Commercial systems for the better homogeneity and compaction of galvanic deposits to cut down on the amount of material being used will be discussed with some case studies. In the last, treatment and disposal or recovery of wastewater metals for the environmental protection, as well as for the economic benefit of recycling valuable metals, will be analyzed.

7.2 Results and discussion

Computational Methods

Although many attempts to improve the sustainability[208] of an electroplating plant by optimizing the whole process have been made by companies in the decorative industry, the R&D process for the optimization of the numerous variables is still based on a trial-and-error method. In this scenario, in silico procedures are trending, as the cut-and-try approach could be translated from the production plant to a chip, or even avoided by introducing predictions and systematic studies. Furthermore, in silico approaches are in line with the sustainable model proposed in Agenda 2030 by United Nations[209]. Specifically, three sustainable developments goals (SDG) are achievable: 3 (good health and well-being), 8 (decent work and economic growth) and 10 (reduced inequalities). SDG 3 is related to the reduction and, possibly, the elimination of hazards in the R&D phase; moreover, the prediction and development of new green processes is fundamental to ensure a healthy working environment in production departments. Shifting the workplace from a laboratory to a computer ensures that people with motor-related impairments can express their full creative potential, as they are no longer limited by structural barriers, accomplishing SDGs 8 and 10. To model an electrochemical process, it is helpful to distinguish two different families of simulations, distinguished by their scale: atomistic simulations[210] and multiphysics simulations[211]. The latter are divided further in ab initio and classical approaches, the first one based on quantomechanic calculations and the second one on classical mechanics.

Atomistic Simulations

Atomistic simulations are helpful to develop new sustainable additives or to understand how the different components of a bath formulation, such as additives and ions[212], interact with each other[213], but they are not yet suitable for industrial practice as they are typically limited to university facilities due to the need for high-performance computers[214] and, above all, an in-depth knowledge of all the chemical and physical processes that are involved. As stated before, molecular systems can be modeled by molecular mechanics (MM), quantum mechanics (QM) or a mix of both (QM/MM). In MM, molecules are considered in terms of bonded atoms with the bond described as a spring. MM is based on the three principles of Newtonian mechanics, with the equation of motion described by the second principle. In MM, it is convenient to describe the system in terms of a Hamiltonian (H_{MM}); if the generalized coordinates are not explicitly time-dependent and if the forces are derivable from a conservative potential (V_{MM}), it can be represented as the sum of a kinetic term K_{MM} and V_{MM} (Equation (13)).

$$H_{MM} = K_{MM} + V_{MM} \tag{13}$$

The union of the form of the functional and parameters[215] is known by the name of Force Field. There are many of them specialized in reproducing different situations, e.g., to simulate organic molecules and ligands, the GAFF protocol family is

recommended[216–218]. Despite that, the basic form of a potential functional is expressed in Equation (15) with $V_{bounded}$ taking into account covalent terms as bond stretching ($V_{bending}$), bending and dihedral torsions ($V_{torsion}$) and $V_{non\text{-}bounded}$ representing non-covalent terms as electrostatic ($V_{coulombic}$) and Van der Waals (V_{VdW}) interactions.

$$V_{MM} = V_{bounded} + V_{non-bounded} \tag{14}$$

$$V_{bounded} = V_{stretching} + V_{bending} + V_{torsion} \tag{15}$$

$$V_{non-bounded} = V_{Coulombic} + V_{vdw} \tag{16}$$

MM, depending on classical mechanics, has a much lower computational cost than QM; although it does not explicitly take electrons into account and thus cannot simulate important phenomena such as bond formation and cleavage, it is widely used to simulate large systems and physical adsorption of organic molecules on metallic surfaces. MM has been already successfully employed to study adsorption mechanism of Ni-Ammonium complexes on Ni nanocones[219] and the adsorption of bath's impurities (such as Zn) in Ni electroplating baths[220]. Furthermore, MM has been successfully used in the screening of pyrophosphate copper bath additives[221].
On the other hand, QM describes molecules in terms of electrons and nuclei with no references to bonds. The basis of QM is the Schrödinger equation, which is reported, in the time-independent form, in Equation (17), where H_{QM} is the QM Hamiltonian operator, E is the energy of the system and Ψ is the wavefunction[222].

$$\widehat{H_{QM}}\Psi = \mathrm{E}\Psi \tag{17}$$

To solve Equation (17), there are two families of methods: one based on wavefunctions as in the Hartree–Fock and post-Hartree–Fock methods (e.g., Møller–Plesset, Configuration Interaction, Coupled Cluster) and one based on the density functional theory (DFT). Despite post-HF methods have been proven to give better results, going under the chemical[223], their computational cost makes it prohibitively expensive to study typical electroplating systems composed of many atoms and transition metals. Hence, DFT and hybrid DFT methods are the preferred options for the study of electrochemical systems given the compromise between accuracy and computational cost. Ab initio calculations have been employed to study the interaction of commercial additives[224] for copper electroplating with a Cu (111) surface[225] and to study the efficiency of novel suppressors for Cu acid baths[226].
To simulate large chemical systems such as electrolyte baths for decorative application, it is possible to adopt a QM/MM approach[227] defining an active space that is going to be treated QM. Consequently, the QM/MM Hamiltonian can be defined as in Equation (18) where H_{QM} and H_{MM} are, respectively, the QM and the

MM Hamiltonians and H_{QM-MM} is the operator taking into account the interactions between the MM system and the QM active space[228].

$$\widehat{H_{QM/MM}} = \widehat{H_{QM}} + \widehat{H_{MM}} + \widehat{H_{QM-MM}} \quad (18)$$

This methodology makes it possible to perform cost efficient simulations, even on big systems, as it is capable of combining the speed of MM with the accurate description of phenomena by QM. However, this is only possible through in-depth knowledge of the system, so as effectively define the active space. QM/MM approaches are rarely used to characterize electrochemical systems but they are widely used to characterize active sites of metalloproteins[229]; nonetheless, the methodologies can be transferred to electrodeposition as well.

Multiphysics Simulations

Multiphysics approaches, based on fluid dynamics simulations, are a reliable tool to understand how the design of manufacts and anodes can influence the thickness distribution due an inhomogeneous current density distribution, even using ordinary computers. Especially in the decorative field, where the lack of sustainability is also related to a compartmentalization of entities involved (e.g., artistic direction, metalworking company and electroplating facility), the geometry of artifacts and goods is not designed to minimize the thickness dispersion, presenting cusps and valleys where the charge density changes dramatically[230]. An example of a complex accessory can be appreciated in **Figure 35**, it was electroplated following the industrial standard for an hypoallergenic cycle (ISO 1811[231]), made of Copper/White Bronze/Palladium-Nickel/Gold, where copper is used as leveler and brightener layer[232], while white bronze and palladium are used as an anticorrosion layer[233] and a barrier layer against intermetallic diffusion[234].

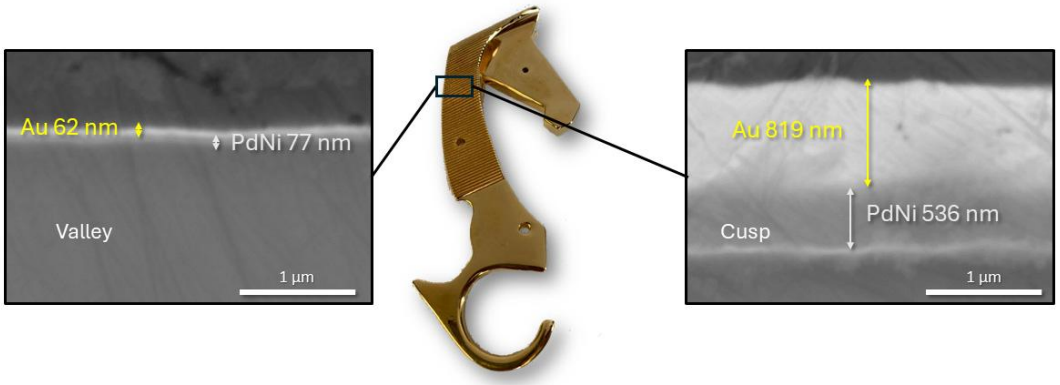

Figure 35 Fashion accessories presenting a complex geometry made of many cusps and valleys to represent a horse crest; the difference in deposited thicknesses of precious metals on a cusp and a valley observed in a cross section of the sample by a scanning electron microscopy (SEM) analysis.

The effect of the geometry in current distribution is also depicted in Figure 1, where, thanks to scanning electron microscopy (SEM) imaging, carried out at 20 kV, the difference in the thickness of layers is clearly influenced by the shape of the object. A simple but effective simulation of the current density distribution along the cathode and its influence over the thickness dispersion can be achieved by simply considering the primary current distribution[235] (i.e., the current distribution, which depends only on the gradient of the electric potential and the resistivity of the medium[236]). To better reproduce an electrolysis, including secondary (i.e., the current distribution that consider charge-transfer processes and mass transport at electrodes[237]) and tertiary currents (i.e., the current distribution that mind diffusion, migration and convection of charged and uncharged species[238]), the system can be modelled with a computational fluid dynamics approach and described as a systems of differential equations and boundary conditions[239] that were extensively discussed by Kauffman[240] in 2020. Considering the electrolyte as an incompressible fluid, the hydrodynamics is governed by the conservation of mass and the conservation of momentum as reflected in the Navier–Stokes equations, Equations (19) and (20), with $\boldsymbol{u}$ representing the fluid velocity, P the fluid pressure, μ the dynamic viscosity, ρ the fluid density and $\boldsymbol{N}$ the resultant of the external forces acting on the fluid. The Navier–Stokes equations are usually solved by tested and robust algorithms such as SIMPLE[241], PISO[242] and PIMPLE[243].

$$\nabla \cdot \mathrm{u} = 0 \tag{19}$$

$$\frac{\delta u}{\delta t} + \nabla \cdot (\mathrm{u} \times \mathrm{u}) - \nabla \cdot (\mathrm{u}\nabla \mathrm{u}) = -\frac{1}{\rho}\nabla P + N \tag{20}$$

The electroneutrality of the electrolyte is fixed with Equation (20) and charge transport for the *i*th species is taken into account by the Nernst–Planck equation, Equation (21), with $\boldsymbol{J}$ representing ion flux within the fluid, D the diffusion coefficient of the species, $\mathrm{c_i}$ the concentration, n_i the valence electrons, R the ideal gas constant, F the Faraday constant, T the temperature and ϕ the electric potential.

$$\sum n_i c_i = 0 \tag{20}$$

$$J_i = -D_i \cdot \nabla C_i - \frac{D_i n_i F}{RT} C_i \cdot \nabla \phi + c_i \cdot u \tag{21}$$

The mass transport at both cathode and anode is considered in the Butler–Volmer equation, Equation (21) (i is the current density, i_0 is the exchange current density, C^{bulk} is the bulk concentration of the species in the fluid and $C(0, t)$ is the concentration at the electrode surface where the subscript indicates the species involved in oxidation (O) and in reduction (R); η is the overpotential and α and β are

respectively the symmetry anodic/cathodic barrier factors depending on the thermodynamic of the system[244].

$$\mathrm{i} = i_0 \left[\left(\frac{C_0(0,t)}{C_0^{bulk}} \right) e^{-\alpha n F \eta \frac{1}{T}} - \left(\frac{C_R(0,t)}{C_R^{bulk}} \right) e^{\beta n F \eta \frac{1}{T}} \right] \tag{21}$$

The thickness (τ) distribution onto the cathode is evaluated by imposing at the cathode Faraday's law for electrolysis (Equation (22)) as a boundary condition, considering t the deposition time; i the current at the electrode (evaluated with Equation (21)) and M_w and ρ_m the molecular mass and density, respectively.

$$\frac{\delta \tau}{\delta t} = \mathrm{i} \frac{M_w}{\rho_m n F} \tag{22}$$

In multiphysics simulations, the previously illustrated equations are solved according to the finite element method (FEM)[245], a numerical approach already extensively used in the engineering field to discretize continuous problems[246–248]. In FEM approach the input geometry (i.e., the electrochemical cell) is divided into finite elements, building a mesh. Differential equations are solved in the integral form, discretizing integrals in a summatory over finite elements where shape functions are defined[249]. Multiphysics simulations can be easily implemented in the industrial manufacturing workflow for example using the commercial software COMSOL 6.2[250], directly importing the CAD designs of decorative accessories. An example of modelling an industrial process of electroforming with it was proposed by Andreou[251] in 2022. The opensource alternative is represented by the OpenFOAM framework[252] : it allows complete personalization of the system but its use is not immediate as it requires programming and scripting knowledge. In 2020 Kauffman[240] proposed and tested an algorithm inside the OpenFOAM environment that successfully described the electrodeposition of copper, reproducing effectively the thickness distribution over a cuspidated cathode. In 2023, Huang[253], still in the OpenFOAM environment, made a whole framework for electrochemical processes and electrolyte flow capable of accounting for different species, including external forces over the electrolyte and the influence of a magnetic field on the electrodeposition process. Connecting designers, metalworking engineers and chemists through multiphysics simulations it will be possible to produce goods with sustainable geometries reducing drastically the waste of precious metals. Each of these three figures has a fundamental place in this challenge: designers have the task of creating new geometries and providing CAD models; engineers must validate the mechanical feasibility of geometries; chemists must perform simulations to find the optimal parameters for it, such as the exchange current, the symmetry factors and the deposition potential, and chemists also need to validate the results of simulations through experimental counterparts determining the thickness of deposited metals through non-destructive methods, such as X-ray fluorescence spectroscopy (XRF)[235]. The whole production process can be fully optimized only if all the data from these three figures of the fashion industry can be crossed and elaborated in order to obtain the better results. Hence, AI-based technologies[254] can be the key elaborate this multitude of correlated aspects.

Specifically, to help the artists to reimagine fashion items, a generative design [255,256] approach could take the full advantages of the thickness distributions obtained from multiphysics simulations and find an alternative geometry with the constrain minimize the current distribution. Additionally, this novel production scheme needs to be iterative, alternating multiphysics simulations with generative design, to achieve the lowest metal dispersion possible.

Deposition Systems

Obtaining homogeneous electrochemical deposits is an issue of absolute importance, especially in the field of the high-fashion industry, where precious metals are often used. Indeed, even a low percentage reduction in consumption leads to a great advantage for the overall process[171].

Having a low standard deviation in the metal deposit allows a smaller amount of material to be used, as the required minimum thickness values can be achieved with less dispersion in the obtained coating, thus operating with reduced costs and less operating time. This leads to clear advantages for the environment sustainability of the entire production process and for the competitiveness and profitability of the manufacturing company. The thickness of the deposits obtained from present electroplating production is uneven because it is strongly influenced by the shape of the treated objects and the current distribution[257,258].

In this work, a benchmark study was conducted on the systems adopted by companies to control the distribution of thicknesses in the case of a precious metal finishing, evaluating the effect of different state of the art industrial engineering solutions. The thickness distribution of gold deposition within the electroplating rack, obtained using the standard parallel anode configuration, was taken as the reference. It was compared with two devices operating on direct current (DC) designed to overcome thickness inhomogeneities and a system operating on pulsed current (PC). The depositions were performed in a typical electroplating tank **Figure 36**.

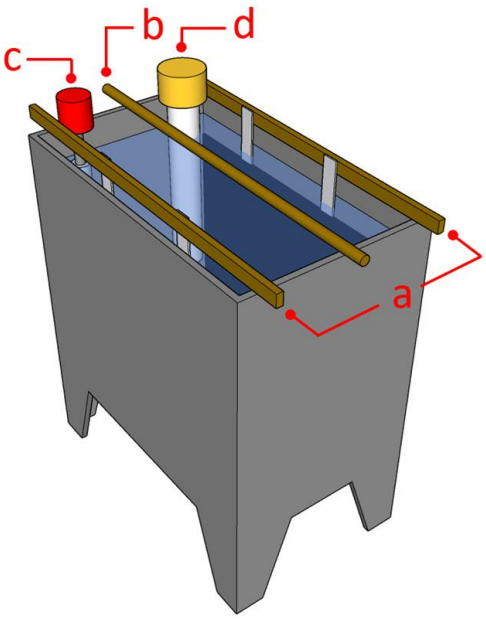

Figure 36 A 500 L electroplating tank containing (**a**) two anode bars, one for each side, to which the MMO anodes are connected; (**b**) a central cathodic bar, where the rack is attached; (**c**) a float to control the level and temperature of the solution; (**d**) a heating element for heating the solution.

All the samples were kindly electroplated and provided by Lotti Srl (Signa, FI, Italy), Gruppo Materia Firenze (Scandicci, FI, Italy) and Eco-Tech Finish Srl (Arezzo, AR, Italy), on their industrial production lines according to the internal standard production process.

DC Deposition Systems

The case study carried out on optimization systems operating on DC was performed on a gold deposit, electrodeposited by means of the commercial "Bluclad 8693" (Calenzano, FI, Italy) electroplating solution. The performance of a classical system operating with common mixed metal oxide (MMO) anodes was compared with that of the commercial systems Italfimet (Monte San Savino, AR, Italy) "Raddrizzatorre Anti Effetto Punta" (RAEP) and Luxury Brands Technologies (LBT) (Calenzano, FI, Italy) "Homogeneous Coating System" (HCS), designed to increase the homogeneity of deposited precious metal thicknesses. The thicknesses of each plate were evaluated by XRF analysis using the fundamental parameters approach[259]. XRF is a fundamental technique in electroplating facilities because it allows for non-destructive control of thickness and metal distribution with fast and robust measurements. This enables the adjustment of deposition parameters such as current density and time for DC, as well as T_{on} and T_{off} for PC. ED-XRF instruments are now standard in electroplating fashion companies, but their use in optimizing the production process is often limited by the operator's insufficient knowledge. The commercial software associated with the equipment often functions as a black box, creating the misconception that employees merely need to press a button. In reality, it is a complex technique that requires qualified personnel.

Italfimet RAEP aims for the maximum thickness uniformity of precious metal electroplating filling inside the working rack. The device is based on the supply of DC, distributed inside the electroplating tanks with the aim of minimizing the effect of the presence of areas with high and low current density within the electroplating system. This is achieved by pre-setting the direct current to be distributed in multiple zones within the system itself. In detail, the anodes consist of three anodic elements coated with mixed oxides, which have 3 different anode outputs. Anodes 1 and 3 are the outer ones and have a complementary shape to the inner anode 2 (**Figure 37a**). The system allows the current of the external anodes to be modulated in a range of instrumental settings from −999.9 to +100.0 (dimensionless values), in the upper section of the anode ("high-cut") and in the lower one ("low-cut") independently. Based on the authors' industrial experience, the current was distributed on the three anodes following Equation (23).

$$i_1 = \frac{i_{tot(h+1)}}{3+h+l};\ i_2 = \frac{i_{tot}}{3+h+l};\ i_3 = \frac{i_{tot(l+1)}}{3+h+l} \quad (23)$$

where i_1, i_2, i_3 are respectively the current applied to the upper, center and lower anodes and h and l are, respectively, the high-cut and the low-cut values. Moreover, $i_1 = 0$ if $h > -1$; $i_3 = 0$ if $l > -1$; $i_1 = i_2 = i_3 = 0$ if $h + l > -3$. In this work the default parameters provided by the supplier were chosen: high-cut of −10.0 and low-cut of −30.0. The manufacturing company of RAEP reports a saving on the cost of the deposition of an average precious metal estimated in the order of 10–15% in addition to a significant reduction in the duration of work cycles related to the deposition of precious metals. This system is applicable to every precious metal plating process on the market, and it is easily implementable within each electroplating tank[260].

LBT-HCS uses a current rectifier “High Performance System” (HPS), designed to distribute applied currents according to the different areas of the rack, to be used with a specific system of three anodes associated with three anode outputs (**Figure 37b**); the central anode has a convex pyramidal shape. The system makes it possible to reduce the differences in current density that can occur between the outer and internal parts of the rack. The current can be modulated for all three electrodes setting the percentages and delays for high, medium and low zones. LBT reports a case study carried out on a palladium electroplating formulation in which a reduction of about 11% in mass of metal deposited and a reduction in the standard deviation in measured thicknesses is observed on minimal thicknesses of 0.8 μm of deposit, evidence of increased homogeneity of the deposit[261]. To confirm the data reported by the suppliers of three-way anode systems, an empirical validation was carried out. In this work, the single rack settings given by the supplier were used: percentage high zone 35.0%, percentage medium zone 55.0%, percentage low zone 10.0%, 20 s delay in low area. Normalized distributions of electrodeposited gold thicknesses are reported in **Figure 38**.

a *b*

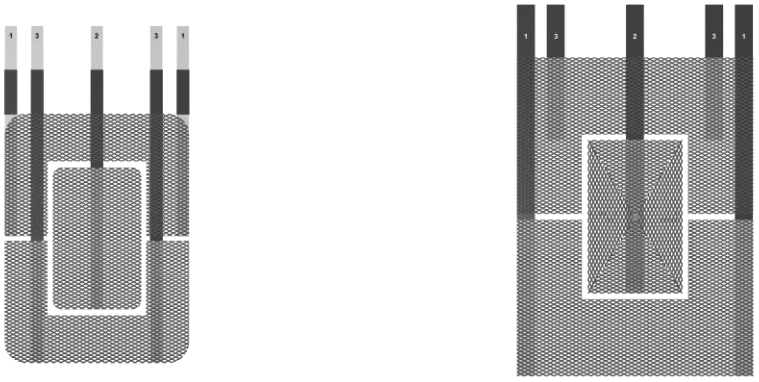

Figure 37 Anode schemes of (**a**) the Italfimet RAEP system, where 1 indicates the connectors related to the upper section of the three-anode system, 2 the connector related to the middle section and the connector related to the lower section; (**b**) the LBT HCS system, where 1 indicates the connectors related to the lower section of the three-anode system, 2 the connector related to the middle section and 3 the connector related to the upper section.

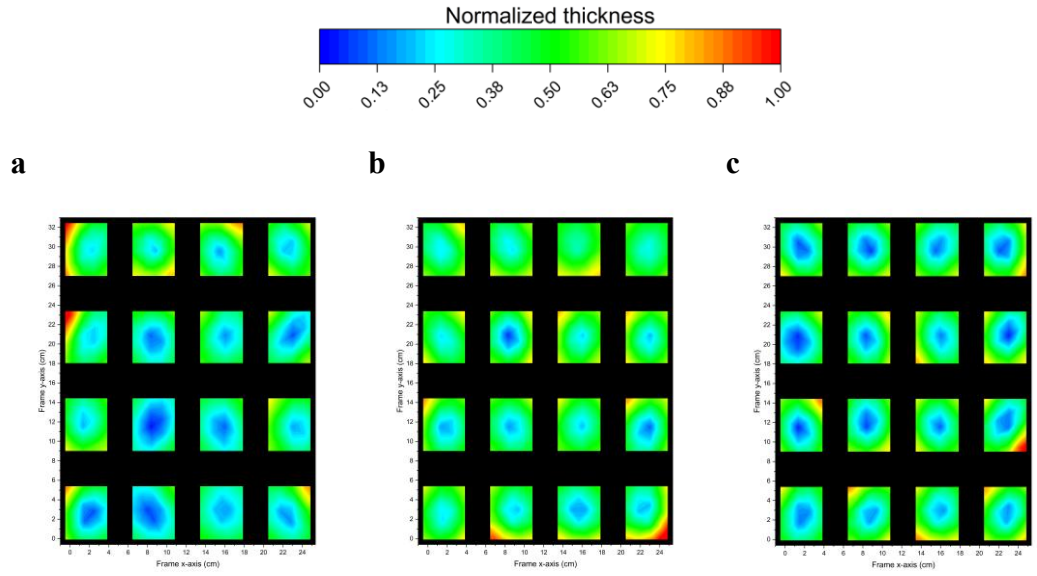

Figure 38 Normalized distributions of electrodeposited gold thicknesses, measured by XRF analysis, relative to a sample obtained (**a**) under standard conditions (DC1); (**b**) using the RAEP system; (**c**) using the HCS. The x and y axes represent the coordinates inside the plating rack, which contains 16 plates arranged in rows and columns of 4. Areas of the rack where there are no plates are shown in black.

As expected, in the center of each plate, there is an area of low deposited thickness; this problem is visibly mitigated in the case of the result obtained by employing the RAEP system. These results are confirmed by the standard deviation values obtained on the entire rack (**Table 10**): the RAEP system shows a significant reduction in the standard deviation value, both in terms of absolute and percentage values. The values obtained in the case of the HCS system are comparable to those obtained in standard conditions.

Table 10 Mean values, standard deviations, and standard deviations of the average thickness of each plate, related to XRF thickness measurements performed on the samples of the entire rack obtained under standard conditions and using the RAEP and HCS systems. The reported thickness errors are based on 80 independent measurements for the overall plating rack and on 5 independent measurements for each individual plate.

	Standard DC1	**RAEP**	**HCS**
Average thickness (µm)	0.57 ± 0.05	0.52 ± 0.05	0.53 ± 0.05
Std. Dev. (µm)	0.13	0.09	0.13
Std. Dev.%	23.75	18.23	25.46
Std. Dev. of averages of each plate (µm)	0.052	0.016	0.022
Std. Dev. of averages of each plate (µm)%	9.17	3.03	4.10

It is also possible to assess how the RAEP and HCS systems reduce the dispersion of thickness within each plate. Therefore, it can be stated that the RAEP system increases the homogeneity of the deposits throughout the entire rack, allowing to reduce the overall metal used to guarantee the minimum thicknesses required. The HCS system does not decrease the standard deviation relating to all thickness measurements, but reduces the difference observed between the various plates.
To further evaluate the performance of these systems, process capability analyses were carried out. A process capability study predicts whether a manufacturing process can repeatably produce parts that meet specifications. To make these assessments, the parameters C_p and C_{pk} were used[262]. C_p (Equation (24)) measures whether the process spread is narrower than the specification width, hence the potential capacity of the process. While C_{pk} (Equation (25)) measures both the centering of the process as well as the spread of the process relative to the specification width, hence actual capacity of the process.

$$C_p = \frac{USL - LSL}{6\sigma} \tag{24}$$

$$C_{pk} = \mathrm{Min}\left(\frac{USL - \overline{x}}{3\sigma}; \frac{\overline{x} - LSL}{3\sigma}\right) \tag{25}$$

where *USL* and *LSL* are respectively the customer-defined limits upper and lower process specification customer-defined limits (VOC) and σ is the standard deviation of the process, 0.55 μm was used as the *USL* and 0.45 μm as the *LSL*.
As shown in **Table 11**, The RAEP system improves the value of C_p over results obtained under standard conditions, while the HCS system returns results comparable to it.

Table 11 Evaluation of Cp and Cpk values on samples obtained under standard conditions and using the RAEP and HCS systems.

	Standard DC1	RAEP	HCS
Cp	0.12	0.18	0.12
Cpk	-0.044	0.110	0.054

The RAEP and HCS systems both allow the improvement of the parameter C_{pk} (the increase in these parameters is a positive result).

Pulsed Plating System
The same evaluations performed in the previous section were carried out on the thickness distribution comparing the deposition obtained by operating in DC and PC. To compare the results reported in the literature[263] with the outcomes shown by three-electrode DC anode systems, an empirical data validation was carried out. The study was performed on a gold deposit electrodeposited by means of the commercial "Bluclad 8614 MUP" electroplating solution.
Normalized distributions of electrodeposited gold thicknesses are reported in **Figure 39**. The use of pulsed current improves the overall homogeneity of the thickness of the deposits.

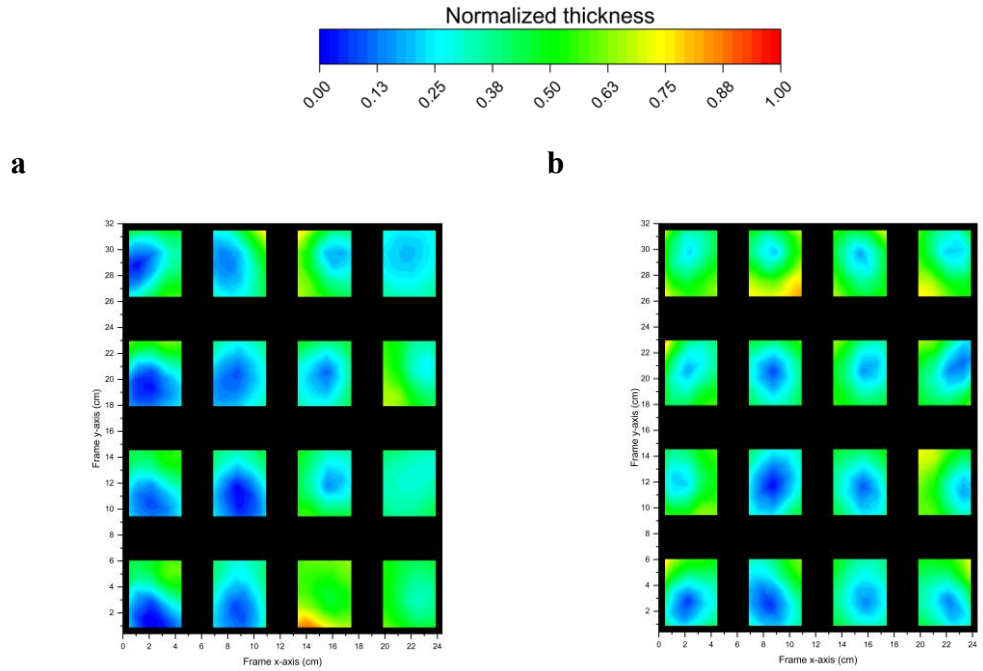

Figure 39 Normalized distributions of electrodeposited gold thicknesses, measured by XRF analysis, relative to a sample obtained (**a**) under standard DC conditions (DC2); (**b**) under PC deposition conditions. The x and y axes represent the coordinates inside the plating rack, which contains 16 plates arranged in rows and columns of 4. Areas of the rack where there are no plates are shown in black.

As can be assessed from the results shown in **Table 12**, the use of pulsed current reduces the percentage standard deviation.

Table 12 Mean values and standard deviations of the average thickness of each plate, related to XRF thickness measurements performed on the samples of the entire rack obtained under direct current conditions and under pulsed current conditions. The reported thickness errors are based on 80 independent measurements for the overall plating rack and on 5 independent measurements for each individual plate.

	Standard DC2	**PC**
Average (µm)	0.49 ± 0.05	0.52 ± 0.05
Std. Dev. (µm)	0.15	0.15
Std. Dev. %	31.66	29.81
Std. Dev. of the averages of each plate (µm)	0.080	0.091
Std. Dev. of the averages of each plate (µm)%	16.36	17.67

It can be stated that the PC system slightly increases the homogeneity of the deposits throughout the entire rack, making it possible to reduce the overall metal used to guarantee the minimum thicknesses required.
On the other hand, it can be seen how operating with pulsed current in these conditions slightly increases the standard deviation of the average thickness of each plate.
An evaluation of the parameters C_p and C_{pk} was also carried out; the results are shown in **Table 13**.

Table 13 Evaluation of Cp and Cpk values made on samples obtained under direct current conditions and under pulsed current conditions.

	Standard DC2	**PC**
Cp	0.11	0.11
Cpk	0.080	0.075

While the value of C_p shows no appreciable changes in the case of PC in comparison to DC, the value of C_{pk} worsens, meaning that the PC process still has room for improvement.
C_p and C_{pk} results, even with improved operating conditions using RAEP, HCS and PC systems, are still suboptimal. Values of C_p and C_{pk} equal to 2 should be considered optimal, while values of 1 are considered barely acceptable[262]. The distance between optimal values of capability estimators, and the results obtained on in-line production processes can be explained by the fact that customers specifications are arbitrary, especially for the high fashion market. Clients only indicate a minimum thickness,

not considering the distribution of it and the geometry of the artifact. In the field of high fashion accessories, brands often do not specify the measurement spot causing the approval of the quality control step to be highly influenced by the arbitrariness of the operator. Hence, analytical estimators such as C_p and C_{pk}, fail to represent the correctness of a process that lacks a profound structuring of demand.
This testifies that the field of electroplating in the high fashion industry shows ample room for improvement, both from an electrochemical engineering point of view and on the demand side and management of the production process: in the first case working on both anode geometries and current waveforms, and in the second case working on correctly disclosing the issues and physical chemistry behind electrodeposition to line workers. To effectively integrate the characteristics of pulsed current depositions with three-way rectifiers, several enhancements are necessary for electroplating factories. Firstly, the hardware must be optimized to utilize both features synergistically. Additionally, a specific formulation of the electroplating bath needs to be developed. Proper training for the personnel in the electroplating department is also crucial. Achieving these improvements is financially challenging for many local electroplating industries, which are often small to medium-sized companies.

Corrosion Tests

In the literature, there are numerous tests to ensure quality control and to verify the performances of the coatings[171,185]. Among them, neutral salt spray has been chosen to be a benchmark of the systems discussed in this review.
The 4 samples along the diagonal of the electroplating rack were selected, the purpose of this sampling is to evaluate the effects of corrosion as the position in the rack changes and to correlate the results obtained with those achieved in the previous paragraphs. The samples were tested against neutral salt spray (NSS) test ISO 9227 for 48 h. During this time, the corrosion behavior of the different coatings was monitored by visual investigation. The samples were visually evaluated by reporting the results with values in the range of 1 to 5, where 5 means no variation occurred on the surface of the sample; 4 slight variation; 3 visible variation; 2 evident variation; and 1 considerable variation. This evaluation metric is adopted by major analysis companies in the field of metal accessories of luxury brands[171]. Standard DC1 samples (obtained in the standard conditions using “Bluclad 8693” electroplating solution) showed a 4.3 average result, RAEP samples 4.5, HCS samples 3, Standard DC2 samples (obtained in the standard conditions using “Bluclad 8614 MUP” electroplating solution) 1.5 and pulsed current samples 2.8.
The results obtained using the RAEP show an improvement over the ones obtained operating under the standard conditions; on the other hand, the use of the HCS system led to a worsening of the performances. However, it is important to note that the outcomes obtained using the latter operating conditions resulted in more homogeneous outputs, this agrees with the results obtained during the evaluation of thicknesses. Depositions using pulsed current resulted in a marked increase in corrosion resistance performance.

Given the results observed in the previous paragraph, which indicated that the PC system slightly increases the homogeneity of the deposits throughout the entire rack, it can be hypothesized that such a marked change in corrosion resistance with respect to a slightly different homogeneity is due to other factors that come into play using pulsed current, such as a change in the chemical–physical structure of the deposit compared with that obtained under direct current conditions. As reported in the literature the use of pulsed current can lead to changes in the morphology of the structure of the deposit[188]. This result is very interesting because it highlights the possibility of obtaining deposits that exhibit greater corrosion resistance for the same amount of precious metal used, with clear advantages both economically and environmentally.

Recovery of Metals

The exponential growth of the world's population and the limitation of natural resources are presenting new challenges. Pollution prevention, waste minimization and the recycling of end-of-life (EOL) products have become primary topics of interest[264,265]. Sustainable development involves creating materials and products that can be more easily recycled through proper management. In terms of sustainability, recycling activities aim to maximize reuse, minimize energy consumption, reduce costs and waste and ideally achieve upcycling. The rapid pace of industrialization is increasing the demand for precious metals, while high-quality natural resources are dwindling, causing operating costs to skyrocket. Consequently, there is a growing need for education on the recovery of these metals.

Due to industrialization, the amount of solid and liquid waste generated from various technological processes and consumer goods is rising, particularly in developing countries. This waste can be either organic or inorganic. Inorganic waste contains toxic metallic and non-metallic elements that have severe negative impacts on ecosystems. Some of these non-ferrous metals have a moderate deterioration rate, persisting for extended periods and exerting cumulative toxic effects. Additionally, many of these elements are carcinogenic[264].

The most significant solid waste materials include non-ferrous metals such as copper, nickel, zinc, chromium, molybdenum and gold, among other potential heavy metals. Heavy metals are elements with atomic weights between 63.5 and 200.6 and a density greater than 5 g/cm^3. They are characterized by high stability and low biodegradability[266,267], leading to bioaccumulation and biomagnification in living organisms[268].

Many elements fall into this category, but the ones listed in **Table 14** are particularly relevant in the environmental context[269]. Heavy metals cause serious health effects, including reduced growth and development, organ and nervous system damage, cancer and in extreme cases, death. The maximum contaminant level (MCL) standards, for those heavy metals, established by United State Environmental Protection Agency (USEPA)[270] are summarized in **Table 14**.

Table 14 MCL standards for the most hazardous heavy metals.

Heavy metal	Toxicities	MCL (mg/L)
Arsenic	Skin manifestations, visceral cancers, vascular disease	0.05
Cadmium	Kidney damage, renal disorder, human carcinogen	0.01
Chromium	Headache, diarrhea, nausea, vomiting, carcinogenic	0.05
Copper	Liver damage, Wilson disease, insomnia	0.25
Nickel	Dermatitis, nausea, chronic asthma, coughing, human carcinogen	0.20
Zinc	Depression, lethargy, signs and increased neurological thirst	0.80
Lead	Damage the fetal brain, diseases of the kidney, circulatory and nervous systems	0.006
Mercury	Rheumatoid arthritis, diseases of the kidneys, circulatory and nervous systems	0.00003

Overall, 75% of copper metal today is used in the electronics, communication and energy sectors[271], all areas from which the ecological transition will pass. Copper also performs essential work in animal metabolism, but the excessive ingestion of copper brings about serious toxicological concerns, such as vomiting, cramps, convulsions, or even death[272].

Zinc is a trace element essential for human health, playing a crucial role in the physiological functions of living tissue and regulating many biochemical processes. However, excessive zinc intake can lead to significant health issues, including stomach cramps, skin irritations, vomiting, nausea and anemia[273]. About 50% of the metallic zinc produced globally is used for anti-corrosion coatings on steel; 30% is used for alloys, primarily brass; and the remainder is utilized in chemicals, pigments, coinage and other minor applications[274].

Approximately 65% of the nickel consumed in the Western world is used to manufacture austenitic stainless steel, while 12% is used in superalloys. The remaining 23% is distributed among various applications, including other types of steel, rechargeable batteries, catalysts and other chemicals, coinage, foundry products and plating (9%)[275]. Exceeding critical levels of nickel can cause serious health issues such as lung and kidney problems, gastrointestinal distress, pulmonary fibrosis and skin dermatitis[276]. Nickel is also recognized as a human carcinogen[267].

Gold, although not cautioned by the EPA in terms of maximum contaminant concentration, it can be detrimental for human health. Gold is often used to treat certain diseases, such as rheumatoid arthritis and bronchial asthma; however, it shows very harmful side effects, including pulmonary toxicity, skin rash, peripheral eosinophilia and liver dysfunction[277]. Seven percent of the gold mined each year is used for medical, industrial and technological purposes, while the remaining 93% is utilized in the jewelry industry and banking, such as in the production of bars and coins[278].

The largest industrial consumption of chromium is in the protective and decorative coating of metal artifacts and in the preparation of various alloys. Oxides and chromates are used as pigments while high salts are used in the textile and tanning industries. Chromium exists in the aquatic environment primarily in two states: Cr(III) and Cr(VI). Generally, Cr(VI) is more toxic than Cr(III). Cr(VI) impacts human physiology, accumulates in the food chain and causes severe health problems, ranging from simple skin irritation to lung carcinoma[279].

The mining industry is one of the main causes of pollution on the planet: the smelting of metals, including gold, contributes about 19 million tons of sulfur dioxide (about 13 percent of global emissions) into the atmosphere each year, causing acid rain[280]. The mining, processing and refining of precious metals requires a great deal of energy: suffice it to say that 7–10% of the oil, gas, coal and hydropower produced annually worldwide (not counting the energy used in transportation) is used in these industries. Mines also generate an immense amount of waste: in 2010, 900 million tons of metal were extracted, producing 6 billion tons of waste, most of which originated from the mining of gold, iron and copper[281].

Many countries have enacted, in the past decade, regulatory laws regarding waste management[264]; one such regulation, effective from 2020, mandates the reuse and recycling of at least 50 percent by weight of paper, metal, plastic and glass from household garbage. Unlike simple storage, these new processing methods enable the recovery of materials embedded in solid residues containing precious metals. The production of these metals from primary sources is constrained and involves high energy consumption. Therefore, recycling can significantly contribute to energy savings and the reduction of CO_2 emissions[282].

Precious metals are crucial in modern society, closely tied to technological advancements and daily life. Sustainable development and stricter environmental legislation are encouraging the recovery of precious metals as a viable approach to conserving natural resources and minimizing waste without incurring high costs.

An explanatory example is the case of gold: for every gram of usable gold, about 1 ton of debris is produced in the mining process[283]. In addition, water contaminated with cyanides and mercury[284] is released, and other chemicals are released into the atmosphere (such as sulfur dioxide and carbon dioxide from metal smelting[285]). A provocatory report of Fairtrade Labelling Organization (a non-profit organization specialized in issuing fair and sustainable trade certifications) states that for one gold wedding ring alone, 3 tons of waste is produced and between 50 and 150 g of mercury is used[286]. Mercury, widely employed in artisanal and small-scale gold mining (ASGM)[287–289], is used because of its ability to combine with gold, allowing the separation of the precious from other minerals. The resulting product, called amalgam, is then heated to a temperature above 257 °C to vaporize the mercury it contains[289]. The use of mercury has a significant impact on the environment and on people: it has the characteristic of not biodegrading and therefore precipitating, settling on the land and consequently on agricultural products, as well as on water and therefore in fish. From there, it is transferred to humans; these areas have a higher incidence of cancer. A gold rush causes the illegal appropriation (i.e., without the

consent of the population) of entire territories and the depletion and contamination of primary resources.
A step towards a society marked by sustainability, not only economically but also socially and environmentally, is perpetrated by the previously mentioned Fairtrade Labelling Organization, the one of the most recognized sustainability label[290]. Even gold can be certified as ethical gold[291]. In fact, ethical gold is mined legally, in mines that have been granted the rights to mine on the ground and in which local communities themselves are primarily employed[292]. It is also mined with greater attention to both people's safety and environmental pollution, minimizing the use of mercury and using it in closed cycles to avoid its release into the environment.
The protection of local communities, who are guaranteed minimum wages and adequate working conditions, providing jobs for women as well, fully embrace the ethics of Sustainable Development as promoted by the United Nations in points 1 (No poverty), 3 (Good health and well-being), 5 (Gender equality), 8 (Decent work and economic growth), 10 (Reduced inequalities). Environmental protection through low-impact extraction methods instead reflects goals 12 (Responsible consumption and production), 13 (Climate action), 15 (Life on land). Another fundamental certification in the fashion industry is the RJC-CoC (Responsible Jewelry Council–Chain of Custody)[293] form the Responsible Jewelry Council, a non-profit organization devoted to setting sustainability standards for the jewelry industry; such certification ensures full traceability of the production chain and guarantees responsible sourcing.
According to Stephen Lezak, an Oxford University researcher and expert in economics and the environment, gold mining could be halted immediately without causing a shortage in any of the above sectors, simply by recycling it[283]. According to the economic models proposed in the research, the only impact would be on the price of gold itself, which today serves both as a safe haven asset for investors and as a "stabilizer" and financial reference for several countries. On the other hand, as far as pollution is concerned, it is estimated that if the supply of gold were derived simply from recycling there would be a decrease in air emissions and impact on ecosystems by 99%; the remaining 1% would represent pollution from the transportation and processing of the precious metal in the recycling stage.
Optimizing recovery solutions presents new avenues in research, addressing increasing demand, resource depletion and global development needs. Precious metals recovered through these processes retain their properties across multiple life cycles, enabling recycling to achieve the following:

- Recover valuable materials without loss of quality;
- Save energy compared to primary production;
- Decrease the need for mining activities;
- Minimize waste.

Industrialized nations have embraced proactive environmental policies aimed at mitigating technological risks, demonstrating significant adaptability through a culture of innovation and the adoption of long-term strategies. Discovering novel technologies for recovering precious metals can harmonize economic pressures with the imperative to preserve natural ecosystems, thereby potentially yielding a positive

global impact. These goals align with the objectives of Sustainable Development Goals (SDGs) 9 (industry, innovation, and infrastructure), 11 (sustainable cities and communities) and 12.

The electroplating industry is considered highly hazardous among chemical-intensive industries due to its significant discharge of metal-contaminated wastewater[294].

In typical electroplating industries, a substantial volume of wastewater is produced from rinsing electroplated parts[295,296] amounting to approximately 20% of the chemicals used in metal salts plating baths[297]. This wastewater contains elevated levels of metal ions that surpass the Industrial Effluent Guidelines set by the USEPA, necessitating treatment to mitigate its high toxicity before discharge into the environment[298]. Therefore, treating metal-contaminated wastewater prior to discharge into the environment is essential[294].

However, in certain electroplating industries, particularly those involving precious metals such as silver, palladium and gold, the wastewater contains significant amounts of these valuable metals. Therefore, an appropriate wastewater treatment process is necessary not only to remove heavy metals but also to recover these precious and valuable metals, addressing both economic growth and environmental considerations[296].

Various treatment techniques for heavy-metal-laden wastewater have been developed in recent years to reduce wastewater volume and enhance the quality of treated effluent. Methods such as electrowinning[299], chemical precipitation, coagulation–flocculation, flotation, ion exchange and membrane filtration are available for removing heavy metals from contaminated wastewater. Each method has its specific advantages and limitations in practical application[300].

Sophisticated electrochemical treatments such as electrodialysis[301], membrane electrolysis[302] and electrochemical precipitation[303] have also played a role in environmental protection. However, these techniques have been less extensively studied due to their high operational costs associated with energy consumption.

Chemical precipitation is a commonly employed method for removing heavy metals from inorganic effluent[304]. By adjusting the pH to basic conditions (pH 11), dissolved metal ions undergo a chemical reaction with a precipitant agent such as lime, converting them into an insoluble solid phase[305]. Typically, the precipitated metal from the solution takes the form of hydroxide. The theoretical process of heavy metal removal via chemical precipitation is illustrated in Equation (26)[305]:

$$M^{2+} + 2(OH)^{-} \rightleftharpoons M(OH)_2 \downarrow \quad (26)$$

where M^{2+} and OH^{-} represent the dissolved metal ions and the precipitant, respectively, while $M(OH)_2$ is the insoluble metal hydroxide. The metal precipitates formed are separated through processes such as coagulation, sedimentation or filtration and then purified using chemical extraction methods[269]. Lime precipitation has been utilized to remove heavy metal cations such as Zn(II), Cd(II) and Mn(II) with an efficiency of 99%. Removal efficiencies for ions such as Cu(II) and Ni(II) are approximately 80% and 85%, respectively. Advantages in the use of precipitation

relate especially to the simplicity of the process and the use of inexpensive equipment. Despite its advantages, chemical precipitation requires a large amount of chemicals to reduce metals and drawbacks such as slow precipitation of metals, poor sedimentation, aggregation of precipitates and especially excessive sludge production. These, in fact require further treatment before disposal, which has a high cost and environmental impact.

Coagulation–flocculation is effective for treating inorganic effluent with metal concentrations ranging from less than 100 mg/L to over 1000 mg/L. In this process, colloidal particles are destabilized by adding a coagulant, leading to sedimentation[306]. After coagulation, the process of flocculation follows to further increase the particle size, forming bulky floccules from the initially destabilized particles. This technique is mainly used for the treatment of Cu(II), Zn(II), Cd(II), Mn(II), which are removed with an efficiency of 99%[294]. Within an electroplating industry, this system is mainly adopted within chemical and physical wastewater treatment systems containing mainly cyanide and chromic washes (after preliminary decyanidation and dechromatization processes). The major advantages of lime-based coagulation reportedly include enhanced sludge settling, improved dewatering characteristics, bacterial inactivation capability and increased sludge stability[307]. Despite its advantages, coagulation–flocculation has limitations such as high operational costs due to chemical consumption.

Flotation is utilized to separate solids or dispersed liquids from a liquid phase using bubble attachment[294]. Attached particles are then separated from the heavy metal suspension as bubbles rise. Flotation methods include dispersed-air flotation, dissolved-air flotation (DAF), vacuum air flotation, electro-flotation and biological flotation. Among these, DAF is the most widely employed for treating metal-contaminated wastewater. Adsorptive bubble separation utilizes foaming to separate metal impurities. While it is primarily a physical separation process, flotation for heavy metal removal shows potential for industrial applications. Additional benefits include enhanced removal of small particles, shorter hydraulic retention times and cost-effectiveness, making flotation a highly promising option for treating metal-contaminated wastewater[308]; towards Cu(II) and Ni(II) ions there is a removal efficiency of 98%, while with regard to Cr(VI) the efficiency is between 95% and 98%.

Membrane filtration has garnered significant interest for treating inorganic effluent because it can eliminate suspended solids, organic compounds and inorganic contaminants such as heavy metals. Depending on the particle size that needs to be retained, different types of membrane filtration, such as ultrafiltration, nanofiltration and reverse osmosis, are utilized for heavy metal removal, as detailed below. Membrane filtration is among the most used techniques, in the galvanic field, within concentration systems. Concentration systems means all those technologies adopted for the treatment and purification of water that lead to the recovery and/or reduction of wastewater. Another technique, although less widely used in surface treatment, is electrodialysis (presented later).

Ultrafiltration (UF) utilizes permeable membranes to separate heavy metals, macromolecules and suspended solids from solutions containing inorganic

compounds based on the pore size (5–20 nm) and the molecular weight (1000–100,000 Da)[269,294,309]. Depending on the membrane's characteristics, UF can achieve removal efficiencies exceeding 90% for metals with concentrations ranging from 10 to 112 mg/L.; this applies both to copper, nickel and cobalt, whose removal efficiency is 100%, but is also used for Cr(III) with a rejection rate of 95%.

Nanofiltration (NF) bridges properties of both UF and RO membranes, utilizing steric (sieving) and electrical (Donnan) effects in its separation mechanism. This membrane is notable for its small pore size and surface charge, enabling the rejection of charged solutes smaller than the membrane pores along with larger neutral solutes and salts. Typically, NF membranes can effectively treat inorganic effluent containing metal concentrations up to 2000 mg/L. Notably, they demonstrate a significant 95% retention rate for Ni(II) ions.

Reverse osmosis (RO) is a pressure-driven membrane process where water permeates through the membrane while heavy metals are retained. RO technology has evolved to accommodate increasingly stringent environmental regulations, utilizing membranes with pore sizes as small as 10–4 μm [148]. Generally, RO is more effective than UF and NF for removing heavy metals from inorganic solutions, achieving removal rates exceeding 97% for metal concentrations ranging from 21 to 200 mg/L. Also in this case cations with a greater rejection rate are Cu(II) and Ni(II) [310].

Ion exchange is also widely used globally for treating heavy-metal-laden wastewater. In ion exchange, there is a reversible exchange of ions between the solid and liquid phases. Here, an insoluble resin removes ions from an electrolytic solution and releases ions of similar charge in an equivalent amount, all without any structural alteration of the resin[309]. Ion exchange is also employed for the recovery of valuable heavy metals from inorganic effluent[311]. Once the loaded resin has separated the metals, they can be recovered in a more concentrated form through elution using appropriate reagents. In the electroplating industry, resin systems are widely used, mainly for the recovery of washing water. These equipment therefore allows for a reduction in the amount of water to be discharged and purified, thus ridiculing the size of purification plants. The greatest response occurs with Cr(III) and Cr(VI); in fact, in both cases, the cations are removed with a rate of 90–100%. Before employing ion exchange, it is essential to implement adequate pretreatment systems for secondary effluent, including the removal of suspended solids from wastewater. Furthermore, not all heavy metals have suitable ion exchange resins available, and the associated capital and operational costs can be substantial.

Adsorption has emerged as a viable alternative treatment method for heavy-metal-laden wastewater. Adsorption is a surface process where the concentration of a specific component (referred to as the adsorbate) in a gas or liquid stream increases at the surface or interface of a porous solid (known as the adsorbent). Depending on the forces brought into play, there are two types of adsorptions: chemical adsorption and physical adsorption[294]. The types of adsorbents widely used for PM recovery from wastewater are activated carbon[312] and carbon nanotubes[267], but also low-cost adsorbents such as agricultural and industrial wastes[313]. Because of its extensive surface area, high absorbency and surface reactivity, activated carbon is effective for

removing metals such as Ni(II), Cr(VI), Cd(II), Cu(II) and Zn(II) from inorganic effluent. The advantages of adsorption methods include straightforward operating conditions and the affordability of adsorbent materials. However, these methods are disadvantaged by low selectivity, low recovery efficiency and the generation of waste products.

Electrowinning is an electrolysis-based method where the metal cations present in wastewater are reduced on a cathode inside the solution[314]. This methodology due its simplicity is the most common metal-recovery technique in industrial electroplating plants working in the decorative field. A commercial set-up is usually made by two parallel MMO anodes with, between them, a copper mesh that serves as cathode. The main advantage of the method is the simplicity and the low installation costs, while it has deficiency in recover metals from low concentrated wastewater which can be overcome if coupled with techniques such as electrodialysis[301]. Electrowinning is often representing the first metal recover procedure as the apparatus is usually placed in the rinsing tank that follows the electroplating one.

Electrodialysis (ED) is a membrane-based separation process where ionized species in a solution are transported through ion exchange membranes under an electric potential[269]. These membranes are thin plastic sheets with either anionic or cationic properties. As the solution containing ionic species flows through the cell compartments, anions migrate towards the anode and cations towards the cathode, crossing the anion-exchange and cation-exchange membranes[315]. This method can recover valuable metals such as Cr and Ni with efficiencies of 90% and 99%, respectively.

Membrane electrolysis (ME) is another method used to eliminate metallic impurities from metal finishing wastewater. This is a chemical process activated by an electrolytic potential and this technique employs two types of cathodes: a standard metal cathode (electrowinning) and a high-surface-area cathode[302]. When an electrical potential is applied across an ion exchange membrane, redox reactions occur at the electrodes. In the anode, oxidation reactions occur as follows:

M and n represent the metal and the coefficient of the reaction component, respectively. The n coefficient depends on the state oxidation of the metal ions. This technique finds widespread acceptance in all galvanic industries, where it is used for the treatment of wastewater produced with rinse water. The metals most involved in the treatment are certainly precious metals, such as palladium and gold, but copper and nickel are also included. Different from ED, ME can be used to treat electroplating wastewater with a metal concentration less than 10 mg/L or more than 2000 mg/L. The major drawback of membrane electrolysis is its high energy consumption[294].

Electrochemical precipitation (EP) is utilized to enhance the removal of heavy metals from polluted wastewater, often replacing traditional chemical precipitation methods. Studies employing EP have focused on removing Cr(VI) from actual electroplating effluents[294]. Generally, electrochemical precipitation processes can effectively treat inorganic effluent containing metal concentrations exceeding 2000 mg/L. Depending on electrode characteristics, the electrochemical process can operate under acidic or basic conditions[316]. Heavy metal removal is achieved through

electrochemical oxidation/reduction reactions within an electrochemical cell, eliminating the need for continuous addition of redox chemicals and thereby reducing space, time and energy consumption costs.

Photocatalysis using semiconductors in aqueous suspension has garnered significant attention in the last decade, particularly for solar energy conversion[269]. This process facilitates the rapid and efficient degradation of environmental pollutants. When the semiconductor–electrolyte interface is illuminated with light energy exceeding the semiconductor's band gap, electron–hole pairs (e^-/h^+) form in the conduction and valence bands of the semiconductor, respectively[317]. These charge carriers migrate to the semiconductor surface, where they can oxidize or reduce species in the solution with suitable redox potentials. Various semiconductors such as TiO_2, ZnO, CeO_2, CdS and ZnS have been employed for this purpose.

Several studies were reported for the photocatalytic reduction of Cr(VI) and the degradation, using UV-irradiated TiO_2, of the complex cyanide with concurrent removal of copper[318].

Generally, physical, chemical treatments offer several advantages, including rapid processing, ease of operation and control and the flexibility to adjust to variable conditions such as seasonal flows and complex discharge patterns. Unlike biological systems, physical, chemical treatments can accommodate fluctuating input loads and flow rates. Chemical plants can be modified as needed, and the treatment systems require less space and lower installation costs. However, these benefits are counterbalanced by drawbacks such as high operational costs due to chemical usage, energy consumption and expenses associated with sludge disposal. Nevertheless, with advances in reducing chemical costs through the use of low-cost adsorbents and improving sludge disposal methods, physical–chemical treatments have emerged as among the most suitable options for treating inorganic effluent[269].

Electrochemical techniques for treating heavy metal wastewater are recognized for their rapidity and precise control, requiring minimal chemical inputs, yielding substantial reductions and generating less sludge. However, their widespread adoption is hindered by significant initial capital investment and the expense of electricity supply, limiting their further development[267]. **Table 15** summarizes the main advantages and disadvantages of the various treatments for electroplating wastewater.

Table 15 Different treatment techniques for wastewater and their advantages and disadvantages.

Type of treatment	Advantages	Disadvantages
Chemical precipitation	Low capital cost, simple operation	Sludge generation, extra operational cost for sludge disposal
Coagulation–flocculation	Shorter time to settle out suspended solids, improved sludge settling	Sludge production, extra operational cost for sludge disposal
Dissolved air flotation	Low cost, shorter hydraulic retention time	Subsequent treatments are required to improve the removal efficiency of heavy metal
Ultrafiltration	Smaller space requirement	High operational cost, susceptibility to membrane fouling
Nanofiltration	Low pressure than RO (7-30 bar)	Costly, prone to membrane fouling
Reverse osmosis	High rejection rate, able to withstand high temperature	High energy consumption due to high pressure required (20–100 bar), susceptible to membrane fouling
Ion exchange	No sludge generation, less time consuming	Not all ion resins are suitable for metal removal, high capital cost
Adsorption	Low-cost, easy operating conditions, having wide pH range, high metal binding capacities	Low selectivity, production of waste products
Electrodialysis	High separation selectivity	High separation operational cost due to membrane fouling and energy consumption
Electrowinning	Low installation cost, simplicity	Need of moderately concentrated metal cation solutions
Membrane electrolysis	Use over a wide range of metal concentrations	High energy consumption
Electrochemical precipitation	Fewer chemicals, acidic or basic conditions	Sludge production
Photocatalysis	Removal of metals and organic pollutant simultaneously, less harmful by-products	Slow process, limited applications

None of the treatments discussed has proven universally effective or applicable for removing heavy metals. As future regulations increasingly emphasize industrial compliance with legal limits on residual metal concentrations in discharge, there is significant value in exploring diverse treatment methods that can aid industrial users in meeting environmental requirements. While numerous methods exist for treating heavy-metal-laden wastewater, it is crucial to emphasize that choosing the most appropriate treatment depends on several factors. These include the initial metal concentration, overall treatment effectiveness compared to alternative technologies, plant flexibility and reliability, environmental impact and economic considerations such as capital investment and operational costs, including energy consumption and maintenance.

Ultimately, the selection of the most suitable treatment system for inorganic effluent, particularly within the electroplating industry, hinges on technical feasibility, operational simplicity and cost-effectiveness. This is particularly crucial given the diverse and metal-rich nature of electroplating wastewater. In this case, the use of only one recovery technique will never be satisfactory, but there is a need for several treatment steps working in synergy with each other to break down all harmful pollutants to a greater extent. All the factors mentioned above should be taken into consideration when choosing the most efficient and cost-effective treatment method to safeguard the environment. It is important to underline how electroplating companies, especially in the decorative field, have to understand the importance not only of installing commonly used metal-recovery methods (*e.g.*, electrowinning), but also optimize them within the necessity of each specific company and invest in research and development to study if other methods (as the one listed in this chapter) could better fit the needs and if the combination different techniques could lead to improved results, developing internal recovery protocols.

7.3 Conclusions

For over two decades, sustainability in the plating industry has been one of the key concerns of that industry. This makes it critical for the industry to assess the overall sustainability of virtually all plating facilities and then develop both short-term and long-term approaches for improving sustainability performance. In this thesis, three different but complementary lines of action to improve the sustainability of the electroplating industry were discussed, with reference to the Agenda 2030 SDGs, especially in non-mandatory fields such as the decorative one. Different plating techniques, in silico simulations and the metal recovery are linked to each other in minimizing material usage and, consequently, metal extraction. The principal SDGs addressed by all of them are the SDG 8 (decent work and economic growth), SDG 10 (reduce inequalities), SDG 12 (responsible consumption and production) and SDG 13 (climate action). In silico simulations streamline the trial-and-error phase, significantly reducing waste and enhancing business productivity. Optimized electroplating techniques enable the creation of more uniform deposits using less precious metal, which not only meets the stringent standards of major brands but also diminishes metal usage and boosts the competitiveness of companies investing in R&D. Enhanced metal recovery processes within businesses lower waste and operational costs, making products more affordable for less affluent populations. Efficient use of metals lessens the need for mining, often conducted in developing countries where it can cause substantial environmental and social harm. Mitigating these impacts improves local communities' livelihoods, fostering greater equity. By minimizing precious metal waste, companies directly contribute to reducing overall waste generation. This efficient metal use decreases the need for new resource extraction, leading to more sustainable production practices. Enhanced production efficiency means that fewer resources are required to achieve the same output, often resulting in lower energy consumption and reduced greenhouse gas emissions. Reducing precious metal waste also cuts emissions associated with the extraction, refining and processing of these materials, further supporting emission reduction efforts. Improved production efficiency and waste minimization bolster company resilience against the economic impacts of climate change, such as resource price volatility and stricter emissions regulations. Investing in waste reduction and efficiency technologies can spur innovative solutions applicable across various sectors, thereby contributing to broader climate change mitigation efforts. Despite that, to reach good sustainability standards, there is a great deal of work remaining. In addition to investing in process management efficiency improvements, it is fundamental that fashion designers take care of the whole production process, thinking outside the existing schemes to develop new sustainable geometries, and that industries embrace simulations to test them. Hence, deposition techniques should be improved by trying to combine the characteristics of pulsed current depositions with three-way rectifier engineering and calibrate the deposition parameters with analytical techniques such as spectroscopy. Furthermore, electroplating facilities need to dedicate labor to select and optimize recovery methods according to their specific internal needs. Finally, it was demonstrated how, in order to reach the sustainability goals, it is fundamental to invest in research and

development divisions, valorize qualified personnel and promote technological-transfer collaboration with universities and research institutes.

8 Final Remarks

The research presented in this thesis has demonstrated the remarkable versatility of electrodeposition and surface modification processes as key tools for both technological innovation and industrial sustainability. Throughout this work, electrochemical synthesis has been shown to offer not only a controllable and scalable approach to material fabrication but also a bridge between fundamental research and practical implementation. When properly designed and optimized, electrodeposition emerges as a powerful and environmentally compatible route to produce advanced functional materials and coatings for applications spanning spintronics, energy conversion, catalysis, and sustainable electroplating.

The thesis began with an in-depth investigation of the fundamental electrochemical techniques underpinning all subsequent studies. Methods such as cyclic voltammetry, chronoamperometry, and a suite of advanced characterization techniques, including SEM, XPS, and XRD, were systematically applied to correlate deposition parameters with the resulting structural, compositional, and properties of the materials. This methodological foundation enabled the establishment of a consistent framework for understanding the relationships between electrochemical behavior, film morphology, and functional performance.

In the third chapter, the successful electrodeposition of MnAs-based thin films was achieved and characterized for the first time. The study demonstrated that MnAs, a material of high relevance for spintronic applications, can be electrochemically synthesized, displaying promising ferromagnetic properties at room temperature. The obtained films exhibited a combination of MnAs and MnO_2 phases, both significant for spin-polarized charge transport. This result is particularly meaningful, as it extends the scope of electrodeposition beyond conventional applications and into the fabrication of magnetic materials traditionally accessible only through high-vacuum methods such as molecular beam epitaxy or sputtering.

The fourth and fifth chapters expanded the investigation to the electrodeposition of metals on silicon substrates, including a detailed study on the electrochemical behavior of rhodium, which provided valuable insights into its nucleation and growth mechanisms on n-type silicon. The work demonstrated that rhodium can form nanostructured deposits, confirming its suitability as a catalytic and functional layer for advanced energy and sensing applications. This part of the research, established a direct correlation between deposition parameters, surface morphology, and electrochemical performance, contributing to the broader understanding of noble-metal electrodeposition on semiconductors. The study therefore continued with a particular focus on the role of electrodeposited metals in the controlled fabrication of nanostructured surfaces and silicon nanowires (NWs) through metal-assisted chemical etching (MACE). These studies confirmed that electrodeposition allows precise control over the growth of catalytic metal layers on doped silicon, directly influencing the uniformity and morphology of the resulting nanostructures. The ability to generate well-defined silicon NWs represents a significant contribution to the field of silicon-based nanotechnologies, with potential implications for

photoelectrochemical energy conversion, sensing, and miniaturized device fabrication.

The sixth chapter explored the electrodeposition of the Ni–Mn–As ternary alloy on silicon, proposing it as a novel tool for the oxygen evolution reaction (OER) optimization. These findings highlight the potential of electrodeposited multicomponent alloys as efficient, scalable, and cost-effective alternatives to noble-metal-based catalysts for water oxidation and hydrogen production. The work also emphasizes how composition control through electrodeposition can tailor the catalytic and electronic properties of complex materials, thus opening new possibilities for energy storage and conversion technologies.

The seventh chapter shifted the perspective from fundamental research to industrial application, addressing sustainability challenges within the decorative electroplating industry. Conducted in collaboration with the company Lotti S.r.l., this part of the project focused on replacing hazardous compounds such as cyanides, optimizing formulations composition, and implementing real-time analytical monitoring and digital process control systems aligned with Industry 4.0 paradigms. The results demonstrated that it is possible to achieve significant reductions in environmental impact and process waste while maintaining high-quality surface finishes and economic competitiveness. This work provides a concrete example of how academic research can directly contribute to innovation and sustainability in manufacturing.

Taken together, these studies illustrate the breadth and impact of electrodeposition as a unifying technology that connects fundamental materials science with applied industrial development. The results achieved not only deepen the scientific understanding of electrodeposited semiconductors, alloys, and nanostructures but also deliver practical methodologies for integrating these materials into sustainable technologies and production chains. The combined academic and industrial outcomes underscore the role of electrochemical synthesis as a strategic enabler for the transition toward cleaner and smarter manufacturing models.

Looking ahead, several promising research directions arise from this work. Future studies could focus on the optimization of deposition parameters to achieve pure and ordered alloy phases on semiconductor substrates, enabling improved spin polarization and magnetic ordering. The integration of photoelectrochemical and spintronic functionalities may also lead to new concepts for direct solar-to-hydrogen energy conversion. On the industrial side, the continued evolution of electroplating processes could further enhance efficiency, reproducibility, and environmental performance across production lines.

In conclusion, this doctoral research contributes to the broader vision of sustainable technological advancement by demonstrating that electrochemical synthesis can effectively unite efficiency, scalability, and environmental responsibility. Electrodeposition emerges not merely as a fabrication method but as a flexible and forward-looking platform capable of addressing critical challenges in energy, materials, and manufacturing. By combining rigorous scientific inquiry with industrial applicability, this work exemplifies how innovation in electrochemistry

can support the development of a more sustainable and intelligent technological future.

9 References

1. Foresti ML. Elettrochimica 2008/2009 Cap. VIII – Tecniche Elettrochimiche M. L. Foresti. Published online 2009:1-5.
2. Foresti ML. Elettrochimica dei materiali e dei nanosistemi 2013/2014 Cap. III – Materiali elettrodici e tecniche elettrochimiche di base M. L. Foresti. Published online 2014:1-62.
3. Zhang XG. *Electrochemistry of Silicon and Its Oxide*. Springer US; 2001.
4. Electrical & Computer Engineering, Integrated Microfabrication Lab BY university. Metal-semiconductor ohmic and Schottky contacts.
5. Filho SG dos S, Hasenack CM, Salay LC, Mertens P. A Less Critical Cleaning Procedure for Silicon Wafer Using Diluted HF Dip and Boiling in Isopropyl Alcohol as Final Steps. *J Electrochem Soc*. 1995;142(3):902-907. doi:10.1149/1.2048555
6. Gronet CM, Lewis NS, Cogan G, Gibbons J. n-Type silicon photoelectrochemistry in methanol: Design of a 10.1% efficient semiconductor/liquid junction solar cell. *Proc Natl Acad Sci*. 1983;80(4):1152-1156. doi:10.1073/pnas.80.4.1152
7. Burrows VA, Chabal YJ, Higashi GS, Raghavachari K, Christman SB. Infrared spectroscopy of Si(111) surfaces after HF treatment: Hydrogen termination and surface morphology. *Appl Phys Lett*. 1988;53(11):998-1000. doi:10.1063/1.100053
8. Sacher E, Yelon A. Comment on Mechanism of HF etching of silicon surfaces: A theoretical understanding of hydrogen passivation. *Phys Rev Lett*. 1991;66(12):1647. doi:10.1103/PhysRevLett.66.1647
9. Mende G, FINSTER J, FLAMM D, SCHULZE D. and J. FINSTER,. *Surf Sci*. 1983;128:169-175.
10. Gräf D, Grundner M, Schulz R. Reaction of water with hydrofluoric acid treated silicon(111) and (100) surfaces. *J Vac Sci Technol A Vacuum, Surfaces, Film*. 1989;7(3):808-813. doi:10.1116/1.575845
11. Pinarbasi M, Kent AD. Perspectives on spintronics technology development: Giant magnetoresistance to spin transfer torque magnetic random access memory. *APL Mater*. 2022;10(2). doi:10.1063/5.0075945
12. Bhatti S, Sbiaa R, Hirohata A, Ohno H, Fukami S, Piramanayagam SN. Spintronics based random access memory: a review. *Mater Today*. 2017;20(9):530-548. doi:10.1016/j.mattod.2017.07.007
13. Wolf SA, Chtchelkanova AY, Treger DM. Spintronics - A retrospective and perspective. *IBM J Res Dev*. 2006;50(1):101-110. doi:10.1147/rd.501.0101
14. Graf T, Felser C, Parkin SSP. Simple rules for the understanding of Heusler compounds. *Prog Solid State Chem*. 2011;39(1):1-50. doi:10.1016/j.progsolidstchem.2011.02.001
15. Bai Z, Shen LEI, Han G, Feng YP. Data storage: review of heusler compounds. *Spin*. 2012;2(4):1-16. doi:10.1142/S201032471230006X

16. Singh M, Singh H, Kashyap MK. Effect of atomic disorder on half-metallic ferromagnetism in Fe 3-xCrxSi (x= 0, 0.25, 0.75, 1) heusler alloys. *AIP Conf Proc*. 2012;1447(1):1111-1112. doi:10.1063/1.4710396
17. Elphick K, Frost W, Samiepour M, et al. *Heusler Alloys for Spintronic Devices: Review on Recent Development and Future Perspectives*. Vol 22. Taylor & Francis; 2021. doi:10.1080/14686996.2020.1812364
18. R. A. de Groot and F. M. Mueller. New Class of Materials: Half-Metallic Ferromagnets. *Strateg Manag J*. 1983;50(25):2024-2027. doi:10.1002/smj.842
19. Innocenti M, Passaponti M, Giurlani W, et al. Spin dependent electrochemistry : Focus on chiral vs achiral charge transmission through 2D SAMs adsorbed on gold ☆. *J Electroanal Chem*. 2020;856:113705. doi:10.1016/j.jelechem.2019.113705
20. Tezuka N, Ikeda N, Mitsuhashi F, Sugimoto S. Improved tunnel magnetoresistance of magnetic tunnel junctions with Heusler Co2 FeAl0.5 Si0.5 electrodes fabricated by molecular beam epitaxy. *Appl Phys Lett*. 2009;94(16):0-3. doi:10.1063/1.3116717
21. Watanabe N, Sano K, Tasugi N, et al. Preparation of Co2FeSn Heusler alloys by electrodeposition method. *APL Mater*. 2015;3(4):1-6. doi:10.1063/1.4918639
22. Hakimi M, Kameli P, Salamati H. Structural and magnetic properties of Co2CrAl Heusler alloys prepared by mechanical alloying. *J Magn Magn Mater*. 2010;322(21):3443-3446. doi:10.1016/j.jmmm.2010.06.042
23. Jayakumar OD, Tyagi AK. *Spintronic Materials, Synthesis, Processing and Applications*. Elsevier Inc.; 2011. doi:10.1016/B978-0-12-385142-0.00005-2
24. Keavney D, Falco C. Deposition Techniques for Magnetic Thin Films and Multilayers. *ChemInform*. 2004;35(9):85721. doi:10.1002/chin.200409262
25. Goktas A, Mutlu IH, Yamada Y, Celik E. Influence of pH on the structural optical and magnetic properties of Zn1-xMnxO thin films grown by sol-gel method. *J Alloys Compd*. 2013;553:259-266. doi:10.1016/j.jallcom.2012.11.097
26. Göktaş A, Mutlu IH. Room temperature ferromagnetism in Mn-doped ZnS nanocrystalline thin films grown by sol-gel dip coating process. *J Sol-Gel Sci Technol*. 2014;69(1):120-129. doi:10.1007/s10971-013-3194-3
27. Mocuta C, Bonamy D, Stanescu S, et al. Finite size effect on the structural and magnetic properties of MnAs/GaAs(001) patterned microstructures thin films. *Sci Rep*. 2017;7(1):1-18. doi:10.1038/s41598-017-17251-y
28. Prima-garcia H, Coronado E, Prieto-ruiz JP, Romero FM. Tailoring magnetic properties of electrodeposited thin films of the molecule-based magnet. Published online 2012:2-5.
29. Fan S, Zhou C, Xu H, et al. A novel strategy to improve giant magnetoresistance effect of Co/Cu multilayered nanowires arrays. *J Alloys Compd*. 2022;910:164729. doi:10.1016/j.jallcom.2022.164729

30. Watanabe N, Sano K, Tasugi N, et al. Preparation of Co2FeSn Heusler alloys by electrodeposition method. *APL Mater*. 2015;3(4):1-6. doi:10.1063/1.4918639
31. Hai PN, Yokoyama M, Ohya S, Tanaka M. Spin polarized tunneling in III-V-based heterostructures with a ferromagnetic MnAs thin film and GaAs:MnAs nanoclusters. *Phys E Low-Dimensional Syst Nanostructures*. 2006;32(1-2 SPEC. ISS.):416-418. doi:10.1016/j.physe.2005.12.082
32. Trassinelli M, Gafton VE, Eddrief M, et al. Magnetic properties of MnAs thin films irradiated with highly charged ions. *Nucl Instruments Methods Phys Res Sect B Beam Interact with Mater Atoms*. 2013;317(PART A):154-158. doi:10.1016/j.nimb.2013.04.025
33. Mizuguchi M, Kuramochi H, Okabayashi J, Manago T, Akinaga H. Magnetic domain structure of MnAs thin films as a function of temperature. *Mater Trans*. 2003;44(12):2578-2581. doi:10.2320/matertrans.44.2578
34. Kubo K, Kato Y, Kanai K, Ohta J, Fujioka H, Oshima M. Growth and magnetic properties of zb-type MnAs films on GaAs substrates by high-temperature MBE. *J Cryst Growth*. 2008;310(21):4535-4538. doi:10.1016/j.jcrysgro.2008.08.051
35. Ma J, Hegde VI, Munira K, et al. Computational investigation of half-Heusler compounds for spintronics applications. *Phys Rev B*. 2017;95(2):1-25. doi:10.1103/PhysRevB.95.024411
36. Ma J, He J, Mazumdar D, et al. PHYSICAL REVIEW B 98 , 094410 (2018) Computational investigation of inverse Heusler compounds for spintronics applications. 2018;094410:1-26. doi:10.1103/PhysRevB.98.094410
37. Akeura K, Tanaka M, Ueki M, Nishinaga T. Epitaxial ferromagnetic MnAs thin films grown by molecular beam epitaxy on Si (001) substrates Epitaxial ferromagnetic MnAs thin films grown by molecular beam epitaxy. 1995;3349(May 2013). doi:10.1063/1.115243
38. Fedorchenko I V, Kilanski L, Zakharchuk I, et al. Composites based on self-assembled MnAs ferromagnet nanoclusters embedded in ZnSnAs2 semiconductor. *J Alloys Compd*. 2015;650:277-284. doi:10.1016/j.jallcom.2015.08.006
39. Lu J, Dreisinger D, Glück T. Hydrometallurgy Manganese electrodeposition — A literature review. *Hydrometallurgy*. 2014;141:105-116. doi:10.1016/j.hydromet.2013.11.002
40. Jia Z, Simm AO, Dai X, Compton RG. The electrochemical reaction mechanism of arsenic deposition on an Au (1 1 1) electrode. 2006;587:247-253. doi:10.1016/j.jelechem.2005.11.017
41. Pourbaix M. Atlas of Electrochemical Equilibria in Aqueous Solutions. *Natl Assoc Corros Eng Cent Beige d'Etude la Corros CEBELCOR*. Published online 1967:644.
42. Wang R qi, Lei T min, Fang Y wen. First-principles design of ferromagnetic monolayer MnO2 at the complex interface. *Phys Scr*. 2023;98(6).

doi:10.1088/1402-4896/acd7b3
43. Solzi M, Pernechele C, Ghidini M, Natali M, Bolzan M. Journal of Magnetism and Magnetic Materials Magnetic analysis of MnAs films grown on GaAs and Si substrates for potential spintronics and magnetocaloric applications. *J Magn Magn Mater*. 2010;322(9-12):1565-1568. doi:10.1016/j.jmmm.2009.09.013
44. Lu J, Dreisinger D, Glück T. Manganese Electrodeposition - A Literature Review. *Hydrometallurgy*. 2013;141:105-116. doi:10.1016/j.hydromet.2013.11.002
45. Beamson G, Moslemzadeh N, Weightman P, Watts JF. Al K ⎵ and Cu K ⎵ 1 excited XPS of vanadium oxide and VF 3 powders : Measurement of the V 1s – KLL Auger parameters. 2008;162:19-24. doi:10.1016/j.elspec.2007.08.001
46. Shirley DA. High-Resolution X-ray Photoemission Spectrum of the Valence Bands of Gold. *Phys Rev B*. 1972;5:4709–4714.
47. Susi T, Pichler T, Ayala P. X-ray photoelectron spectroscopy of graphitic carbon nanomaterials doped with heteroatoms. Published online 2015:177-192. doi:10.3762/bjnano.6.17
48. Abdel-Aziz AM, Hassan HH, Badr IHA. Glassy Carbon Electrode Electromodification in the Presence of Organic Monomers: Electropolymerization versus Activation. *Anal Chem*. 2020;92(11):7947-7954. doi:10.1021/acs.analchem.0c01337
49. Messier R, Yehoda JE, Messier R, Yehoda JE. Geometry of thinfilm morphology Geometry of thin-film morphology. 1985;3739. doi:10.1063/1.335639
50. Thorpe SD, Arciprete F, Placidi E, Patella F, Fanfoni M. XPS and STM study of Mn incorporation on the GaAs(001) surface. *Superlattices Microstruct*. 2009;46(1-2):258-265. doi:10.1016/j.spmi.2008.12.021
51. Hatfield SA, Veal TD, Mcconville CF, Bell GR, Edmonds KW. Photoelectron spectroscopy study of Ga1-_xMnxAs(0 0 1) surface oxide and low temperature cleaning. *Surf Sci*. 2005;585:66-74. doi:10.1016/j.susc.2005.04.012
52. Oshima M, Mizuguchi M, Ono K, Akinaga H, Sugiyama M. Formation , properties and photoelectron spectroscopy of magnetic nanostructures. *J Electron Spectros Relat Phenomena*. 2002;124:165-174. doi:10.1016/S0368-2048(02)00052-X
53. Stec BYWJ, Morgan WE, Albridge RG, Wazer JRVAN. Measured Binding Energy Shifts of the “3p” and “3d” Electrons in Arsenic Compounds. *Inorg Chem*. 1972;11(2). doi:10.1021/ic50108a001
54. Moulder J, Stickle Wi, Sobol P, Kenneth B. Handbook of X-ray Photoelectron Spectroscopy. Published online 1992.
55. Lin X, Tabassum D, Rudyk BW, Mar A. Manganese-Substituted Rare-Earth Zinc Arsenides RE1−yMnxZn2−xAs2 (RE = Eu−Lu) and

RE2−yMnxZn4−xAs4 (RE = La−Nd, Sm, Gd). *Inorg Chem*. 2014;2:0-10. doi:10.1021/ic501053v
56. Ajith N, Bhattacharyya K, Ipte PR, et al. Interaction of arsenic(III) and arsenic(V) on manganese dioxide: XPS and electrochemical investigations. *J Environ Sci Heal - Part A Toxic/Hazardous Subst Environ Eng*. 2019;54(4):277-285. doi:10.1080/10934529.2018.1544478
57. Biesinger MC, Payne BP, Grosvenor AP, et al. Applied Surface Science Resolving surface chemical states in XPS analysis of first row transition metals , oxides and hydroxides : Cr , Mn , Fe , Co and Ni. *Appl Surf Sci*. 2011;257(7):2717-2730. doi:10.1016/j.apsusc.2010.10.051
58. Yeh JJ. *Atomic Calculation of Photoionization Cross-Section and Asymmetry Parameters*. Gordon and Breach; 1993.
59. Yeh JJ, Lindau I. Atomic subshell photoionization cross sections and asymmetry parameters: $1 \leqslant Z \leqslant 103$. *At Data Nucl Data Tables*. 1985;32(l):1-155. doi:https://doi.org/10.1016/0092-640X(85)90016-6
60. Tournassat C, Charlet L, Bosbach D, Manceau A. Arsenic(III) oxidation by birnessite and precipitation of manganese(II) arsenate. *Environ Sci Technol*. 2002;36(3):493-500. doi:10.1021/es0109500
61. Weil M, Kolitsch U. Dimorphism of MnHAsO 4 (H 2 O): natural monoclinic krautite and its synthetic triclinic modi fi cation. 2022;77:221-230.
62. Schippan F, Behme G, Däweritz L, et al. Magnetic structure of epitaxially grown MnAs on GaAs(001). *J Appl Phys*. 2000;88(5):2766-2770. doi:10.1063/1.1287607
63. Le Bail A. Whole powder pattern decomposition methods and applications: A retrospection. *Powder Diffr*. 2005;20(4):316-326. doi:10.1154/1.2135315
64. Abrams H. Grain size measurement by the intercept method. *Metallography*. 1971;4(1):59-78. doi:10.1016/0026-0800(71)90005-X
65. Zhang Z, Jiang C, Fu P, Cai F, Ma N. Microstructure and texture of electrodeposited Ni-ZrC composite coatings investigated by Rietveld XRD line profile analysis. *J Alloys Compd*. 2015;626:118-123. doi:10.1016/j.jallcom.2014.11.144
66. Wyckoff RWG. *Crystal Structures - Volume 1*. 2nd ed. Interscience Publishers; 1963.
67. Aba Z, Goktas A, Kilic A. Characterization of Zn1-xLaxS thin films; compositional, surface, optical, and photoluminescence properties for possible optoelectronic and photocatalytic applications. *J Sol-Gel Sci Technol*. 2024;109(1):260-271. doi:10.1007/s10971-023-06273-w
68. Goktas S, Tumbul A, Goktas A. Growth Technique–Induced Highly C-Axis-Oriented ZnO: Mn, Zno: Fe and ZnO: Co Thin Films: A Comparison of Nanostructure, Surface Morphology, Optical Band Gap, and Room Temperature Ferromagnetism. *J Supercond Nov Magn*. 2023;36(10-12):1875-1892. doi:10.1007/s10948-023-06630-4

69. Downs RT, Hall-Wallace M. American Mineralogist Crystal Structure Database.
70. Horiguchi R, Hara S, Iida M. Magnetic domain structure and domain wall analysis of ferromagnetic MnAs nanodisks selectively-grown on Si (111) substrates for spintronic applications. *J Appl Phys*. 2018;124(15). doi:10.1063/1.5045241
71. Jaiganesh G, Kalpana G. First-principles study of structural, electronic and magnetic properties of AeX (Ae=Be, Mg, Sr, Ba; X=Si, Ge and Sn) compounds. *J Magn Magn Mater*. 2013;326:66-74. doi:10.1016/j.jmmm.2012.07.001
72. Panguluri RP, Tsoi G, Nadgorny B, Chun SH, Samarth N, Mazin II. Point contact spin spectroscopy of ferromagnetic MnAs epitaxial films. *Phys Rev B - Condens Matter Mater Phys*. 2003;68(20):4-7. doi:10.1103/PhysRevB.68.201307
73. created in Chris Wolverton's group at Northwestern University. The Open Quantum Materials Database. https://oqmd.org/
74. The Materials Project.
75. Matsukura F, Ohno H, Shen A, Sugawara Y. Transport properties and origin of ferromagnetism in (Ga, Mn)As. *Phys Rev B - Condens Matter Mater Phys*. 1998;57(4):R2037-R2040. doi:10.1103/PhysRevB.57.R2037
76. Giurlani W, Vizza M, Pizzetti F, et al. Magnetic Field Effect on the Handedness of Electrodeposited Heusler Alloy. *Appl Sci*. 2022;12(11):5640.
77. Atmane KA, Michel C, Piquemal JY, et al. Control of the anisotropic shape of cobalt nanorods in the liquid phase: From experiment to theory... and back. *Nanoscale*. 2014;6(5):2682-2692. doi:10.1039/c3nr03686c
78. Hochheimer HD, Honle W. To [22]. 1986;118(6):293-296.
79. Kan M, Zhou J, Sun Q, Kawazoe Y, Jena P. The intrinsic ferromagnetism in a MnO2 monolayer. *J Phys Chem Lett*. 2013;4(20):3382-3386. doi:10.1021/jz4017848
80. Oomori K, Asubar JT, Ishibashi T, Jinbo Y, Uchitomi N. Magnetic properties and surface morphology of MnAs thin films grown by MBE on GaAs(111) substrates. *IOP Conf Ser Mater Sci Eng*. 2011;21(1):0-5. doi:10.1088/1757-899X/21/1/012024
81. Sulka GD. Electrochemistry of Thin Films and Nanostructured Materials. *Molecules*. 2023;28(10). doi:10.3390/molecules28104040
82. Fukata N, Subramani T, Jevasuwan W, Dutta M, Bando Y. Functionalization of Silicon Nanostructures for Energy-Related Applications. *Small*. 2017;13(45):1-13. doi:10.1002/smll.201701713
83. Kuntyi OI, Zozulya GI, Shepida M V., Nichkalo SI. Deposition of nanostructured metals on the surface of silicon by galvanic replacement: A mini-review. *Vopr Khimii i Khimicheskoi Tekhnologii*. 2019;2019(3):74-82. doi:10.32434/0321-4095-2019-124-3-74-82
84. Azzaroni O, Fonticelli M, Schilardi PL, et al. Surface nanopatterning of

metal thin films by physical vapour deposition onto surface-modified silicon nanodots. *Nanotechnology*. 2004;15(4). doi:10.1088/0957-4484/15/4/014
85. Abo Ghazala MS, Othman HA, Sharaf El-Deen LM, Nawwar MA, Kashyout AEHB. Fabrication of nanocrystalline silicon thin films utilized for optoelectronic devices prepared by thermal vacuum evaporation. *ACS Omega*. 2020;5(42):27633-27644. doi:10.1021/acsomega.0c04206
86. Droopad R, Curless JA, Yu Z, et al. Development of integrated heterostructures on silicon by MBE. *MBE 2002 - 2002 12th Int Conf Mol Beam Ep*. 2002;251:45-46. doi:10.1109/MBE.2002.1037752
87. Jaydeep Sarkar. *Sputtering Materials for VLSI and Thin Film Devices*. 1st Editio. Elsevier; 2000.
88. Thomann AL, Vahlas C, Aloui L, et al. Conformity of aluminum thin films deposited onto micro-patterned silicon wafers by pulsed laser deposition, magnetron sputtering, and CVD. *Chem Vap Depos*. 2011;17(10-12):366-374. doi:10.1002/cvde.201106936
89. Mitzi DB, Kosbar LL, Murray CE, Copel M, Afzali A. High-mobility ultrathin semiconducting films prepared by spin coating. *Nature*. 2004;428(6980):299-303. doi:10.1038/nature02389
90. Srinivasan K, Kottantharayil A. Aluminium oxide thin film deposited by spray coating for p-type silicon surface passivation. *Sol Energy Mater Sol Cells*. 2019;197(April):93-98. doi:10.1016/j.solmat.2019.03.048
91. Tumelero MA, Benetti LC, Isoppo E, Faccio R, Zangari G, Pasa AA. Electrodeposition and ab Initio Studies of Metastable Orthorhombic Bi2Se3: A Novel Semiconductor with Bandgap for Photovoltaic Applications. *J Phys Chem C*. 2016;120(22):11797-11806. doi:10.1021/acs.jpcc.6b02559
92. Foresti ML, Milani S, Loglio F, Innocenti M, Pezzatini G, Cattarin S. Ternary CdSxSe1-x deposited on Ag(111) by ECALE: Synthesis and characterization. *Langmuir*. 2005;21(15):6900-6907. doi:10.1021/la050176k
93. Giurlani W, Giaccherini A, Calisi N, et al. Investigations on the Electrochemical Atomic Layer Growth of Bi2Se3 and the Surface Limited Deposition of Bismuth at the Silver Electrode. *Materials (Basel)*. 2018;11(8):1426. doi:10.3390/ma11081426
94. Giurlani W, Giaccherini A, Salvietti E, et al. Selective Electrodesorption-Based Atomic Layer Deposition (SEBALD) of Bismuth under Morphological Control. *Electrochem Soc Interface*. 2018;27(2):77-81. doi:10.1149/2.F08182if
95. Gregory BW, Stickney JL. Electrochemical atomic layer epitaxy (ECALE). *J Electroanal Chem*. 1991;300(1-2):543-561. doi:10.1016/0022-0728(91)85415-L
96. Vizza M, Giaccherini A, Giurlani W, et al. Successes and Issues in the Growth of Moad and MoSe2 on Ag(111) by the E-ALD Method. *Metals (Basel)*. 2019;9(2):122. doi:10.3390/met9020122
97. Ogata YH, Kobayashi K, Motoyama M. Electrochemical metal deposition

on silicon. *Curr Opin Solid State Mater Sci*. 2006;10(3-4):163-172. doi:10.1016/j.cossms.2007.02.001
98. Tung RT. Recent advances in Schottky barrier concepts. *Mater Sci Eng R Reports*. 2001;35(1-3):1-138. doi:10.1016/S0927-796X(01)00037-7
99. SATO N. Electrocthemistry of Semiconductors. *Tetsu-to-Hagane*. 1990;76(9):1423-1436. doi:10.2355/tetsutohagane1955.76.9_1423
100. Oskam G, Long JG, Natarajan A, Searson PC. Electrochemical deposition of metals onto silicon. *J Phys D Appl Phys*. 1998;31(16):1927-1949. doi:10.1088/0022-3727/31/16/001
101. Giurlani W, Dell'Aquila V, Vizza M, et al. Electrodeposition of Nanoparticles and Continuous Film of CdSe on n-Si (100). *Nanomaterials*. 2019;9(10):1504. doi:10.3390/nano9101504
102. Prod'Homme P, Maroun F, Cortès R, Allongue P. Electrochemical growth of ultraflat Au(111) epitaxial buffer layers on H-Si(111). *Appl Phys Lett*. 2008;93(17). doi:10.1063/1.3006064
103. Skachkov D, Liu S long, Wang Y, Zhang X guang, Cheng H ping. PHYSICAL REVIEW B 104 , 045429 (2021) First-principles theory for Schottky barrier physics. 2021;045429:47-49. doi:10.1103/PhysRevB.104.045429
104. Muñoz AG. Electroplating of Rhodium/Si(111) Junctions for Solar Fuel Generation: Effects of Hydrogen Diffusion. *J Electrochem Soc*. 2014;161(10):D571-D578. doi:10.1149/2.1041410jes
105. Wasilewska J, Chmielarek M, Skupiński W. Study of Rh/TiO2–SiO2 system in photolytic water splitting. *React Kinet Mech Catal*. 2021;132(2):1165-1192. doi:10.1007/s11144-020-01924-3
106. Dang Q, Liao F, Sun Y, et al. Rhodium/silicon quantum dot/carbon quantum dot composites as highly efficient electrocatalysts for hydrogen evolution reaction with Pt-like performance. *Electrochim Acta*. 2019;299:828-834. doi:10.1016/j.electacta.2019.01.031
107. Song Z, Chang H, Zhu W, Xu C, Feng X. Rhodium Nanoparticle-mesoporous Silicon Nanowire Nanohybrids for Hydrogen Peroxide Detection with High Selectivity. *Sci Rep*. 2015;5:1-4. doi:10.1038/srep07792
108. Marot L, Schoch R, Steiner R, Thommen V, Mathys D, Meyer E. Rhodium and silicon system: II. Rhodium silicide formation. *Nanotechnology*. 2010;21(36):365707. doi:10.1088/0957-4484/21/36/365707
109. Grätzel M. Highly Efficient Nanocrystalline Photovoltaic Devices. *Platin Met Rev*. 1994;38(4):151-159. doi:10.1595/003214094x384151159
110. Pillai S, Catchpole KR, Trupke T, Zhang G, Zhao J, Green MA. Enhanced emission from Si-based light-emitting diodes using surface plasmons. *Appl Phys Lett*. 2006;88(16):1-4. doi:10.1063/1.2195695
111. Wang F, Chen G, Zhang N, Liu X, Ma R. Engineering of carbon and other protective coating layers for stabilizing silicon anode materials. *Carbon Energy*. 2019;1(2):219-245. doi:10.1002/cey2.24

112. Feng L, Zhang M, Wang J, et al. Silicon photonic devices for scalable quantum information applications. *Photonics Res*. 2022;10(10):A135. doi:10.1364/prj.464808
113. Yalavarthi R, Yesilyurt O, Henrotte O, et al. Multimetallic Metasurfaces for Enhanced Electrocatalytic Oxidations in Direct Alcohol Fuel Cells. *Laser Photonics Rev*. 2022;16(7):1-10. doi:10.1002/lpor.202200137
114. Ullah A, Wang YC, Yeasmin S, et al. Reconfigurable photoinduced terahertz wave modulation using hybrid metal–silicon metasurface. *Opt Lett*. 2022;47(11):2750. doi:10.1364/ol.457573
115. Kern W. The Evolution of Silicon Wafer Cleaning Technology. 1990;137(6):7-12. doi:10.1149/1.2086825
116. Tian F, Yang D, Opila RL, Teplyakov A V. Applied Surface Science Chemical and electrical passivation of Si (1 1 1) surfaces. *Appl Surf Sci*. 2012;258(7):3019-3026. doi:10.1016/j.apsusc.2011.11.030
117. Giurlani W, Cavallini M, Picca RA, et al. Underpotential-Assisted Electrodeposition of Highly Crystalline and Smooth Thin Film of Bismuth. *ChemElectroChem*. 2020;7(1):299-305. doi:10.1002/celc.201901678
118. Innocenti M, Pezzatini G, Forni F, Foresti ML. CdS and ZnS Deposition on Ag(111) by Electrochemical Atomic Layer Epitaxy. *J Electrochem Soc*. 2001;148(5):C357. doi:10.1149/1.1360208
119. X-ray Photoelectron Spectroscopy (XPS) Reference Pages. Accessed January 10, 2024. https://www.xpsfitting.com/
120. Jha D, Ward L, Paul A, et al. ElemNet: Deep Learning the Chemistry of Materials From Only Elemental Composition. *Sci Rep*. 2018;8(1):1-13. doi:10.1038/s41598-018-35934-y
121. Agrawal A, Meredig B, Wolverton C, Choudhary A. A Formation Energy Predictor for Crystalline Materials Using Ensemble Data Mining. *IEEE Int Conf Data Min Work ICDMW*. 2016;0:1276-1279. doi:10.1109/ICDMW.2016.0183
122. Meredig B, Agrawal A, Kirklin S, et al. Combinatorial screening for new materials in unconstrained composition space with machine learning. *Phys Rev B - Condens Matter Mater Phys*. 2014;89(9):1-7. doi:10.1103/PhysRevB.89.094104
123. Jain A, Ong SP, Hautier G, et al. Commentary : The Materials Project : A materials genome. *APL Mater*. 2013;1(011002):1-11. doi:10.1063/1.4812323
124. Palmstrøm CJ. Contacts for Compound Semiconductors : Ohmic Type. *Encycl Mater Sci Technol (Second Ed*. Published online 2001:1581-1587. doi:doi.org/10.1016/B0-08-043152-6/00282-5
125. Tu KN, Thompson RD, Tsaur BY, Tu KN, Thompson RD, Tsaur BY. Low Schottky barrier of rareearth silicide on nSi. 1981;626:6-9. doi:10.1063/1.92457
126. Herrero E, Buller LJ, Abruna D. Underpotential Deposition at Single Crystal

Surfaces of Au , Pt , Ag and Other Materials. *Chem Rev*. 2001;101(7):1897-1930. doi:doi.org/10.1021/cr9600363
127. Sarkar S, Sebastian PC. Inorganic chemistry. *Inorg Chem Front*. 2018;(9). doi:10.1039/C8QI00042E
128. Cheng N, Stambula S, Wang D, et al. Hydrogen evolution reaction. *Nat Commun*. 2016;7:1-9. doi:10.1038/ncomms13638
129. Zhu L, Lin H, Li Y, et al. A rhodium/silicon co-electrocatalyst design concept to surpass platinum hydrogen evolution activity at high overpotentials. *Nat Publ Gr*. 2016;7. doi:10.1038/ncomms12272
130. Lee J, Arrigan DWM, Silvester DS. Mechanical polishing as an improved surface treatment for platinum screen-printed electrodes. *Sens Bio-Sensing Res*. 2016;9:38-44. doi:10.1016/j.sbsr.2016.05.006
131. Michaelson HB. The work function of the elements and its periodicity. 1977;48:4729-4733. doi:10.1063/1.323539
132. Lattice Constants for all the elements in the Periodic Table.
133. Philipsen H, Jehoul H, Inoue F, et al. Nucleation and growth kinetics of electrodeposited Ni films on Si(100) surfaces. *Electrochim Acta*. 2017;230:407-417. doi:10.1016/j.electacta.2017.02.010
134. Philipsen H, Monnens W. Immersion and electrochemical deposition of Ru on Si. *Electrochim Acta*. 2018;274:306-315. doi:10.1016/j.electacta.2018.04.093
135. Palladium, X-Ray Photoelectron Spectroscopy (XPS) Reference Pages. Accessed January 10, 2024. http://www.xpsfitting.com/2017/10/%0Apalladium.html
136. Platinum, X-Ray Photoelectron Spectroscopy (XPS) Reference Pages. Accessed January 10, 2024. http://www.xpsfitting.com/2012/01/%0Aplatinum.html
137. Rhodium, X-Ray Photoelectron Spectroscopy (XPS) Reference Pages. Accessed January 10, 2024. http://www.xpsfitting.com/2016/12/%0Arhodium.html
138. Kreyling WG, Semmler-Behnke M, Chaudhry Q. A complementary definition of nanomaterial. *Nanotoday*. 2010;5(3):165-168. doi:10.1016/j.nantod.2010.03.004
139. Morganti D, Leonardi AA, Jos M, et al. Ultrathin Silicon Nanowires for Optical and Electrical Nitrogen Dioxide Detection. 2021;(x):1-13.
140. Jones AC, Hitchman ML. *Chemical Vapour Deposition: Precursors, Processes and Applications*. Royal Society of Chemistry; 2008. doi:10.1039/9781847558794-00357
141. Hossain MI, Mohammad A, Qarony W, et al. Atomic layer deposition of metal oxides for efficient perovskite single-junction and perovskite/silicon tandem solar cells. *RSC Adv*. 2020;10(25):14856-14866. doi:10.1039/d0ra00939c
142. Pappaianni G, Giurlani W, Bonechi M, et al. Electrodeposition of MnAs-

Based Thin-Film as a Possible Promising Candidate in Spintronics Applications. *J Electrochem Soc*. 2024;171(6):062502. doi:10.1149/1945-7111/ad5112
143. Giurlani W, Pappaianni G, Biffoli F, et al. What Is the Current State of Sustainability in the Decorative Electroplating Industry? A Close Look at New Practices and Advances. *Sustain* . 2024;16(13). doi:10.3390/su16135821
144. Ivanova YA, Ivanou DK, Streltsov EA. Electrodeposition of PbSe onto n-Si(1 0 0) wafers. *Electrochim Acta*. 2008;53(15):5051-5057. doi:10.1016/j.electacta.2007.12.066
145. Pappaianni G, Montanari F, Bonechi M, Zangari G, Giurlani W, Innocenti M. Electrodeposition of Nanostructured Metals on n-Silicon and Insights into Rhodium Deposition. *Nanomaterials*. 2024;14(24):2042. doi:10.3390/nano14242042
146. Giurlani W, Vizza M, Leonardi AA, Lo Faro MJ, Irrera A, Innocenti M. Optimization and Characterization of Electrodeposited Cadmium Selenide on Monocrystalline Silicon. *Nanomaterials*. 2022;12(4):610. doi:10.3390/nano12040610
147. Yae S, Kawamoto Y, Tanaka H, Fukumuro N, Matsuda H. Formation of porous silicon by metal particle enhanced chemical etching in HF solution and its application for efficient solar cells. *Electrochem commun*. 2003;5(8):632-636. doi:10.1016/S1388-2481(03)00146-2
148. Peng K, Wu Y, Fang H, Zhong X, Xu Y, Zhu J. Uniform, axial-orientation alignment of one-dimensional single-crystal silicon nanostructure arrays. *Angew Chemie - Int Ed*. 2005;44(18):2737-2742. doi:10.1002/anie.200462995
149. Irrera A, Lo Faro MJ, D'Andrea C, et al. Light-emitting silicon nanowires obtained by metal-assisted chemical etching. *Semicond Sci Technol*. 2017;32(4). doi:10.1088/1361-6641/aa60b8
150. Huang Z, Geyer N, Werner P, De Boor J, Gösele U. Metal-assisted chemical etching of silicon: A review. *Adv Mater*. 2011;23(2):285-308. doi:10.1002/adma.201001784
151. Lai RA, Hymel TM, Narasimhan VK, Cui Y. Schottky Barrier Catalysis Mechanism in Metal-Assisted Chemical Etching of Silicon. *ACS Appl Mater Interfaces*. 2016;8(14):8875-8879. doi:10.1021/acsami.6b01020
152. Kumar J, Ingole S. Effect of Silicon Conductivity and HF/H2O2 Ratio on Morphology of Silicon Nanostructures Obtained via Metal-Assisted Chemical Etching. *J Electron Mater*. 2018;47(2):1583-1588. doi:10.1007/s11664-017-5964-0
153. Kim J, Han H, Kim YH, Choi SH, Kim JC, Lee W. Au/Ag bilayered metal mesh as a Si etching catalyst for controlled fabrication of Si nanowires. *ACS Nano*. 2011;5(4):3222-3229. doi:10.1021/nn2003458
154. Wilkinson P. Understanding gold plating. *Gold Bull*. 1986;19(3):75-81.

doi:10.1007/BF03214646
155. Aylmore MG. *Alternative Lixiviants to Cyanide for Leaching Gold Ores*. Elsevier B.V.; 2016. doi:10.1016/B978-0-444-63658-4.00027-X
156. Adams MD, Friedl J, Wagner FE. The mechanism of adsorption of Au(CN)4- onto activated carbon. *Hydrometallurgy*. 1992;31(3):265-275. doi:10.1016/0304-386X(92)90123-H
157. Irrera A, Artoni P, Iacona F, Pecora EF, Franz G. Quantum confinement and electroluminescence in ultrathin silicon nanowires fabricated by a maskless etching technique. Published online 2012. doi:10.1088/0957-4484/23/7/075204
158. Chan CK, Peng H, Liu GAO, et al. High-performance lithium battery anodes using silicon nanowires. Published online 2007:31-35. doi:10.1038/nnano.2007.411
159. Cui Y, Wei Q, Park H, Lieber CM. Nanowire Nanosensors for Highly Sensitive and Selective Detection of Biological and Chemical Species. 2001;293(August):1289-1293.
160. Pasa AA, Schwarzacher W. Electrodeposition of thin films and multilayers on silicon. *Phys Status Solidi Appl Res*. 1999;173(1):73-84. doi:10.1002/(SICI)1521-396X(199905)173:1<73::AID-PSSA73>3.0.CO;2-8
161. Swesi AT, Masud J, Nath M. Nickel Selenide As High-efficiency Catalyst for Oxygen Evolution Energy & Environmental Science Accepted Manuscript Energy & Environmental Science Accepted Manuscript. Published online 2013:1-3. doi:10.1039/C5EE02463C
162. Tian L, Zhai X, Wang X, Li J, Li Z. Advances in Manganese-Based Oxides for Oxygen Evolution Journal of Materials Chemistry A Accepted Manuscript Journal of Materials Chemistry A Accepted Manuscript. Published online 2013:24-26. doi:10.1039/D0TA05116K
163. Yu M, Li G, Fu C, Liu E, Manna K, Budiyanto E. Tunable e g Orbital Occupancy in Heusler Compounds for Oxygen Evolution Reaction **. Published online 2021:5800-5805. doi:10.1002/anie.202013610
164. Dinh VA, Sato K, Katayama-Yoshida H. New high-Tc half-Heusler ferromagnets NiMnZ (Z = Si, P, Ge, As). *J Phys Soc Japan*. 2008;77(1). doi:10.1143/JPSJ.77.014705
165. Everhart W, Newkirk J. Mechanical properties of Heusler alloys. *Heliyon*. 2019;5(5):e01578. doi:10.1016/j.heliyon.2019.e01578
166. Wei Q, Wang H, Ma J, Zhao X, Zhao J. Magneto-transport properties of cubic NiMnAs film epitaxied on GaAs (110) substrate. *J Phys Condens Matter*. 2021;33(31). doi:10.1088/1361-648X/ac03d4
167. Ma JL, Wang HL, Zhang XM, Yan S, Yan WS, Zhao JH. Epitaxial Growth and Magnetic Properties of NiMnAs Films on GaAs Substrates. *Chinese Phys Lett*. 2019;36(1):1-5. doi:10.1088/0256-307X/36/1/017501
168. Loglio F, Innocenti M, Jarek A, Caporali S, Pasquini I, Foresti ML. Nickel sulfur thin films deposited by ECALE : Electrochemical , XPS and AFM

characterization. *J Electroanal Chem*. 2010;638(1):15-20. doi:10.1016/j.jelechem.2009.10.027
169. Sun Z, He G, Zhao Z, He X, Zhao H. Research Progress of Electroplated Micropore for Interconnection Technology. *J Phys Conf Ser*. 2023;2430(1). doi:10.1088/1742-6596/2430/1/012011
170. Bandinelli R, Fani V, Bindi B. Electroplating and PVD Finishing Technologies in the Fashion Industry: Perspectives and Scenarios. *Sustainability*. 2021;13(8):4453. doi:10.3390/su13084453
171. Giurlani W, Zangari G, Id FG, et al. Electroplating for Decorative Applications : Recent Trends in Research and Development. :1-25. doi:10.3390/coatings8080260
172. United Nations. Sustainable Development Goals.
173. Jeyamala S, Kumaraguru AK, Nagarani N. Occupational health effects due to nickel and chromium exposure in electroplating workers. *Toxicol Environ Chem*. 2012;94(8):1583-1590. doi:10.1080/02772248.2012.715382
174. Moura B, Papaioannou E, Grigoropoulos A, Zoikis-Karathanasis A, Monteiro H. Sustainability of Spent Nickel-Based Electroplating Baths: An Innovative Valorisation Process. *Sustainability*. 2023;15(21):15366. doi:10.3390/su152115366
175. Xu P, Lai S, Wu L, et al. Insights into the health status of the general population living near an electroplating industry zone: metal elevations and renal impairment. *Environ Sci Pollut Res*. 2022;30(11):31905-31915. doi:10.1007/s11356-022-24411-9
176. Yu Y, Xie Y, Ji L, Zhang J, Cai Y, Yang Z. Water management for industrial development, energy conservation, and subjective attitudes: a comprehensive risk-oriented model to explore the tolerance of unbalanced allocation problem. *J Water Clim Chang*. 2022;13(1):139-157. doi:10.2166/wcc.2021.377
177. Li T, Wei G, Liu H, et al. Comparative study of electroplating sludge reutilization in China: environmental and economic performances. *Environ Sci Pollut Res*. 2023;30(48):106598-106610. doi:10.1007/s11356-023-29849-z
178. Pizzetti F, Salvietti E, Giurlani W, Emanuele R, Fontanesi C, Innocenti M. Cyanide-free silver electrodeposition with polyethyleneimine and 5,5-dimethylhydantoin as organic additives for an environmentally friendly formulation. *J Electroanal Chem*. 2022;911:116196. doi:10.1016/j.jelechem.2022.116196
179. Satpathy B, Jena S, Das S, Das K. A comprehensive review of various non-cyanide electroplating baths for the production of silver and gold coatings. *Int Mater Rev*. 2023;68(7):825-861. doi:10.1080/09506608.2022.2156723
180. Jasni AB, Yoshihara S. Electrodeposition of Silver in Cyanide-Free Solution Containing Pyrimidine Derivative as a Complexing Agent. *J Electrochem Soc*. 2023;170(9):092504. doi:10.1149/1945-7111/acf6e3

181. Sayed MA El, Elazab NT, Gassoumi M, Ibrahim MAM. Nanocrystalline silver coatings on steel by electrodeposition from non-polluting aqueous baths and its antibacterial activity. *J Taiwan Inst Chem Eng*. 2022;132:104212. doi:10.1016/j.jtice.2022.104212
182. El Sayed MA, Ibrahim MAM, T. Elazab N, Gassoumi M. Electrochemical Synthesis of Nanocrystalline CuAg Coatings on Stainless Steel from Cyanide-Free Electrolyte. *Processes*. 2022;10(10):2134. doi:10.3390/pr10102134
183. Navinšek B, Panjan P, Milošev I. PVD coatings as an environmentally clean alternative to electroplating and electroless processes. *Surf Coatings Technol*. 1999;116-119:476-487. doi:10.1016/S0257-8972(99)00145-0
184. Legg KO, Graham M, Chang P, Rastagar F, Gonzales A, Sartwell B. The replacement of electroplating. *Surf Coatings Technol*. 1996;81(1):99-105. doi:10.1016/0257-8972(95)02653-3
185. Vorobyova M, Biffoli F, Giurlani W, et al. PVD for Decorative Applications : A Review. *Materials (Basel)*. 2023;16(14):4919. doi:doi.org/10.3390/ma16144919
186. Larson C, Farr* JPG. Current research and potential applications for pulsed current electrodeposition – a review. *Trans IMF*. 2012;90(1):20-29. doi:10.1179/174591912X13238641755178
187. Kalantary MR, Gabe DR. Coating thickness distribution and morphology of pulsed current copper electrodeposits. *Surf Eng*. 1995;11(3):246-254. doi:10.1179/sur.1995.11.3.246
188. Mariani E, Giurlani W, Bonechi M, Dell'Aquila V, Innocenti M. A systematic study of pulse and pulse reverse plating on acid copper bath for decorative and functional applications. *Sci Rep*. 2022;12(1):18175. doi:10.1038/s41598-022-22650-x
189. Siddiqui A, Potoff R, Huang Y. Sustainability metrics and technical solution derivation for performance improvement of electroplating facilities. *Clean Technol Environ Policy*. 2023;(0123456789). doi:10.1007/s10098-023-02696-9
190. Iñigo EA, Albareda L. Understanding sustainable innovation as a complex adaptive system: a systemic approach to the firm. *J Clean Prod*. 2016;126:1-20. doi:10.1016/j.jclepro.2016.03.036
191. Xiao J, Huang Y. Technology Integration for Sustainable Manufacturing: An Applied Study on Integrated Profitable Pollution Prevention in Surface Finishing Systems. *Ind Eng Chem Res*. 2012;51(35):11434-11444. doi:10.1021/ie300154n
192. Piluso C, Huang Y. Collaborative profitable pollution prevention: an approach for the sustainable development of complex industrial zones under uncertain information. *Clean Technol Environ Policy*. 2009;11(3):307-322. doi:10.1007/s10098-008-0187-y
193. Song H, Bhadbhade N, Huang Y. Sustainability Assessment and

Performance Improvement of Electroplating Process Systems. In: *Sustainability in the Design, Synthesis and Analysis of Chemical Engineering Processes*. Elsevier; 2016:227-248. doi:10.1016/B978-0-12-802032-6.00010-4
194. Kirichenko KY, Vakhniuk IA, Ivanov V V., et al. Complex study of air pollution in electroplating workshop. *Sci Rep*. 2020;10(1):11282. doi:10.1038/s41598-020-67771-3
195. Wei J, Shi P, Cui G, et al. Analysis of soil pollution characteristics and influencing factors based on ten electroplating enterprises. *Environ Pollut*. 2023;337:122562. doi:10.1016/j.envpol.2023.122562
196. Liu T, Wang Z. Contamination and health risk assessment of heavy metals in soil surrounding an electroplating factory in JiaXing, China. *Sci Rep*. 2024;14(1):4097. doi:10.1038/s41598-024-54620-w
197. Ohno T. *Toyota Production System: Beyond Large-Scale Production*. CRC Press, Taylor \& Francis Group
198. Pande P, Neuman RP, Cavanagh RR. *The Six Sigma Way: How GE, Motorola, and Other Top Companies Are Honing Their Performance*. McGraw-Hill Professional; 2001.
199. Monday LM. Define, Measure, Analyze, Improve, Control (DMAIC) Methodology as a Roadmap in Quality Improvement. *Glob J Qual Saf Healthc*. 2022;5(2):44-46. doi:10.36401/JQSH-22-X2
200. Mittal A, Gupta P, Kumar V, Al Owad A, Mahlawat S, Singh S. The performance improvement analysis using Six Sigma DMAIC methodology: A case study on Indian manufacturing company. *Heliyon*. 2023;9(3):e14625. doi:10.1016/j.heliyon.2023.e14625
201. Kadir AMY, Amar K, Asmal S. A Design of Procurement Managing Tool Based on the Lean Six Sigma-DMADV: A Case Study of an Indonesian Fishery Company. *Qual to Success*. 2024;25(199). doi:10.47750/QAS/25.199.15
202. Trubetskaya A, McDermott O, Durand P, Powell DJ. Improving value chain data lifecycle management utilising design for Lean Six Sigma methods. *TQM J*. 2024;36(9):136-154. doi:10.1108/TQM-01-2024-0020
203. Niemann J, Reich B, Stöhr C. *Lean Six Sigma*. Springer Berlin Heidelberg; 2024. doi:10.1007/978-3-662-68744-4
204. Safaei A. *Discrete Event Simulation as a Lean Manufacturing Tool for Copper Plating of PCB Manufacturing*. State University of New York at Binghamton; 2012.
205. Kidwell M. Lean manufacturing and the environment. *Target*. 2006;22(6):13-18.
206. Kantichaimongkol P, Chutima P. Method for Reducing Defect in Electroplating Process.
207. Leiden A, Herrmann C, Thiede S. Cyber-physical production system approach for energy and resource efficient planning and operation of plating

process chains. *J Clean Prod*. 2021;280:125160. doi:10.1016/j.jclepro.2020.125160
208. Todeschini BV, Cortimiglia MN, Callegaro-de-Menezes D, Ghezzi A. Innovative and sustainable business models in the fashion industry: Entrepreneurial drivers, opportunities, and challenges. *Bus Horiz*. 2017;60(6):759-770. doi:10.1016/j.bushor.2017.07.003
209. United Nations (UN). *Transforming Our World: The 2030 Agenda for Sustainable Development*. United Nations (UN); 2015.
210. Wu B, Huang J, Lv Z, et al. Experimental and DFT study of the effect of mercaptosuccinic acid on cyanide-free immersion gold deposition. *RSC Adv*. 2020;10(17):9768-9776. doi:10.1039/d0ra00925c
211. Pinto G, Silva F, Porteiro J, Míguez J, Baptista A. Numerical simulation applied to PVD reactors: An overview. *Coatings*. 2018;8(11):1-21. doi:10.3390/COATINGS8110410
212. Giurlani W, Fidi A, Anselmi E, et al. Specific ion effects on copper electroplating. *Colloids Surfaces B Biointerfaces*. 2023;225:113287. doi:10.1016/j.colsurfb.2023.113287
213. Lai Z, Wang S, Wang C, et al. A comparison of typical additives for copper electroplating based on theoretical computation. *Comput Mater Sci*. 2018;147:95-102. doi:10.1016/j.commatsci.2017.11.049
214. Maris P, Sosonkina M, Vary JP, Ng E, Yang C. Scaling of ab-initio nuclear physics calculations on multicore computer architectures. *Procedia Comput Sci*. 2010;1(1):97-106. doi:10.1016/j.procs.2010.04.012
215. Allinger NL, Zhou X, Bergsma J. Molecular mechanics parameters. *J Mol Struct THEOCHEM*. 1994;312(1):69-83. doi:10.1016/S0166-1280(09)80008-0
216. Wang J, Wolf RM, Caldwell JW, Kollman PA, Case DA. Development and testing of a general amber force field. *J Comput Chem*. 2004;25(9):1157-1174. doi:10.1002/jcc.20035
217. Sprenger KG, Jaeger VW, Pfaendtner J. The General AMBER Force Field (GAFF) Can Accurately Predict Thermodynamic and Transport Properties of Many Ionic Liquids. *J Phys Chem B*. 2015;119(18):5882-5895. doi:10.1021/acs.jpcb.5b00689
218. Di Grande S, Ciofini I, Adamo C, Pagliai M, Cardini G. Absorption Spectra of Flexible Fluorescent Probes by a Combined Computational Approach: Molecular Dynamics Simulations and Time-Dependent Density Functional Theory. *J Phys Chem A*. 2022;126(47):8809-8817. doi:10.1021/acs.jpca.2c04637
219. Daneshmand H, Araghchi M, Asgary M, Karimi M, Torab-Mostaedi M. New insight into adsorption mechanism of nickel–ammonium complex on the growth of nickel surfaces with hierarchical nano/microstructure. *Results in Surfaces and Interfaces*. 2021;3:100014. doi:10.1016/j.rsurfi.2021.100014
220. Pérez Jiménez VA, Hernández-Montoya V, Ramírez-Montoya LA, Castillo-

Borja F, Tovar-Gómez R, Montes-Morán MA. Adsorption of impurities from nickel-plating baths using commercial sorbents to reduce wastewater discharges. *J Environ Manage*. 2021;284:112024. doi:10.1016/j.jenvman.2021.112024
221. Li Q, Hu J, Zhang J, Yang P, Hu Y, An M. Screening of electroplating additive for improving throwing power of copper pyrophosphate bath via molecular dynamics simulation. *Chem Phys Lett*. 2020;757:137848. doi:10.1016/j.cplett.2020.137848
222. Levine IN. *Quantum Chemistry*. (Pearson College, ed.).; 2013.
223. Di Grande S, Kállay M, Barone V. Accurate thermochemistry at affordable cost by means of an improved version of the JunChS-F12 model chemistry. *J Comput Chem*. 2023;44(27):2149-2157. doi:10.1002/jcc.27187
224. Verrucchi M, Comparini A, Bonechi M, et al. Electrochemical spectroscopic analysis of additives in copper plating baths by DRT and multivariate approach. *J Electroanal Chem*. 2024;954:118045. doi:10.1016/j.jelechem.2024.118045
225. Dianat A, Yang H, Bobeth M, Cuniberti G. DFT study of interaction of additives with Cu(111) surface relevant to Cu electrodeposition. *J Appl Electrochem*. 2018;48(2):211-219. doi:10.1007/s10800-018-1150-1
226. Li Y, Ren P, Zhang Y, et al. The influence of leveler Brilliant Green on copper superconformal electroplating based on electrochemical and theoretical study. *J Ind Eng Chem*. 2023;118:78-90. doi:10.1016/j.jiec.2022.10.047
227. Mendieta-Moreno JI, Marcos-Alcalde I, Trabada DG, Gómez-Puertas P, Ortega J, Mendieta J. A Practical Quantum Mechanics Molecular Mechanics Method for the Dynamical Study of Reactions in Biomolecules. In: ; 2015:67-88. doi:10.1016/bs.apcsb.2015.06.003
228. Hou G, Zhu X, Elstner M, Cui Q. A Modified QM/MM Hamiltonian with the Self-Consistent-Charge Density-Functional-Tight-Binding Theory for Highly Charged QM Regions. *J Chem Theory Comput*. 2012;8(11):4293-4304. doi:10.1021/ct300649f
229. Tzeliou CE, Mermigki MA, Tzeli D. Review on the QM/MM Methodologies and Their Application to Metalloproteins. *Molecules*. 2022;27(9):2660. doi:10.3390/molecules27092660
230. Braun TM, Josell D, John J, Moffat TP. Editors' Choice—Simulation of Copper Electrodeposition in Through-Hole Vias. *J Electrochem Soc*. 2020;167(1):013510. doi:10.1149/2.0102001JES
231. *EN 1811:2011+A1:2015 Reference Test Method for Release of Nickel from All Post Assemblies Which Are Inserted into Pierced Parts of the Human Body and Articles Intended to Come into Direct and Prolonged Contact with the Skin*. European Committee for Standardisation; 2015.
232. Fabbri L, Giurlani W, Mencherini G, et al. Optimisation of Thiourea Concentration in a Decorative Copper Plating Acid Bath Based on

Methanesulfonic Electrolyte. *Coatings*. 2022;12(3):1-11. doi:10.3390/coatings12030376
233. Berretti E, Calisi N, Capaccioli A, et al. Electrodeposited white bronzes on brass: Corrosion in 3.5 % sodium chloride solution. *Corros Sci*. 2020;175:108898. doi:10.1016/j.corsci.2020.108898
234. Giurlani W, Biffoli F, Fei L, et al. Analytic procedure for the evaluation of copper intermetallic diffusion in electroplated gold coatings with energy dispersive X-ray microanalysis. *Anal Chim Acta*. 2023;1269:341428. doi:10.1016/j.aca.2023.341428
235. Martinuzzi S, Giovani C, Giurlani W, et al. A robust and cost-effective protocol to fabricate calibration standards for the thickness determination of metal coatings by XRF. *Spectrochim Acta Part B At Spectrosc*. 2021;182(May):106255. doi:10.1016/j.sab.2021.106255
236. Li S. Introduction to Electrochemical Reaction Engineering. In: *Chemical Reaction Engineering*. Elsevier; 2017:599-651. doi:10.1016/B978-0-12-410416-7.00013-6
237. Nishiki Y, Aoki K, Tokuda K, Matsuda H. Secondary current distribution in a two-dimensional model cell composed of an electrode with an open part. *J Appl Electrochem*. 1986;16(2):291-303. doi:10.1007/BF01093363
238. Colli AN, Bisang JM. Tertiary Current and Potential Distribution Including Laminar/Turbulent Convection, Diffusion, and Migration by the Finite Volume Method Using OpenFOAM. *Ind Eng Chem Res*. 2021;60(32):11927-11941. doi:10.1021/acs.iecr.1c01884
239. Beale S, Lehnert W, eds. *Electrochemical Cell Calculations with OpenFOAM*. Vol 42. Springer International Publishing; 2022. doi:10.1007/978-3-030-92178-1
240. Kauffman J, Gilbert J, Paterson E. Multi-Physics Modeling of Electrochemical Deposition. *Fluids*. 2020;5(4):240. doi:10.3390/fluids5040240
241. Rahman MM, Liu W, Lv M, Pan H. Exploring SIMPLE algorithm for all speeds. *Ain Shams Eng J*. 2023;14(2):101854. doi:10.1016/j.asej.2022.101854
242. Issa R., Gosman A., Watkins A. The computation of compressible and incompressible recirculating flows by a non-iterative implicit scheme. *J Comput Phys*. 1986;62(1):66-82. doi:10.1016/0021-9991(86)90100-2
243. Payri R, Ruiz S, Gimeno J, Martí-Aldaraví P. Verification of a new CFD compressible segregated and multi-phase solver with different flux updates-equations sequences. *Appl Math Model*. 2015;39(2):851-861. doi:10.1016/j.apm.2014.07.011
244. Dickinson EJF, Wain AJ. The Butler-Volmer equation in electrochemical theory: Origins, value, and practical application. *J Electroanal Chem*. 2020;872:114145. doi:10.1016/j.jelechem.2020.114145
245. Ngandjong AC, Lombardo T, Primo EN, et al. Investigating electrode

calendering and its impact on electrochemical performance by means of a new discrete element method model: Towards a digital twin of Li-Ion battery manufacturing. *J Power Sources*. 2021;485:229320. doi:10.1016/j.jpowsour.2020.229320
246. Chandrupatla T, Belegundu A. *Introduction to Finite Elements in Engineering*. Cambridge University Press; 2021. doi:10.1017/9781108882293
247. Sabat L, Kundu CK. History of Finite Element Method: A Review. In: ; 2021:395-404. doi:10.1007/978-981-15-4577-1_32
248. Tsige D, Korita M, Beyene A. Deformation analysis of cement modified soft clay soil using finite element method (FEM). *Heliyon*. 2022;8(6):e09613. doi:10.1016/j.heliyon.2022.e09613
249. Dickinson EJF, Ekström H, Fontes E. COMSOL Multiphysics®: Finite element software for electrochemical analysis. A mini-review. *Electrochem commun*. 2014;40:71-74. doi:10.1016/j.elecom.2013.12.020
250. Goel V, Thornton K. Enabling the electrochemical simulation of Li-ion battery electrodes with anisotropic tortuosity in COMSOL Multiphysics®. *MethodsX*. 2021;8:101425. doi:10.1016/j.mex.2021.101425
251. Andreou E, Roy S. Modelling the Scaling-Up of the Nickel Electroforming Process. *Front Chem Eng*. 2022;4. doi:10.3389/fceng.2022.755725
252. Jasak H. OpenFOAM: Open source CFD in research and industry. *Int J Nav Archit Ocean Eng*. 2009;1(2):89-94. doi:10.2478/IJNAOE-2013-0011
253. Huang M, Weber N, Mutschke G. A Simulation Framework for Electrochemical Processes with Electrolyte Flow. *J Electrochem Soc*. 2023;170(7):073502. doi:10.1149/1945-7111/ace333
254. Lee YK. How complex systems get engaged in fashion design creation: Using artificial intelligence. *Think Ski Creat*. 2022;46:101137. doi:10.1016/j.tsc.2022.101137
255. Särmäkari N, Vänskä A. 'Just hit a button!' – fashion 4.0 designers as cyborgs, experimenting and designing with generative algorithms. *Int J Fash Des Technol Educ*. 2022;15(2):211-220. doi:10.1080/17543266.2021.1991005
256. Kallioras NA, Lagaros ND. DzAI𝕟: Deep learning based generative design. *Procedia Manuf*. 2020;44:591-598. doi:10.1016/j.promfg.2020.02.251
257. Ishizuka N, Yamada T, Izui K, Nishiwaki S. Topology optimization for unifying deposit thickness in electroplating process. *Struct Multidiscip Optim*. 2020;62(4):1767-1785. doi:10.1007/s00158-020-02574-8
258. Yang G, Deng D, Zhang Y, Zhu Q, Cai J. Numerical Optimization of Electrodeposition Thickness Uniformity with Respect to the Layout of Anode and Cathode. *Electrocatalysis*. 2021;12(5):478-488. doi:10.1007/s12678-021-00668-5
259. Giurlani W, Berretti E, Innocenti M, Lavacchi A. Measuring the thickness of metal coatings: A review of the methods. *Coatings*. 2020;10(12):1-36.

doi:10.3390/coatings10121211
260. Brevettato RAEP, il sistema ITALFIMET per un risparmio di metallo prezioso fino al 15%. *Galvanotec e nuove finiture*. Published online April 2020:234-236.
261. Luxury Brands Technologies. HCS: Homogeneous Coating System.
262. Chen M shu, Wu M hsun, Lin C ming. Application of Indices Cp and Cpk to Improve Quality Control Capability in Clinical Biochemistry Laboratories. 2014;57(5):63-68. doi:10.4077/CJP.2014.BAB170
263. Mariani E, Giurlani W, Verrucchi M, Dell'Aquila V, Lo Nostro P, Innocenti M. Pulse Electroplating of Gold-Nickel Alloys: Morphological and Aesthetic Improvement Compared to DC. *J Electrochem Soc*. 2024;171(1):012504. doi:10.1149/1945-7111/ad1d97
264. Canda L, Heput T, Ardelean E. Methods for recovering precious metals from industrial waste. *IOP Conf Ser Mater Sci Eng*. 2016;106:012020. doi:10.1088/1757-899X/106/1/012020
265. Comparini A, Del Pace I, Giurlani W, et al. Electroplating on Al6082 Aluminium: A New Green and Sustainable Approach. *Coatings*. 2023;13(1):1-13. doi:10.3390/coatings13010013
266. Ani JU, Akpomie KG, Okoro UC, Aneke LE, Onukwuli OD, Ujam OT. Potentials of activated carbon produced from biomass materials for sequestration of dyes, heavy metals, and crude oil components from aqueous environment. *Appl Water Sci*. 2020;10(2):69. doi:10.1007/s13201-020-1149-8
267. Fu F, Wang Q. Removal of heavy metal ions from wastewaters: A review. *J Environ Manage*. 2011;92(3):407-418. doi:10.1016/j.jenvman.2010.11.011
268. Habib SS, Naz S, Fazio F, et al. Assessment and Bioaccumulation of Heavy Metals in Water, Fish (wild and Farmed) and Associated Human Health Risk. *Biol Trace Elem Res*. 2024;202(2):725-735. doi:10.1007/s12011-023-03703-2
269. Barakat MA. New trends in removing heavy metals from industrial wastewater. *Arab J Chem*. 2011;4(4):361-377. doi:10.1016/j.arabjc.2010.07.019
270. Babel S. Low-cost adsorbents for heavy metals uptake from contaminated water: a review. *J Hazard Mater*. 2003;97(1-3):219-243. doi:10.1016/S0304-3894(02)00263-7
271. Bragagni M, Xhaferraj L. Copper and our sustainable future. *Esharelife Found*. Published online 2021. doi:10.13140/RG.2.2.26384.53762
272. Paulino AT, Minasse FAS, Guilherme MR, Reis A V., Muniz EC, Nozaki J. Novel adsorbent based on silkworm chrysalides for removal of heavy metals from wastewaters. *J Colloid Interface Sci*. 2006;301(2):479-487. doi:10.1016/j.jcis.2006.05.032
273. Oyaro NJOMEGE. The contents of Pb, Cu, Zn and Cd in meat in nairobi, Kenya. *Int J food, Agric Environ* . 2007;5(3-4):119-121.

274. Kania H, Saternus M. Evaluation and Current State of Primary and Secondary Zinc Production—A Review. *Appl Sci*. 2023;13(3):2003. doi:10.3390/app13032003
275. Cleanmetals. Nickel.
276. Borba CE, Guirardello R, Silva EA, Veit MT, Tavares CRG. Removal of nickel(II) ions from aqueous solution by biosorption in a fixed bed column: Experimental and theoretical breakthrough curves. *Biochem Eng J*. 2006;30(2):184-191. doi:10.1016/j.bej.2006.04.001
277. Tomioka H, King TE, Schnabel A. Gold-induced pulmonary disease: Clinical features, outcomes, and differentiation from rheumatoid lung disease. *Pneumologie*. 1997;51(9):921.
278. Quanto male fa al pianeta l'estrazione dell'oro?
279. Khezami L, Capart R. Removal of chromium(VI) from aqueous solution by activated carbons: Kinetic and equilibrium studies. *J Hazard Mater*. 2005;123(1-3):223-231. doi:10.1016/j.jhazmat.2005.04.012
280. Ripley EA, Redmann ER, Crowder AA, et al. *Environmental Effects of Mining*. Routledge; 2018. doi:10.1201/9780203757147
281. Earthworks, Oxfam America. *Dirty Metals - Mining, Communities and the Environment*.
282. Cui J, Forssberg E. Mechanical recycling of waste electric and electronic equipment: a review. *J Hazard Mater*. 2003;99(3):243-263. doi:10.1016/S0304-3894(03)00061-X
283. Lezak S, Wilson C, Ansar A, Bazilian M. The case against gold mining. *Environ Res Lett*. 2023;18(1):011001. doi:10.1088/1748-9326/ac9f26
284. Chen W, Hong J, Wang C, et al. Water footprint assessment of gold refining: Case study based on life cycle assessment. *Ecol Indic*. 2021;122:107319. doi:10.1016/j.ecolind.2020.107319
285. Dossou Etui IM, Stylo M, Davis K, et al. Artisanal and small-scale gold mining and biodiversity: a global literature review. *Ecotoxicology*. Published online May 2024. doi:10.1007/s10646-024-02748-w
286. Oto etico: un passo avanti verso un futuro sostenibile.
287. Fritz B, Peregovich B, da Silva Tenório L, da Silva Alves AC, Schmidt M. Mercury and CO2 emissions from artisanal gold mining in Brazilian Amazon rainforest. *Nat Sustain*. 2023;7(1):15-22. doi:10.1038/s41893-023-01242-1
288. Esdaile LJ, Chalker JM. The Mercury Problem in Artisanal and Small-Scale Gold Mining. *Chem – A Eur J*. 2018;24(27):6905-6916. doi:10.1002/chem.201704840
289. Cheng Y, Watari T, Seccatore J, Nakajima K, Nansai K, Takaoka M. A review of gold production, mercury consumption, and emission in artisanal and small-scale gold mining (ASGM). *Resour Policy*. 2023;81:103370. doi:10.1016/j.resourpol.2023.103370
290. Mook A, Overdevest C. Fairtrade credentialism: towards understanding

certified producer organizations' perceptions of Fairtrade as a credential. *Globalizations*. 2020;17(1):110-125. doi:10.1080/14747731.2019.1638113
291. Oakley P. Searching for pure gold: The impact of ethical gold sourcing certification programmes in the UK and Switzerland. *Environ Sci Policy*. 2022;132:101-108. doi:10.1016/j.envsci.2022.02.016
292. Gold and precious metals.
293. Bloomfield MJ, Manchanda N. Business, power, and private regulatory governance: Shaping subjectivities and limiting possibilities in the gold supply chain. *Regul Gov*. 2024;18(1):81-98. doi:10.1111/rego.12522
294. Kurniawan TA, Chan GYS, Lo WH, Babel S. Physico–chemical treatment techniques for wastewater laden with heavy metals. *Chem Eng J*. 2006;118(1-2):83-98. doi:10.1016/j.cej.2006.01.015
295. BABU BR, BHANU SU, MEERA KS. Waste Minimization in Electroplating Industries: A Review. *J Environ Sci Heal Part C*. 2009;27(3):155-177. doi:10.1080/10590500903124158
296. Azmi AA, Jai J, Zamanhuri NA, Yahya A. Precious Metals Recovery from Electroplating Wastewater: A Review. *IOP Conf Ser Mater Sci Eng*. 2018;358:012024. doi:10.1088/1757-899X/358/1/012024
297. Upadhyay K. Solution for wastewater problem related to electroplating industry: an overview. *J Ind Pollut Control*. 2006;22(1):59-66.
298. ADHOUM N, MONSER L, BELLAKHAL N, BELGAIED J. Treatment of electroplating wastewater containing Cu2+, Zn2+ and Cr(VI) by electrocoagulation. *J Hazard Mater*. 2004;112(3):207-213. doi:10.1016/j.jhazmat.2004.04.018
299. Selpiana S, Haryati S, Bustan MD. Cathode current efficiency of lead electrowinning in sulphate electrolyte. *AIP Conf Proc*. 2022;2391(1):040007. doi:10.1063/5.0072429
300. Rajoria S, Vashishtha M, Sangal VK. Treatment of electroplating industry wastewater: a review on the various techniques. *Environ Sci Pollut Res*. 2022;29(48):72196-72246. doi:10.1007/s11356-022-18643-y
301. Kim J, Yoon S, Choi M, et al. Metal ion recovery from electrodialysis-concentrated plating wastewater via pilot-scale sequential electrowinning/chemical precipitation. *J Clean Prod*. 2022;330:129879. doi:10.1016/j.jclepro.2021.129879
302. Janssen L. The role of electrochemistry and electrochemical technology in environmental protection. *Chem Eng J*. 2002;85(2-3):137-146. doi:10.1016/S1385-8947(01)00218-2
303. N. Kongsricharoern, C. Polprasert. Electrochemical precipitation of chromium (Cr) from an electroplating wastewater. *Water Sci Technol*. 1995;31(9). doi:10.1016/0273-1223(95)00412-G
304. US Environmental Protection Agency (EPA). Chemical Precipitation. 2000;(EPA832-F-.
305. Lawrence K. Wang YTHNKS. *Physicochemical Treatment Processes*. Vol

3. (Wang LK, Hung YT, Shammas NK, eds.). Humana Press; 2005. doi:10.1385/159259820x
306. Shammas NK. Coagulation and Flocculation. In: *Physicochemical Treatment Processes*. Humana Press; 2005:103-139. doi:10.1385/1-59259-820-x:103
307. Cheng RC, Liang S, Wang H, Beuhler MD. Enhanced coagulation for arsenic removal. *J AWWA*. 1994;86(9):79-90. doi:10.1002/j.1551-8833.1994.tb06248.x
308. Matis KA, Zouboulis AI, Gallios GP, Erwe T, Blöcher C. Application of flotation for the separation of metal-loaded zeolites. *Chemosphere*. 2004;55(1):65-72. doi:10.1016/j.chemosphere.2003.11.030
309. Vigneswaran S, Ngo HH, Chaudhary DS, Hung YT. Physicochemical Treatment Processes for Water Reuse. In: *Physicochemical Treatment Processes*. Humana Press; 2005:635-676. doi:10.1385/1-59259-820-x:635
310. Madaeni S., Mansourpanah Y. COD Removal from Concentrated Wastewater Using Membranes. *Filtr Sep*. 2003;40(6):40-46. doi:10.1016/S0015-1882(03)00635-9
311. Dąbrowski A, Hubicki Z, Podkościelny P, Robens E. Selective removal of the heavy metal ions from waters and industrial wastewaters by ion-exchange method. *Chemosphere*. 2004;56(2):91-106. doi:10.1016/j.chemosphere.2004.03.006
312. Yahya MA, Al-Qodah Z, Ngah CWZ. Agricultural bio-waste materials as potential sustainable precursors used for activated carbon production: A review. *Renew Sustain Energy Rev*. 2015;46:218-235. doi:10.1016/j.rser.2015.02.051
313. Moreira SA, Melo DQ, de Lima ACA, et al. Removal of Ni2+, Cu2+, Zn2+, Cd2+ ions from aqueous solutions using cashew peduncle bagasse as an eco-friendly biosorbent. *Desalin Water Treat*. 2016;57(22):10462-10475. doi:10.1080/19443994.2015.1037355
314. Cesiulis H, Tsyntsaru N. Eco-Friendly Electrowinning for Metals Recovery from Waste Electrical and Electronic Equipment (WEEE). *Coatings*. 2023;13(3):574. doi:10.3390/coatings13030574
315. Chen G. Electrochemical technologies in wastewater treatment. *Sep Purif Technol*. 2004;38(1):11-41. doi:10.1016/j.seppur.2003.10.006
316. Subbaiah T, Mallick S., Mishra K., Sanjay K, Das R. Electrochemical precipitation of nickel hydroxide. *J Power Sources*. 2002;112(2):562-569. doi:10.1016/S0378-7753(02)00470-6
317. Herrmann JM. Heterogeneous photocatalysis: fundamentals and applications to the removal of various types of aqueous pollutants. *Catal Today*. 1999;53(1):115-129. doi:10.1016/S0920-5861(99)00107-8
318. BARAKAT M. Removal of toxic cyanide and Cu(II) Ions from water by illuminated TiO2 catalyst. *Appl Catal B Environ*. 2004;53(1):13-20. doi:10.1016/j.apcatb.2004.05.003